

Scanning Probe Microscopy Characterization of Organic Self-Assembled Monolayers

THÈSE N° 8274 (2018)

PRÉSENTÉE LE 26 JANVIER 2018

À LA FACULTÉ DES SCIENCES ET TECHNIQUES DE L'INGÉNIEUR
LABORATOIRE DES NANOMATÉRIAUX SUPRAMOLÉCULAIRES ET INTERFACES - CHAIRE CONSTELLIUM
PROGRAMME DOCTORAL EN SCIENCE ET GÉNIE DES MATÉRIAUX

ÉCOLE POLYTECHNIQUE FÉDÉRALE DE LAUSANNE

POUR L'OBTENTION DU GRADE DE DOCTEUR ÈS SCIENCES

PAR

Evangelia-Nefeli ATHANASOPOULOU

acceptée sur proposition du jury:

Prof. C. Hébert, présidente du jury
Prof. F. Stellacci, directeur de thèse
Prof. R. Garcia, rapporteur
Prof. M. Halik, rapporteur
Prof. E. Amstad, rapporteuse



ÉCOLE POLYTECHNIQUE
FÉDÉRALE DE LAUSANNE

Suisse
2018

Acknowledgments

Deciding to work towards a PhD has been my first step in what I hope to be a career in research and science. Very quickly however I found out that my somewhat romantic and certainly naïve notion of a researcher effortlessly going from scientific breakthrough to scientific breakthrough was, to say the least, misguided. Over the past four years I realized that research is a laborious occupation, requiring painstaking effort, perseverance, and clarity of mind. Being somewhat pessimistic by nature, it has often been difficult for me to maintain my motivation. I would like, therefore, to take a moment to thank the people who supported me and helped me see that, no matter how many times your experiment fails or your ideas don't come to fruition, there is always a light at the end of the tunnel.

First and foremost, I would like to thank my supervisor, Prof. Francesco Stellacci, who offered me an opportunity to join his group, learn from and beside him, and always inspired and guided me towards research that made me happy. Working under the guidance of a person so positive and passionate about science has truly been a pleasure. Francesco supported me through a very difficult period in my life, more than I could ever expect or hope a supervisor to, and for that I will be forever grateful.

I would also like to thank Prof. Ricardo Garcia, Prof. Marcus Halik, Prof. Esther Amstad and Prof. Cécile Hébert, who, as members of my PhD thesis committee, saw the scientific merit of my work. I would like to especially thank Prof. Garcia, who allowed me to visit his group, and Dr. Alma P. Perrino, who took the time to teach me the technique of bimodal AFM.

I would like to thank Mr. Pierre Metraux, who performed all the XPS measurements presented here, Mr. Friedhelm Freiss from Asylum Research, without whom I could have never kept our AFMs up and running, and Ms. Chiara Donini.

I was very fortunate to join a group that quickly evolved from colleagues to friends. I would like to thank all the members of SuNMIL, past and present, for their help, support, and patience. In particular I would like to thank Nikos, Maria, Sergio, Pelin, Ula, Paulo, Ozgun, Matej, Rosie, Anna and Zhi. Thank you for your practical, mental and emotional support, friendship, humor, wit, music, and endless coffee break discussions.

I would also like to thank my friends, who heard my rants, held my hand, laughed with me, cried with me, and always helped me see the bigger picture. Christina, Eleni, Varvara, Myrto: I could not have done it without you.

Last but certainly not least, a big thank you to my family. My brother, Nassos, who always inspired me to do better, find the humor in any situation and proofread everything without complaint. My dad, Kostis, for his level-headedness and inquisitive mind, for passing down his love for learning and always challenging me intellectually. My mum, Penny. You taught me to persist, to insist, to learn, to brush the dust off and try again, to believe in myself. I so wish you could see how much we have achieved. For all that and so much more, thank you. Always.

Abstract

As technology advances, surface coatings become more and more important to assure materials performances. In recent years, molecular coatings have found larger acceptance and uses. Among them, self-assembled monolayers (SAMs) are attractive because they are versatile and their manufacturing approach is easy to scale up. Their mechanical properties, such as elasticity, are generally considered an important quality indicator. The molecular structure and ordering of SAMs is believed to be one of the key causes for their mechanical properties. A direct set of structure-property relationships has not been obtained yet. This is mainly due to the difficulty in achieving mechanical and structural information about SAMs at the same time. Most information currently available on intermolecular interactions in SAMs pertains to highly ordered systems on ideal flat surfaces, *i.e.* the easiest systems to study.

This thesis presents a novel approach to address the question of determining structure and mechanical properties of self-assembled monolayers at the same time. The effective Young's modulus, E^* , of SAMs was measured using the Atomic Force Microscope operated in the bimodal excitation and detection mode (bimodal AFM) while at the same time imaging at high resolution.

Bimodal AFM was first used on alkanethiol molecules self-assembled on Au (111), a model system for SAMs. Surface elasticity has been reliably determined and found to be ligand-length dependent. An interpretation of this behavior is provided in the thesis.

A similar investigation has been extended to the characterization of octadecylphosphonic acid SAMs on Al_2O_3 , an industrially relevant system. The monolayer ordering as a function of monolayer formation time was explored, together with the evolution of surface elasticity. The latter allows distinguishing between the consecutive steps of ligand adsorption, monolayer ordering and multilayer formation.

The method developed, *i.e.* simultaneous imaging and mechanical property derivation, was extended to provide localization of the chemical species present in thiolated binary SAMs. Within the systems tested phase separation down to ~ 10 nm domains could be observed both in the topography and in the elasticity channel.

In conclusion, the results shown in this thesis demonstrate that bimodal AFM allows for accurate characterization of surface nanomechanical properties in organic self-assembled systems, as well as the way those scale with varying molecular ordering.

Keywords: self-assembled monolayers, thiols, alkylphosphonic acids, bimodal AFM, Young's modulus, molecular ordering

Résumé

Avec les récentes avancées technologiques, le choix du revêtement de la surface d'un matériau est devenu de plus en plus important en vue d'obtenir les performances désirées. Ces dernières années, les revêtements moléculaires ont rencontré un grand succès et de nombreuses applications importantes ont été développées. Parmi ces revêtements, les monocouches auto-assemblées (SAMs) sont particulièrement attrayantes du fait de leur polyvalence et de leur capacité à être mises à l'échelle. Leurs propriétés mécaniques, comme l'élasticité, sont généralement considérées comme un important indicateur de qualité et sont probablement définies par la structure moléculaire et l'organisation des SAMs, même si aucune relation structure-propriétés n'a encore été obtenue à ce jour. Ceci est principalement dû à la difficulté d'obtenir simultanément des informations d'ordre structural et mécanique. Actuellement, la majorité des informations disponibles sur les interactions intermoléculaires présentes dans les SAMs ont été obtenues à l'aide de systèmes hautement ordonnés sur des surfaces planes idéales qui sont, à l'heure actuelle, les systèmes les plus simples à étudier.

Cette thèse présente une nouvelle approche pour aborder la détermination simultanée de la structure et des propriétés mécaniques de monocouches auto-assemblées. Le module de Young (E^*) des SAMs a été mesuré en enregistrant des images à haute résolution à l'aide d'un Microscope à Force Atomique opérant en mode bimodal de détection et d'excitation (AFM bimodal).

L'AFM bimodal a été utilisé en premier lieu sur des molécules d'alcanethiols auto-assemblées sur de l'or (Au (111)), un système modèle pour les SAMs. L'élasticité de la surface a ainsi pu être déterminée de manière fiable et s'est avérée être dépendante de la longueur des ligands utilisés. Une interprétation de ce comportement est présentée dans la thèse.

Une analyse similaire a été réalisée pour la caractérisation de SAMs d'acide octadécylphosphonique sur de l'alumine, Al_2O_3 , un système pertinent pour l'industrie. L'organisation de ces monocouches en fonction de leur temps de formation ainsi que l'évolution de l'élasticité de la surface ont été étudiés, cette dernière permettant de différencier les étapes successives de l'adsorption du ligand sur la surface, de l'organisation de la monocouche et, finalement, de la formation de multicouches.

La méthode développée ici, c'est-à-dire l'imagerie couplée à l'établissement simultané des propriétés mécaniques, a également été utilisée afin de fournir la localisation des espèces chimiques présentes dans les SAMs binaires thiolées. Dans ces systèmes, une séparation de phase allant jusqu'à des domaines d'une dizaine de nanomètres a ainsi pu être observée à la fois sur les images topographiques et élastiques.

En conclusion, les résultats présentés dans cette thèse démontrent que l'AFM bimodal permet une caractérisation précise des propriétés nanomécaniques des surfaces dans des systèmes organiques auto-assemblés, mais aussi la façon dont ces propriétés évoluent avec l'arrangement moléculaire.

Mots-clés : monocouches auto-assemblées, thiols, acide octadécylphosphonique, AFM bimodal, module de Young, ordre moléculaire.

Contents

Acknowledgments.....	i
Abstract	iii
Résumé	v
Abbreviations	xi
Chapter 1	
Introduction and thesis structure	1
1.1. Introduction.....	1
1.2. Structure of the thesis	3
1.3. References	6
Chapter 2	
Organic self-assembled monolayers	7
2.1. Introduction to organic self-assembled monolayers (SAMs)	8
2.2. Deposition of SAMs.....	9
2.3. Thiol SAMs on Au (111)	10
2.3.1. The Au-thiolate interface: Binding mechanism, in-plane diffusion and interfacial disorder	11
2.4. Alkylphosphonic acid SAMs on Al ₂ O ₃	13
2.4.1. Binding mechanism	14
2.5. Variations in ligand ordering and packing density	16
2.5.1. Ligand length.....	16
2.5.2. Effect of spacer chains and end functionalities	19
2.5.3. Substrate effect.....	20
2.5.4. The role of bimodal AFM in determining ligand packing and ordering.....	21
2.6. Binary thiol SAMs: Phase separation and mixing.....	21
2.6.1. The role of bimodal AFM in mixed ligand SAM characterization	22
2.7. Kinetics and stability of SAMs and multilayer formation	23
2.7.1. Kinetics and stability of SAMs	23
2.7.2. Multilayer formation	25
2.7.3. The role of bimodal AFM	25
2.8. References	27

Chapter 3

Bimodal Atomic Force Microscopy for the nanomechanical characterization of organic self-assembled monolayers	37
3.1. The working principle of the AFM.....	38
3.2. Equation of motion for an oscillating cantilever: The Euler-Bernoulli beam and the equivalent point-mass model	39
3.3. Tip-sample interaction forces and their effect in cantilever oscillation parameters.....	43
3.3.1. Weakly perturbed harmonic oscillator	43
3.3.2. The Virial Dissipation method.....	44
3.3.3. Net repulsive, net attractive regime and bistability.....	45
3.4. Conservative and dissipative forces in Atomic Force Microscopy	48
3.4.1. Contact mechanics forces	48
3.5. Multifrequency Atomic Force Microscopy.....	51
3.5.1. Multiharmonic AFM imaging	52
3.5.2. Band excitation	52
3.5.3. Torsional harmonic AFM	52
3.5.4. Nanomechanical holography	53
3.5.5. Bimodal AFM.....	53
3.6. References	65

Chapter 4

Nanomechanical characterization of homoligand and binary thiolated self-assembled monolayers on Au (111) using bimodal Atomic Force Microscopy.....	71
4.1. Introduction	72
4.2. Materials and Methods	74
4.3. Results and Discussion.....	77
4.3.1. Contact mechanics model selection	77
4.3.2. Comparative study of homoligand alkanethiol SAMs	78
4.3.3. Deconvolution of substrate-film elasticity	81
4.3.4. Other thiols	84
4.3.5. Binary SAMs: Surface Chemical Recognition	86
4.4. Conclusions	91
4.5. References	93

Chapter 5

Kinetic study of the formation of octadecylphosphonic acid self-assembled monolayers on Al ₂ O ₃ and the characteristics thereof	97
5.1. Introduction.....	98
5.2. Materials and methods	99
5.3. Results and Discussion	101
5.3.1. ODPA SAMs on flat Al ₂ O ₃	101
5.3.2. Alkylphosphonic acid SAMs on industrial surfaces	110
5.4. Conclusions	111
5.5. References.....	113

Chapter 6

Summary, conclusions and outlook

6.1. Summary and conclusions	117
6.2. Outlook	119
6.3. References.....	123
Appendix A.....	125
Appendix B.....	135
References	146
Curriculum Vitae.....	147

Abbreviations

AFM	Atomic Force Microscope
A_0	Free amplitude of oscillation
A	Work amplitude
Al_2O_3	Aluminium oxide
ALD	Atomic Layer Deposition
AM	Amplitude Modulation
Au	Gold
C11	1-undecanethiol
C12	1-dodecanethiol
C18	1-octadecanethiol
C4	1-butanethiol
C7	1-heptanethiol
C9	1-nonanethiol
CA	Contact angle
CD	Cyclodextrin
CN4T	4-cyano-1-butanethiol
DMT	Derjaguin-Muller-Toporov
E	Young's modulus
E^*	Effective Young's modulus
ECM	Extracellular matrix
f_0	Resonance frequency
f	Driving frequency
FM	Frequency Modulation
JKR	Johnson-Kendall-Roberts
LSV	Linear Sweep Voltammetry
MPA	Mercaptopropionic acid
MSA	Mercaptosuccinic acid
MUS	11-mercaptoundecanesulfonate
O	Oxygen
ODPA	Octadecylphosphonic acid
OT	1-octanethiol
P	Phosphorus

PA	Phosphonic acid
PS	Polystyrene
S	Sulfur
SPM	Scanning Probe Microscopy
STM	Scanning Tunneling Microscope
t_M	Monolayer formation time
TMA	Trimethylaminedecanethiol
XPS	X-ray Photoelectron Spectroscopy
ω_0	Angular resonance frequency
ω	Driving angular frequency

Chapter 1

Introduction and thesis structure

1.1. Introduction

Surfaces, the first few nanometers of a material, dominate the way we interact with our surroundings. From the caution to not touch the hot oven door, to our decision to buy the soft woolen sweater, every contact with a material, pleasant or not, is guided by our perception of its surface. As the first line of interaction with the material, it then comes as no surprise that historically the first aspect of a material to be modified is the surface. The inventive prehistoric human, using animal fat and wax to stop water permeating his or her clothes, and the rebellious 21st century teenager dying his or her hair in a vivid shade of green share more than a common ancestor: they both modify the surface of a material, altering its properties while leaving the bulk unaffected.

Surface modification is an extremely diverse scientific field, studying the ways with which physical, chemical or biological features of a surface can be altered and tailored according to specific needs. Anti-corrosion coatings, self-cleaning paints, antibacterial and antiviral drugs; they all target the surface of a material aiming at its modification. One of the most interesting methods of surface modification is the use of organic self-assembled monolayers.

Organic self-assembled monolayers (SAMs) are highly organized molecularly thin structures formed by the spontaneous adsorption of active compounds, or ligands, on suitable surfaces, or substrates, and their subsequent ordering [1]. SAMs offer a unique platform for basic science research, as well as real-life applications, as they provide an easy synthetic route to inherently manufacturable and reproducible thin films, altering the properties of surfaces while leaving the bulk of the substrate unaffected.

The interest in SAMs coincided with and was largely fuelled by the great advent of nanotechnology, predicted by Feynman in 1959 [2]. Optimization of analytical techniques such as X-ray Photoelectron Spectroscopy (XPS) allowed the chemical analysis of the first few atomic layers (~5 nm) of a material. The construction of more synchrotron light sources popularized their use as a method to characterize materials with subnanometer resolution. The development of the Scanning Tunnelling Microscope (STM) in 1981 by Binnig and Rohrer offered an invaluable tool for the visualization of

subnanometer size objects on conductive surfaces [3]. The development of the Atomic Force Microscope (AFM) a few years later, by Binnig, Quate and Gerber, allowed insulating objects to be imaged with subnanometer lateral resolution [4] and opened the door to the characterization of intermolecular interactions in virtually any material.

The study of intermolecular interaction in SAMs has been the focal point of numerous scientific studies since 1983, when the work of Nuzzo and Allara [5] drew attention to the field.

The issue of molecular arrangement at the nanoscale has been addressed at length, particularly in the case of SAMs of thiolated molecules on Au (111). A number of models have been proposed regarding the mode of bond formation and discussing the effects of this on the arrangement of the ligand molecules, the onset of orientation and ordering, and formation of densely packed phases. Thiol SAMs have been observed to form a number of crystalline structures, the appearance and lattice of which depends on a number of parameters, such as the structure of the ligand and the time of the monolayer formation.

Alkylphosphonic acid SAMs on metal oxides in general, and Al_2O_3 in particular, are another interesting and widely studied system. The unique mode of bond formation between the $-\text{PO}(\text{OH})_2$ headgroup and the $-\text{OH}$ rich surface of Al_2O_3 has been experimentally and theoretically addressed. However, many aspects of the structure of phosphonic acid SAMs and how this affects their properties still remain unknown.

Even before the official “birth” of the scientific domain, SAMs had been patented industrial modification processes for metal surfaces, starting as early as 1961 [6]. Application of the scientific knowledge obtained in academia to industrial processes could set the basis for a more rational approach to the design of industrial practices, leading to product and process optimization, minimizing material waste and environmental impact, while favoring sustainable economic growth. However, in the past fifty-six years during which SAMs have been deposited and studied, it seems that the paths of academic and industrial research have been only parallel, and often with a significant lag between them. Synchrotron radiation characterization and high resolution techniques allowed scientist to gain unique insight on the chemical and interatomic aspects of SAM formation and organization, focusing on ideal, crystalline structures on atomically flat surfaces. On the other hand, industrial SAM deposition favors the use of old, “tried and tested”, processes, which successfully provide the

desired macroscopic properties of the surface, without overtly concerning themselves with interactions at the nanoscale.

One of the prerequisites for bridging the gap between academia and industry is a detailed understanding of the exact synthesis-structure-properties relation of the SAMs, and their quantification using a simple, commercially available, yet effective and highly sensitive characterization technique.

In this thesis, I propose the use of nanomechanical characteristics as an indication of molecular ordering in soft matter. To do that, the use of a characterization technique combining high sensitivity, low loads, small indentation depth and high lateral resolution is imperative. I investigate the use of bimodal Atomic Force Microscopy for the accurate and quantifiable determination of surface elasticity in SAMs, and the correlation of the macroscopic elasticity of the material to the ordering of the constituent components, the ligands, at the nanoscale.

The purpose of this study is to demonstrate that nanoscopic interactions, previously accessible only in highly controlled environments and thus not readily applicable in large-scale processes, can be probed and interpreted by measuring the macroscopic elasticity of a soft thin film, using a sensitive, yet commercially accessible and robust technique.

1.2. Structure of the thesis

An overview of the state of the art on thiol and alkylphosphonic acid SAM deposition, structure and characterization is the subject of **Chapter 2**. The basic aspects of monolayer formation and ordering are discussed, and the areas where further improvement in the field is possible are highlighted. The hypothesis that forms the backbone of this thesis is formulated: can we use a macroscopic property of the materials as an indicator of ligand ordering? I propose the measurement of surface elasticity, E^* , and its correlation to parameters proven to influence ligand ordering: ligand length, ligand stereochemistry, and monolayer formation time. I suggest the use of an Atomic Force Microscope (AFM) operated in a bimodal excitation scheme as the main technique for the nanomechanical characterization of SAMs. The technique has been successfully used on bulk and thin film polymers and polymer blends, as well as biological structures, such as proteins. However, the use of bimodal AFM for the accurate and quantitative nanomechanical characterization of SAMs has not been demonstrated yet.

The basic principles of operation of an AFM in the dynamic, amplitude modulation (AM) mode are introduced in **Chapter 3**. The way interatomic forces influence the movement of an oscillating cantilever is discussed, as well as how these forces can be quantified and used to extract information on particular material properties. The non-linear movement of a cantilever under the influence of multiple forces in the same tip-sample distance is introduced, and the way multifrequency AFM can utilize this non-linearity to enhance imaging and material contrast is presented. Emphasis is given in the operation of an AFM under bimodal excitation, and the way nanomechanical properties, such as elasticity, can be probed and quantified.

In **Chapter 4**, experimental work on the characterization of thiol SAMs on Au (111) via bimodal AFM is presented and discussed. A correlation between ligand length and E^* is found and it is demonstrated that a differentiation between SAMs of varying ligands through surface elasticity is possible. By deconvoluting the effect of the substrate from E^* , the actual Young's moduli of the tested alkanethiol SAMs are calculated. These values provided the basis for a comparative evaluation of ligand ordering and how it scaled with ligand length, for set monolayer deposition conditions. Moreover, they were in good agreement with previous studies, underlying the robustness of the technique as a quantitative characterization tool. These observations on the behavior of homoligand SAMs were used for the characterization of phase separated binary SAMs. The high lateral resolution of AFM and direct correlation between the topographic and Young's modulus channels allowed the identification of chemically different domains and the localization on the surface of the two types of ligands used, addressing a long-standing problem in the field of binary SAMs formation and characterization.

Additional AFM images of the samples discussed in Chapter 4 are presented in **Appendix A**.

Bimodal AFM was further used for the characterization of octadecylphosphonic acid SAMs, as discussed in **Chapter 5**. In this case all SAMs were formed from the same ligand, while increasing monolayer formation time, t_M . XPS and contact angle (C.A.) characterization of the SAMs allows the formulation of a model describing the kinetic process of octadecylphosphonic acid (ODPA) SAM formation as a three step process; the three steps being initial rapid adsorption and formation of a physisorbed, sparse submonolayer for $t_M \leq 1\text{min}$, formation of a lying-down chemisorbed phase

accompanied by slower ligand uptake and significant increase in ordering leading to a dense, well-ordered SAM for $2 \text{ min} \leq t_M \leq 2 \text{ h}$, followed by multilayer formation. The structures corresponding to each step showed remarkably different elasticity and, in the case of multilayer formation, stability. The rate of monolayer and multilayer formation has been calculated, by fitting the experimental results to a suitable absorption model. In addition to the characterization of ODPA SAMs on ideally flat surfaces, E^* of alkylphosphonic acid SAMs grown under industrially relevant conditions on rough aluminium alloys surfaces was measured via bimodal AFM. The results illustrated the applicability of bimodal AFM as a characterization technique and possibly quality control method not only in the context of a laboratory, but also alongside an industrial production line.

Additional AFM images, XPS data and the fitting details of the absorption models discussed in Chapter 5 are presented in **Appendix B**.

Chapters 4 and 5 are written in the form of paper drafts, soon to be submitted.

In **Chapter 6** a summary of all experimental results is given, along with some suggestions on further uses of the technique. In the same way that bimodal AFM allowed the chemical mapping of a phase separated binary SAM on a flat surface, it can be used to characterize different steps of different ligand exchange reactions on the surface of Ag nanocubes. Our preliminary results show that hydrophobic and hydrophilic ligands tend to displace polyvinylpyrrolidone (PVP) in an entirely different way, the first forming islands, the latter in a random process over the entire surface. Moreover, it can be used to rapidly map *in situ* the evolution of elasticity along the newly formed walls of dividing bacteria cells. Our preliminary results show that the process is fast and completed in approximately 20 min, a time frame that makes it very difficult for traditional Atomic Force Spectroscopy to characterize the entire interface in any level of detail.

1.3. References

- [1] A. Ulman, *An introduction to ultrathin organic films: From Langmuir-Blodgett to self-assembly*, 1st ed. Boston: Academic Press, 1991.
- [2] R. P. Feynman, "There's plenty of room at the bottom," *J. Microelectromech. Syst.*, vol. 1, no. 1. pp. 60–66, 1992.
- [3] G. Binnig and H. Rohrer, "Scanning tunneling microscopy," *Surf. Sci.*, vol. 126, no. 126, pp. 236–244, 1982.
- [4] G. Binnig and C. F. Quate, "Atomic Force Microscope," *Phys. Rev. Lett.*, vol. 56, no. 9, pp. 930–933, 1986.
- [5] R. G. Nuzzo and D. L. Allara, "Adsorption of bifunctional organic disulfides on gold surfaces," *J. Am. Chem. Soc.*, vol. 105, no. 13, pp. 4481–4483, 1983.
- [6] M. E. Cupery and D. Wilmington, "Substrate having an organic polymer containing pentavalent phosphorus bonded thereto," 3,013,904, 1961.

Chapter 2

Organic self-assembled monolayers

Organic SAMs are at the forefront of surface modification methods, due to their inherent manufacturability and reproducibility. Offering both a platform for basic science research and multiple applications, certain aspects of their formation have been extensively characterized; others still remain elusive. An accurate and thorough correlation between the synthetic procedure followed, the structure, and the properties of SAMs can provide a valuable tool for the conscious design of experiments addressing fundamental science questions, and large-scale processes aiming at surface modification at an industrial level. In this thesis the relationship between the deposition, structure and nanomechanical properties of SAMs of thiolated molecules on Au (111) and of alkylphosphonic acids on Al_2O_3 is being studied. My hypothesis is that nanomechanical characteristics of the SAMs can be correlated to the ordering of the ligands and that a commercially available bimodal AFM excitation scheme can be used as the means to accurately, reproducibly and rapidly measure the elasticity of SAM covered surfaces, E^* . This chapter is introduced by a general overview of the state of the art of SAM formation and characterization, in paragraph 2.1, simultaneously highlighting the areas where further development of the field is possible. The general scheme of SAM deposition is discussed in paragraph 2.2. The unique mode of bond formation between thiols and Au and phosphonic acids and Al_2O_3 is described in paragraphs 2.3 and 2.4, respectively. Aspects pertaining to the ordering of the monolayers are discussed in paragraph 2.5. The formation of binary SAMs, offering the possibility to further tailor surface properties, is discussed in paragraph 2.6. Lastly, the kinetic aspects of SAM formation and ordering are discussed in paragraph 2.7.

2.1. Introduction to organic self-assembled monolayers (SAMs)

Organic self-assembled monolayers (SAMs) are ordered molecular assemblies of active compounds, called ligands, spontaneously adsorbed on suitable surfaces, or substrates [1]. This simple synthetic process makes them inherently manufacturable and reproducible, altering the properties of surfaces while leaving the bulk of the substrate unaffected. They offer a unique platform for surface engineering, aiming at basic science research and real-life applications alike.

The properties of SAMs depend, on a fundamental level, on two parameters: their elemental composition and their structure. In this thesis the relationship between synthetic parameters, monolayer structure and nanomechanical properties will be investigated. The interest in the nanomechanical properties stems from the fact that elasticity is a feature of materials related to the arrangement of their atoms and molecules. It is therefore hypothesized that a variation in Young's moduli between different SAMs would indicate differences related to the degree of ordering of the ligands. The monolayers studied are thiol SAMs on Au (111) and alkylphosphonic acid SAMs on Al_2O_3 .

The structure of SAMs is largely determined by the structure of the individual ligands, their arrangement and ordering, and the experimental conditions selected; most notably, time.

A number of researchers have reported the formation of ordered, crystalline SAMs, particularly in the case of thiols [2]–[9]. The degree of ordering has been reported to vary with the length of the used ligands, but studies on the elasticity of thiol SAMs, both computational and via Atomic Force Spectroscopy, show a great discrepancy in their findings [3], [10]–[14].

Regarding the molecular ordering of phosphonic acid SAMs, the general consensus is that both ordered and amorphous phases are possible [15]–[19]; but the conditions under which they can form [19]–[26], as well as the actual stability of the SAMs [27]–[35], remain a source of debate. A study of the temporal evolution of these SAMs from the amorphous to the ordered state, and the corresponding structural characteristics of the formed structures, has so far not been performed. No investigation of the elasticity of alkylphosphonic acid SAMs has been performed either.

Another attractive feature of SAMs is the possibility to further tailor their properties by combining two ligands. Numerous theoretical studies have addressed the thermodynamic behavior of binary thiol SAMs on gold substrates, showing that the two

ligands can mix, form domains, or entirely phase separate [36]–[40]. At the moment however, it is experimentally very difficult to localize each ligand on a surface, particularly when the formed domains are smaller than 10 nm. If, however, SAMs of different ligands exhibit different mechanical properties at the nanoscale, the localization of the molecules in a binary SAM could be performed by mapping this variation with high lateral resolution.

In the following paragraphs of this chapter the well-established aspects of SAMs' formation and ordering will be discussed; at the same time the possibilities for further developments in the field will be illustrated, focusing on the nanomechanical variations between SAMs. The characterization of the nanomechanical properties of molecularly thin, largely disordered organic materials grown on much stiffer substrates is, however, not trivial. Furthermore, direct correlation between topographical and mechanical features on a surface cannot be readily achieved. In the present thesis the use of the Atomic Force Microscope (AFM) under bimodal excitation and detection mode (bimodal AFM) as a sensitive, fast and non-destructive technique, combining the high lateral resolution of conventional dynamic AFM with the accurate description of the elasticity of the first few atomic layers of a complex, multilayered surface is proposed. The experimental results presented in Chapters 4 and 5 demonstrate that the technique allowed for accurate characterization of surface elasticity in SAMs, as well as the way it scales with varying ligand length, monolayer formation time and monolayer ordering.

2.2. Deposition of SAMs

The ligands can be deposited on the substrate from a gas or liquid phase. Liquid phase deposition by immersion of the substrates in a suitable ligand solution is by far the most used method as it is easily applicable and does not require any sophisticated equipment. Gas phase deposition would typically yield better ordered SAMs and could circumvent some problems such as solvent effects and multilayer formation. However, it requires specially designed reactors and constant gas flow lines and is therefore not the preferred deposition method.

SAM solution deposition, as shown in Figure 2.1, typically involves three steps: a) initial ligand physisorption on the surface, b) ligand chemisorption or desorption back into solution, and c) spontaneous ligand reorganization and ordering, as the system approaches equilibrium [41]. The headgroup provides the most exothermic process by reacting with the exposed molecules or atoms of the surface forming covalent bonds, pinning each ligand molecule into place on the surface. Interchain interactions between

the spacer chains result in a higher or lower degree of two-dimensional order. It should be noted that interchain interactions alone are by no means adequate to form an ordered monolayer; rather, they supplement the ordering allowed by the layer configuration created by the specific bounding sites of the headgroup. Once the previously described process has taken place resulting in a monolayer, the exposed terminal group determines the functionality of the surface [1].

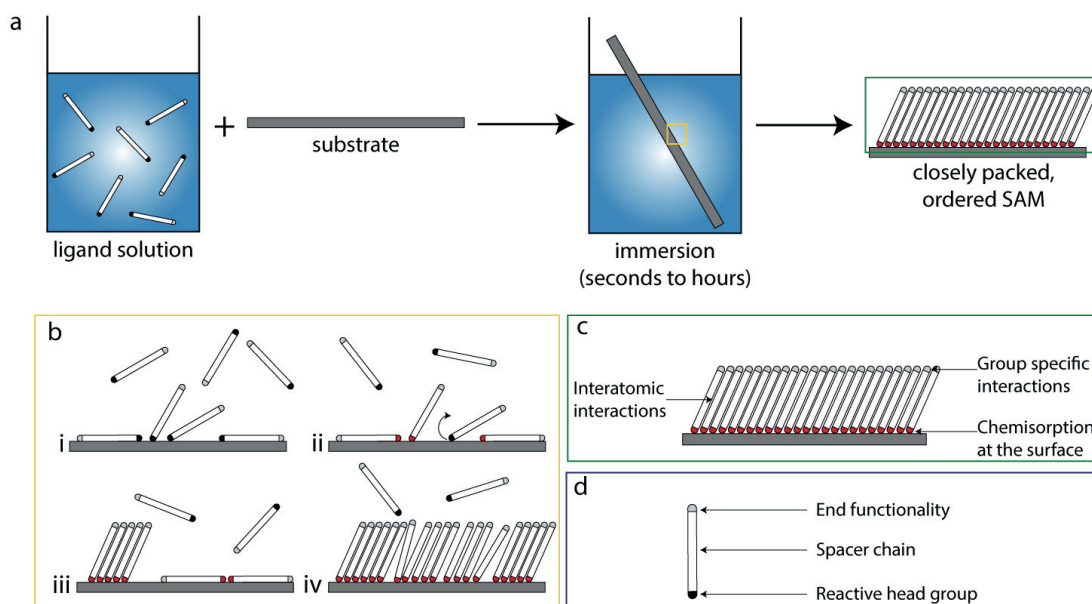


Figure 2.1: Simplified general process of SAM deposition from solution (a) and schematic representation of a ligand molecule (inset d). The substrate is immersed in a ligand solution for a set time period. The ligand molecules are initially physisorbed (inset b, i). Some molecules react with the surface via the reactive headgroup and are chemisorbed, while others are desorbed back to solution (inset b, ii). Under the influence of interatomic forces, the initially disorganized, lying-down ligand molecules begin standing up, creating ordered domains (inset b, iii). Additional ligand molecules are adsorbed in the free surface binding sites and the formation of ordered domains expands to the entire surface (inset b, iv). The resulting SAM is a closely packed, well ordered molecularly thin structure, chemically attached to the substrate (inset c). The ligand end functionality is exposed to the environment.

The simple synthetic procedure followed for SAM deposition from solution makes them inherently manufacturable and thus technologically attractive. All parts of the ligand can be selected in order to accommodate the particular needs of each application. The headgroup dictates to which surfaces the ligands can chemisorb.

2.3. Thiol SAMs on Au (111)

Perhaps the most widely studied and better understood self-assembly system, thiol SAMs on Au (111) surfaces have been a model system for most studies, ever since the pioneering study of Nuzzo and Allara that first described the spontaneous formation of

organized monolayers of disulphides on zerovalent Au surfaces [42]. Thiols are organosulfur compounds with a carbon-bonded sulfhydryl group and the general structure R-SH. They coordinate strongly to a number of metals, including silver, copper and platinum, as well as GaAs and InP [41]. Alkanethiolates have been shown to form highly organized, well-ordered monolayers reproducibly, always leaving the ω -functionalized end exposed to the environment, thus constituting an ideal system to probe basic surface science problems [43].

2.3.1. The Au-thiolate interface: Binding mechanism, in-plane diffusion and interfacial disorder

The question of the bond formation between the -SH headgroup and the Au substrate is one highly debated and still not fully understood, especially as far as the lateral position of the S atoms at the S-Au(111) interface are concerned. The model initially proposed [43] entails the adsorption of the ligand on the surface and loss of the thiol hydrogen, which, in turn, desorbs from the surface as H₂. The presumed product of the reaction is a gold(I) thiolate (RSAu) adsorbed on metallic Au(0). It has been hypothesized that the S atoms of the -SH headgroup are bound to the three-fold hollow sites of the Au(111) lattice, forming a hexagonal $\sqrt{3}\times\sqrt{3}$ R30° overlayer commensurate with the underlying structure of Au (111) [44], known as the “standard model”. The standard model was supported by quantum chemical calculations and the fact that S is known to adsorb on highly coordinated sites on transition metals. The $\sqrt{3}\times\sqrt{3}$ R30° mesh has been experimentally observed via early studies [45]; however, these results pertain only to the location of the spacer chain and not the lateral position of the S headgroups [46]–[48]. Later studies [49] showed the existence of a rectangular unit mesh containing four molecules in two indistinguishable pairs. This c(4×2) superlattice indicates that there are in fact two possible binding configurations of the S headgroup, instead of the one proposed by the standard model. X-ray crystallography and Sum-Frequency Generation (SFG) [50] data have also shown that the symmetry of an alkanethiol monolayer consists of a hexagonal lattice of the spacer alkyl chains and a pairing of the S head groups, leading to the hypothesis of the sulphur pairing model and further contradicting the standard model. Subsequent simulations investigating the spacing of the S species at the S-Au (111) interface are in good agreement with the experimental results [51], [52]. It should be noted that these studies have accounted for possible S-S interactions; simulations where these interactions are ignored [53]–[55] yield inconclusive results, not in agreement with experimentally observed structures. An X-ray Standing Wave

(XSW) study by Fenter et al. demonstrated further excluded the possibility of a single binding site model and proposed instead the formation of a chemical bond between the S headgroup and the Au atom of the substrate directly beneath it, along with a S-S pairing. There is no chemical interaction between the second S atom and the underlying Au atom [56].

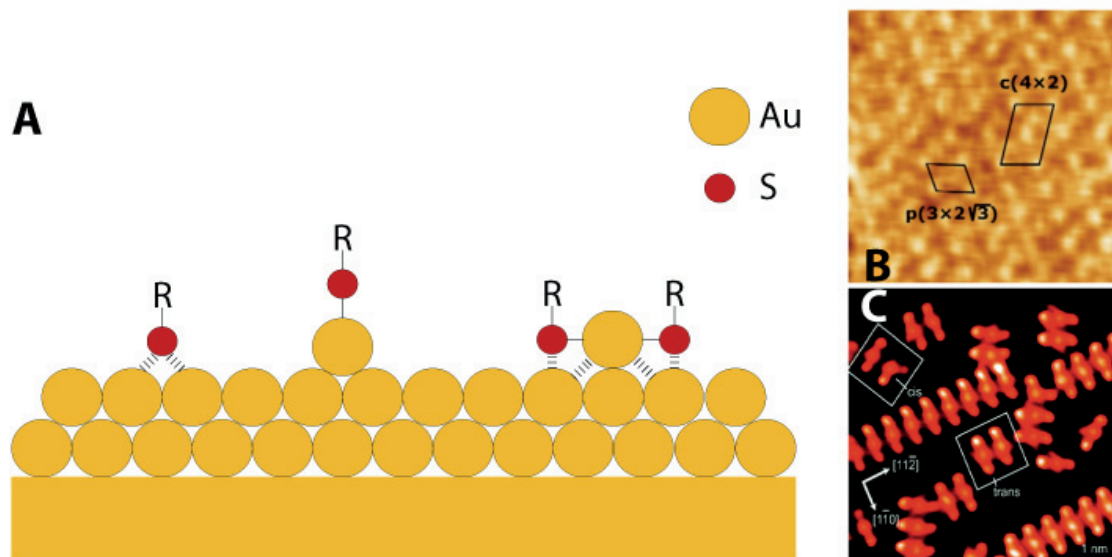


Figure 1.2 (A-C): Some of the reported Au-S binding modes (A). From left to right, the standard model, an Au adatom-thiolate complex, and the RS – Au_{ad} – SR complex. More than one binding mode can coexist in a single SAM. STM image of a dodecanethiol SAM on Au (111) showing two possible configurations of the ligand, in the $\sqrt{3} \times \sqrt{3}$ and the $c(4 \times 2)$ lattice (B). STM image of methylthiolate adsorbed at low coverage on Au (111), showing two *trans* $(\text{CH}_3)_2\text{S}$ complexes and one *cis* and one *trans* adatom complexes. Image B reproduced from <http://www.physics.mcgill.ca/~SPM/sensor/AfMgold.htm>, image C reproduced with permission from reference [44].

Recent studies have shown that the formation of a thiol SAM is accompanied by significant surface reconstruction [57], [58]. Experimental results indicate that the topmost Au layer can be modeled as a layer including delocalized vacancies and adatoms, leading to a dynamically restructured S-Au(111) interface. A 2006 study by Maksymovych et al. proposed the model of two S headgroups forming one bond with the Au adatom located slightly above a twofold bridge-site, and each forming one more with an underlying lattice Au atom [59]. Additional support for the hypothesis of the RS-Au_{ad}-SR complex formation has been provided by a number of simulations and theoretical calculations [6], [57], [60]–[63].

In spite of the multiple theories and models addressing the S-Au bond, its exact nature has yet to be determined. It is clear however that its dynamic nature has significant implications in the evolution of SAMs' surface morphology. The diffusion of thiols on

the free Au(111) surface directly impacts SAM formation density. In-plane diffusion of thiolates within an already formed SAM and subsequent energetically favorable ligand reorganization directs ligand packing and, in the case of mixed ligand monolayers, phase separation or mixing. Lastly, the diffusion of Au atoms leads to an overall restructuring of the surface, and can lead to or heal surface defects [44].

2.4. Alkylphosphonic acid SAMs on Al₂O₃

Aluminium is one of the most technologically relevant materials in use today. From transportation to food packaging and from construction to microelectronics, it is the most heavily consumed non-ferrous metal in the world, with the annual production for 2016 reaching almost 59 million metric tons [64]. Al₂O₃, both the inert, brittle material extracted from bauxite and used for aluminium production and the passivating layer that under equilibrium conditions covers the surface of aluminium, can be used as an insulator, filler, abrasive or even catalyst. Given the high technological importance of aluminium and Al₂O₃, it is not surprising that surface SAM depositions would aim at these materials, and knowledge gained from the study of thiol SAMs would be transferred to this new system.

Al₂O₃ surfaces are in general polar structures. *Ab initio* thermodynamics and Density Functional Theory (DFT) simulations show that a fully hydroxylated surface is the thermodynamically stable state for Al₂O₃ [65], [66]. Suitable ligands for the deposition of SAMs on Al₂O₃ should be molecules with headgroups able to react with the surface hydroxyls, such as silanes, carboxylic acids, and phosphonic acids.

Chloro- or alkoxysilanes can react rapidly with hydroxylated surfaces to form monolayers, but can also self-polymerize, resulting in multilayer structures difficult to control [67], [68]. Carboxylic acids react with hydroxylated surfaces in a much slower and more controllable way than silanes, but have the disadvantage of forming largely reversible bonds with the surface –OH groups, thus leading to unstable SAMs [69], [70]. Between the two, one can find organophosphonic acids. Less reactive than silanes but leading to better chemisorbed monolayers than carboxylic acids, they are a prime candidate for SAM deposition on metal oxides.

Alkylphosphonic acids are organic phosphorus compounds having the –PO(OH)₂ moiety. This moiety, being the reactive headgroup of the ligand, can readily react with the hydroxylated surfaces of oxides, such as Al₂O₃, SiO₂ and TiO₂, via simple condensation reactions.

2.4.1. Binding mechanism

Organophosphonic acids can be bound to hydroxylated MeO_x surfaces initially via physical interactions, such as hydrogen bond formation between the $-\text{OH}$ moieties of the $-\text{PO}(\text{OH})_2$ group and the surface, and at a later stage via mono-, bi- and/or tridentate binding [71]–[74]. A recent study by Bauer et al. has explored in depth the nature of the formed bonds between Al_2O_3 and phosphonic acids. Protonation of surface $-\text{OH}$ groups by the $-\text{PO}(\text{OH})_2$ groups leads to an elimination acid-base reaction, allowing the formation of mono- and bidentate bonds. The third bond is formed when “a dissociated water molecule reassembles in order to provide an empty adsorption site for the oxygen atom” from the $-\text{PO}(\text{OH})_2$ groups [72], as shown in Figure 2.3.

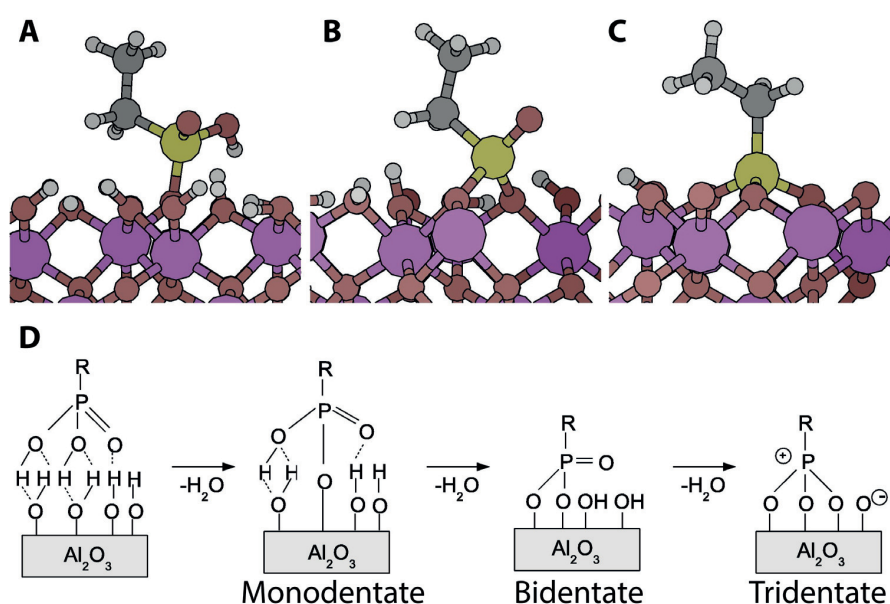


Figure 2.3: Schematic representation of steric configuration of monodentate (a), tridentate (b) and tridentate (c) coordination of ethylphosphonic acid on the surface of Al_2O_3 C-plane (0001). O atoms are brown, Al atoms are violet, H atoms are grey and P atoms are green. Stepwise condensation reaction between the phosphonic acid headgroup and the Al_2O_3 surface (d). Reproduced with permission from reference [71].

The stability of the formed bonds and, conversely, the resulting SAMs, depends on three main parameters: a) the interfacial bonding types, b) the adsorption free energy of the $-\text{PO}(\text{OH})_2$ group in comparison to the solvent, and c) the local adsorption geometry.

In a work by Thissen et al. [27] the nature of the bonding between the $-\text{PO}(\text{OH})_2$ headgroup and different configurations was determined via Polarization Modulation-Infrared Reflection-Adsorption Spectroscopy (PM-IRRAS) and Diffuse Reflectance Infrared Fourier Transform Spectroscopy (DRIFT). PM-IRRAS spectra recorded for octadecylphosphonic acid SAMs grown on native, amorphous Al_2O_3 and DRIFT spectra recorded for the Al_2O_3 R-plane ($1\bar{1}02$) indicate that bidentate covalent bonding between

the ligand and surface is preferable. In contrast, ionic bonding between deprotonated -PO_3 and surface Al atoms is favored in the case of Al_2O_3 C-plane (0001), leaving the SAMs more susceptible to desorption into a polar medium [75].

Molecular Dynamics (MD) simulations have shown that polar solvents exhibit a certain affinity towards the polar Al_2O_3 surfaces, forming a dense interface through a H-bond network, patterned by the crystalline structure of the substrate [76]. As experimentally shown by Chen et al., the higher the dielectric constant of a solvent, the higher its affinity towards the surface, occupying binding sites which the phosphonic acids might occupy, possibly leading to a local free energy minimum. For the system to reach a global energy minimum, the solvent molecules must be displaced from the interface by the ligand. Studies have shown that SAMs formed on oxide-terminated surfaces from solvents with a high dielectric constants exhibit a higher defect density than their counterparts deposited from lower polarity solvents [27]–[29], [77]–[80].

The geometrical configuration of the substrate surface also has a significant role in the number of allowed bonds. The distance between the P in the -PO(OH)_2 and the underlying Al ions is crucial for the stability of the binding geometry [27], [73], [81]; the larger the P-Al distance, the more stable the bonding mode [71].

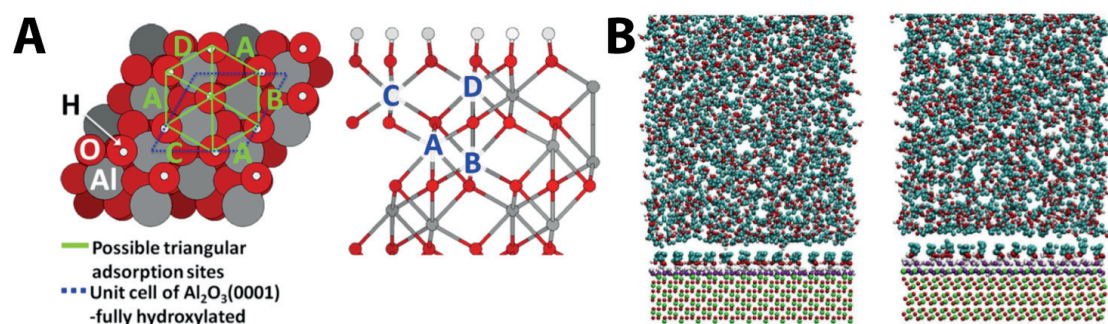


Figure 2.4 (A, B): Surface lattice and used solvent are parameters that can affect the structure and stability of alkanethiol SAMs. Top view of the fully hydroxylated Al_2O_3 C-plane (0001) surface with all possible triangular adsorption sites (A, left). Side view of the fully hydroxylated Al_2O_3 C-plane (0001) surface showing the position of the underlying Al ion for all possible triangular adsorption sites (A, right). The tridentate adsorption of phosphonic acids is only possible in the adsorption sites A and B, while for binding sites C and D bidentate bonding is the thermodynamic ground state. Reproduced with permission from reference [81]. Simulation snapshots for ethanol on Al_2O_3 C-plane (0001) (left) and R-plane ($1\bar{1}02$) (right) showing the formation of a dense solvent layer at the surface-solvent interface. Green and red spheres represent aluminum and oxygen atoms in the bulk structure, respectively. For both surfaces, surface hydroxyl groups are illustrated using purple for oxygen and white for hydrogen atoms. Ethanol molecules are represented using cyan, red and white spheres for methyl (ethyl) groups, oxygen and hydrogen atoms, respectively. Reproduced with permission from reference [76].

2.5. Variations in ligand ordering and packing density

The degree of ordering and molecular packing within SAMs significantly affects material properties such as wetting, friction [4], adhesion, and elasticity [3], [10]–[14], to name a few. Increase of ligand length, particularly for ligands with alkyl chains, leads to SAMs of increased order. The addition of bulky or rigid moieties in spacer chains typically leads to a decrease in ligand density, usually due to steric hindrance or unfavorable intermolecular interactions. Charged end groups can enhance SAM ordering via intermolecular interactions between neighboring moieties [4], or electrostatic repulsive forces can lead to more disordered structures [19]. The roughness and density of binding sites of the substrate can also affect the ligand packing density and order.

2.5.1. Ligand length

Interatomic interactions between neighboring spacer chains are the main driving force for a ligand ordering within SAMs, particularly in the case of alkyl chains. As a general trend, the addition of $-\text{CH}_2$ groups in a chain leads to an increase in attractive van der Waals interactions between neighboring ligands, stabilizing the chains into a configuration more perpendicular to the surface. Alkanethiols with fewer than three carbons in the alkyl spacer chain have been observed to form (3×4) lattices formed by the $\text{RS-Au}_{\text{ad}}\text{-SR}$ complex in the *trans* configuration [2]. For longer alkyl chains ($3 < n \leq 12$) [3], chain-chain van der Waals interactions lead to a significant energy gain for the system, as opposed to S-Au interactions, minimizing the tilt of the chains towards the surface, leading to a more perpendicular orientation and enhancing overall ordering with fewer *gauche* defects [4], [5]. Moreover, the $c(4\times 2)$ lattice is increasingly observed, with an orthorhombic *cis* packing structure [6]. As the number of carbons in the alkyl chain increases further, areas exhibiting the standard model-proposed, $\sqrt{3}\times\sqrt{3}\text{R}30^\circ$ monoclinic packing structure appear more frequently, as this arrangement allows for better optimization of the van der Waals interactions than the $c(4\times 2)$ configuration [7]. Experimental studies of octanethiol SAMs have shown the coexistence of both $\sqrt{3}\times\sqrt{3}\text{R}30^\circ$ and $c(4\times 2)$ phases [8]. Mild thermal annealing of the SAMs has been shown to promote the reorganization of the ligands to one, thermodynamically favorable, phase of increased order and packing density [9].

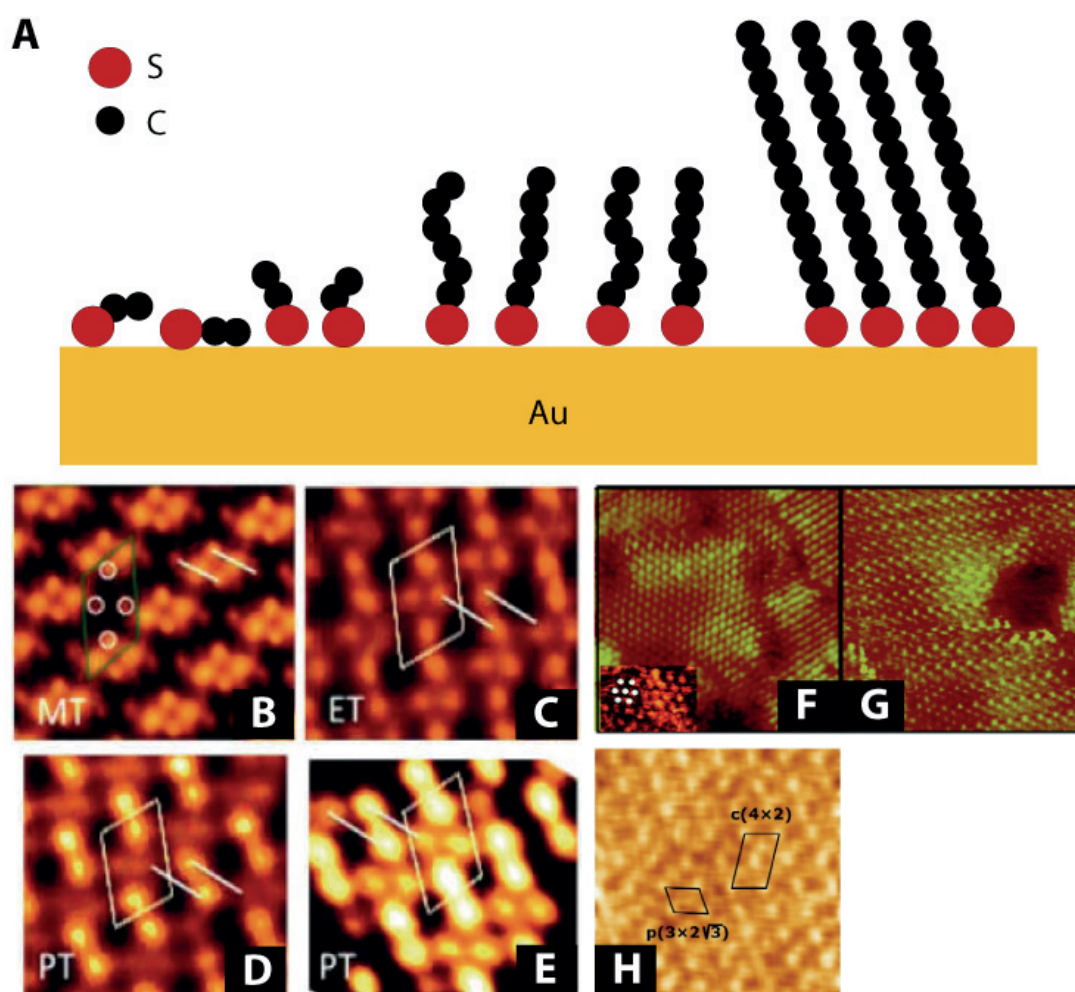


Figure 2.5 (A-H): Schematic representation of molecular ordering in alkanethiol SAMs for ligands of different length (A). For short-chain alkanethiols substrate-chain forces are dominant and the ligands are almost parallel to the substrate. As ligand length increases, interatomic forces promote ordering. Denser packing of better-ordered ligands leads to different thiol lattices. STM images of the 3×4 phase of methylthiolate (B), ethylthiolate (C), and propylthiolate (D, E) SAMs. The white bars in each image are used to highlight the Au-atom-dithiolate unit. Adapted with permission from reference [2]. STM images of the $\sqrt{3} \times \sqrt{3}$ R30° lattice in a decanethiol SAM (the inset shows the same lattice on nonanedithiol) (F) and a rectangular c(4x2) lattice in a hexanethiol SAM (G). Adapted with permission from reference [82]. The two phases coexist in a highly ordered dodecanethiol SAM. Reproduced from <http://www.physics.mcgill.ca/~SPM/sensor/AfMgold.htm>.

Alkylphosphonic acid SAMs with $10 \leq n \leq 13$ were found by Spori et al. to self-assemble in relatively sparse and disordered SAMs. Stabilization of these shorter spacer chains was mainly provided by interatomic interactions with the surface, leading to lower packing density and order. For longer alky chains ($16 \leq n \leq 18$) the formation of closer packed, denser SAMs was favored. It should be noted that X-ray Photoelectron Spectroscopy (XPS) results indicated the favorable mono- or bidentate binding in the denser monolayers, a conformation energetically more favorable [15]. Expanding on

these observations, Fukuda et al. fabricated thin film transistors (TFTs) with gate dielectrics made of alkylphosphonic acid SAMs grown on amorphous Al_2O_3 and their performance was correlated to ligand ordering. The performance of the TFTs was measured and found to increase with increasing ligand length, reaching a maximum for $n = 14$. Shorter alkylphosphonic acids have a higher defect concentration within the SAMs, possibly due to lack of cohesive interactions between neighboring ligand molecules. Somewhat surprisingly, alkyl chains with $16 \leq n \leq 18$ appear to also increase the concentration of *gauche* defects, this time near the SAM-environment interface [16]. An increase in monolayer ordering with increasing ligand length was also found by Losego et al. for alkylphosphonic acid SAMs grown on ITO via Near-edge X-ray Absorption Fine Structure (NEXAFS). It was also demonstrated that the roughness of the unmodified surface significantly affected tilt angle and molecular ordering in the deposited SAMs [17]. A theoretical study by Lushtinetz et al. confirmed the experimentally observed order enhancement by increased ligand length in alkylphosphonic acid SAMs on Al_2O_3 , while also providing an insight in the effect of the binding mode and surface structure to SAM ordering. The density of available binding sites on a surface, as discussed in paragraph 2.4.1, limits the concentration of phosphonic acids in a SAM, such that the maximum theoretical packing of the alkyl chains cannot be reached. Moreover, monodentate binding allows for a greater number of ligand chains to chemisorb on the surface, but the rotational flexibility of this binding mode increases the disorder of the SAMs. On the other end of the spectrum, rigid tridentate bonding limits the maximum number of ligands that can be adsorbed, leading to a sparser monolayer, but, as it also does not allow for any rotational movement, promoting molecular ordering within the monolayer [18].

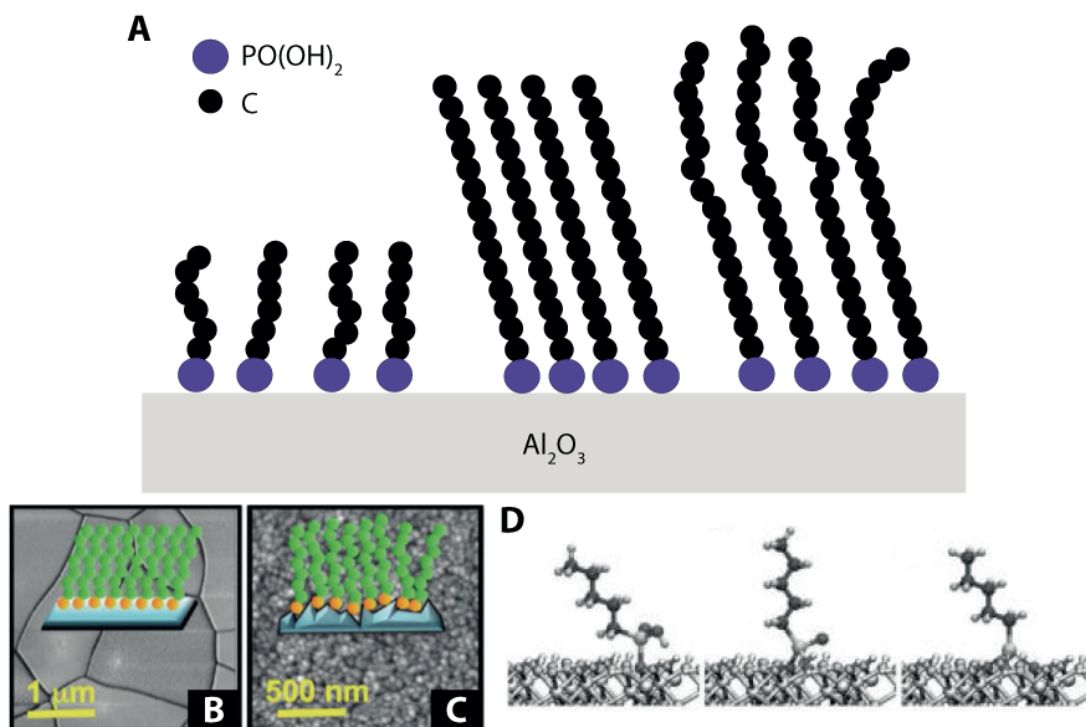


Figure 2.6 (A-D): Schematic representation of molecular ordering in alkylphosphonic acid SAMs for ligands of different length (A). SAMs where the ligand has fewer than 10 C are reported to be disordered. As ligand length increases, so does molecular ordering, under the influence of neighbor-neighbor chain interactions. For ligands with more than 16 C defects are introduced at the SAM-environment interface. Low surface roughness promotes ordering in alkylphosphonic acid SAMs on metal oxides (B, C). Adapted with permission from reference [15]. Monodentate and bidentate bound phosphonic acids are free to rotate and tilt, introducing disorder to the SAMs, while tridentate bonding results in a rigid configuration (D). Image adapted with permission from reference [18].

2.5.2. Effect of spacer chains and end functionalities

Thiol SAMs with polar terminal groups such as $-\text{OH}$ and $-\text{COOH}$ appear to lead to better ligand ordering irrespective of the spacer chain length, possibly as an effect of hydrogen bonding between the end functionalities [4]. Small and bulky ligands on the other hand, such as mercaptobenzoic acid [83], 6-mercaptapurine [84], and mercaptosuccinic acid [85] tend to form sparse SAMs, demonstrating the effect of steric hindrance in ligand packing.

Similarly, X-ray Reflectivity (XRR) results for phosphonic acid SAMs reported by Khassanov et al. confirmed that while long alkyl chains tend to form crystalline domains, the inclusion of charged, fluorinated groups or rigid benzo[b]benzo[4, 5]thieno[2, 3-d]thiopheny-2-yl (BTBT) groups lead to a molecular tilt in respect to the surface plane and a lower ligand density. SAM assembly from ligands with the bulky fullerene end group was dominated by the steric requirements of the fullerene and were thus

inherently sparse and disordered. The inclusion of simple alkyl chain phosphonic acids in C60-PA SAMs enhances the overall molecular ordering and packing density [19].

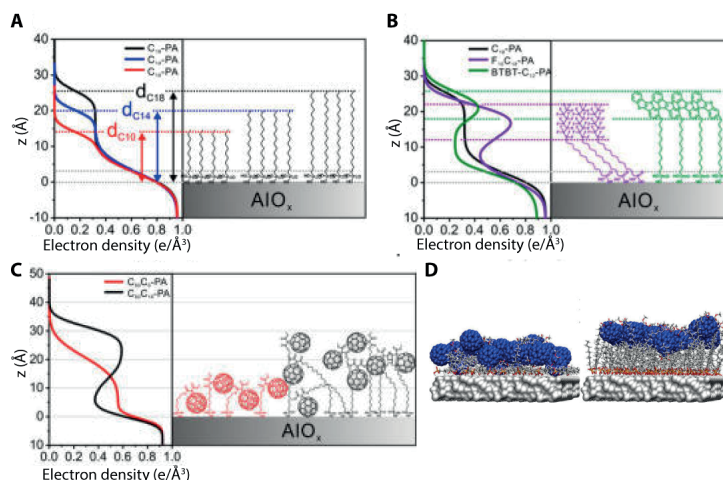


Figure 2.7 (A-D): XRR determined electron density profiles and predicted structures for SAMs of alkylphosphonic acids (A), phosphonic acids terminated with fluorinated groups and rigid BTBT groups (B) and phosphonic acids terminated with fullerenes (C). Reproduced with permission from reference [19]. The inclusion of bulky and/or rigid groups in the ligand chains reduces overall ordering. Interestingly, linear alkylphosphonic acid molecules can act as spacers in SAMs of bulky molecules, increasing anew the ordering of the system, as evident from MD simulations of binary C60-octadecylphosphonic acid:decanephosphonic acid SAMs (D). Reproduced with permission from reference [86].

2.5.3. Substrate effect

The density of the adsorbed species in a SAM is significantly affected by the density of the available binding sites and the roughness of the substrate itself (see Figure 2.6 D). A theoretical study by Lushtinetz et al. confirmed the experimentally observed order enhancing by increased ligand length in alkylphosphonic acid SAMs on Al_2O_3 , while also providing an insight in the effect of the binding mode and surface structure to SAM ordering. The density of available binding sites on a surface, as discussed in paragraph 2.4.1, limits the concentration of phosphonic acids in a SAM, such that the maximum theoretical packing of the alkyl chains cannot be reached. Moreover, monodentate binding allows for a greater number of ligand chains to chemisorb on the surface, but the rotational flexibility of this binding mode increases the disorder of the SAMs. On the other end of the spectrum, rigid tridentate bonding limits the maximum number of ligands that can be adsorbed, leading to a relatively sparser monolayer, but as it also does not allow for any rotational movement promoting molecular ordering within the monolayer [18].

2.5.4. The role of bimodal AFM in determining ligand packing and ordering

As discussed in paragraphs 2.5.1, 2.5.2 and 2.5.3, most experimental studies presented typically make use of spectroscopic techniques, often requiring high-energy radiation sources, and high resolution scanning probe microscopy in order to deduce the configuration of the molecules within a SAM. A different path, requiring less sophisticated equipment, would be the experimental observation of properties such as wetting, friction [4], adhesion and elasticity [3], [10]–[14], and their subsequent correlation to structural differences between SAMs of different ligands. This approach can provide valuable information on the effect of small changes in ligand characteristics to molecular ordering within SAMs, especially in comparative studies. In this work the variation of elasticity between SAMs of varying length and with different end functionalities has been determined via bimodal AFM and correlated to structural differences within the different thiol SAMs studied.

2.6. Binary thiol SAMs: Phase separation and mixing

The use of multiple ligands within a SAM can lead to smoothly tunable surfaces, combining more than two functionalities in a manner tailored to particular needs and applications. Mixed ligand SAMs can be formed via coadsorption or desorption and subsequent adsorption of a different ligand (place-exchange). While mixed ligand SAMs can be deposited on any substrate and with any ligand, the thiol-gold system is of particular interest. The mobility of the Au-S species, as discussed in paragraph 2.3.1, allows mixed ligand SAMs to exhibit phase separation or ligand mixing, as directed in each case by the interplay between enthalpic and entropic contributions towards free energy minimization. Ligands of significantly differing height or bulkiness tend to lead to phase separation in gold nanoparticles [36], [37], [87], and in quenched SAMs on flat surfaces [38], [87], [88]. Mixed ligand SAMs on flat Au surfaces of alkanethiols of similar lengths are reported to mix completely, as any entropic gain caused by phase separation is minimal [39]. The addition of a polar moiety in the spacer chain however can lead to phase separation, as demonstrated by Smith et al. [40]. In their study they prepared mixed ligand SAMs via coadsorption of n-decanethiol and an amide-containing alkanethiol of similar length (3-mercapto-N-nonylpropionamide) using different feed solution molar ratios. Phase separation, observed for all tested molar ratios, was driven by free energy minimization; separating the polar group containing molecules from the crystalline domains of the alkanethiol lead to a significant enthalpy gain.

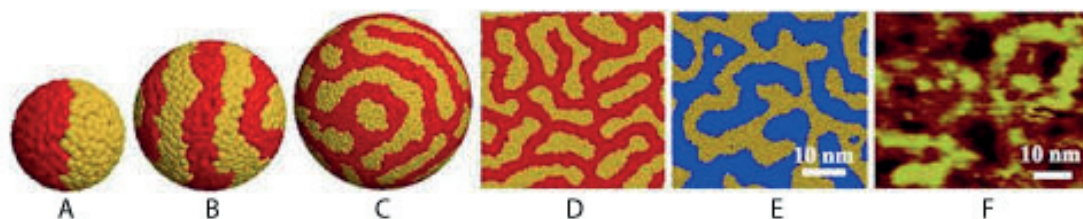


Figure 2.8 (A-F): Atomistic simulations results of phase separated equilibrium structures of binary monolayers of surfactants (A-D) and C4:C6 thiols. STM height image of C4:C6 binary SAM showing phase separation and domain formation. Reproduced with permission from reference [87].

2.6.1. The role of bimodal AFM in mixed ligand SAM characterization

The experimental verification of the theoretical studies on mixed ligand SAMs is a widely debated research topic. The presence of different chemical species within a SAM can be chemically verified by most chemical recognition techniques for powder and liquid samples, but only a handful of those can be used for SAMs on flat surfaces. Furthermore, the localization of molecules and domains on a surface remains equivocal. Experimental studies address domain observation on SAMs on flat gold surfaces by Scanning Probe Microscopy (SPM) imaging, where height differences are attributed to expected length differences between the used ligands or standing-up and lying-down phases. Techniques offering actual chemical recognition on the surface, like Atomic Force Microscope Infrared-Spectroscopy (AFM-IR) and Atomic Force Microscope Time of Flight Secondary Ion Mass Spectrometry (AFM-TOF-SIMS) have a lateral resolution limit too large for the typical size of formed domains. A microscopy technique that allows the user to locate the chemically different domains on a surface with high lateral resolution can address the uncertainty that currently prevails all the experimentally available data.

The high lateral resolution of AFM operated in a dynamic mode makes it a prime candidate for characterization of nanodomains. As bimodal AFM exhibits high sensitivity to material properties, it can be used to locate mechanical variations on mixed ligand SAMs. Any observed differences in the recorded elasticity can then be directly attributed to topographical features, revealing the local chemical composition of the studied SAMs.

2.7. Kinetics and stability of SAMs and multilayer formation

2.7.1. Kinetics and stability of SAMs

The kinetics of thiol and alkylphosphonic acid SAMs' formation are in general two rather different processes, mainly due to the largely irreversible bonding of the -PO(OH)_2 with surface -OH species, as opposed to the formation of highly mobile S-Au bonds.

The temporal evolution of thiol SAM formation and ordering via incubation in a ligand solution can be viewed as a three-step process, with the consecutive steps originating from the surface and moving towards the film surface, as shown in Figure 2.9. The first step, initial adsorption of ligands to the gold surface and formation of S-Au bonds, has been discussed in paragraph 2.3.1. During this rapid step, typically lasting less than 5 min [89], [90], patches of disordered molecules are formed and etch pits appear on the gold surface [91]–[93]. During the second step, low-ligand density, lying-down phases of initially ordered ligands [82], [91], [92], [94]–[96], perpendicular to the surface normal-plane, are formed. The lying-down phases can exhibit different degrees of ordering, the most common of which are a head-head/tail-tail configuration (striped configuration) and the arrangement of alkyl chains in adjacent rows, with an out of plain interdigitated configuration [93], [95], [96]. Ordered lying-down phases can coexist with amorphous, liquid-like phases. At increased adsorbed ligand concentration, the system evolves to formation of higher density, close-packed standing-up phases [5], [93], with the ligands' alkyl chains exhibiting a tilt of approximately 30° relative to the surface normal plane [97]–[99]. The transition from lying-down to standing-up phases is driven by free energy minimization via S-Au bond formation and van der Waals interactions between neighboring alkyl chains [4], [7]. The third reported step of thiol SAM formation takes place at long monolayer formation times and entails the orientation and aligning of the end functionalities in the standing-up phases [89], [90].

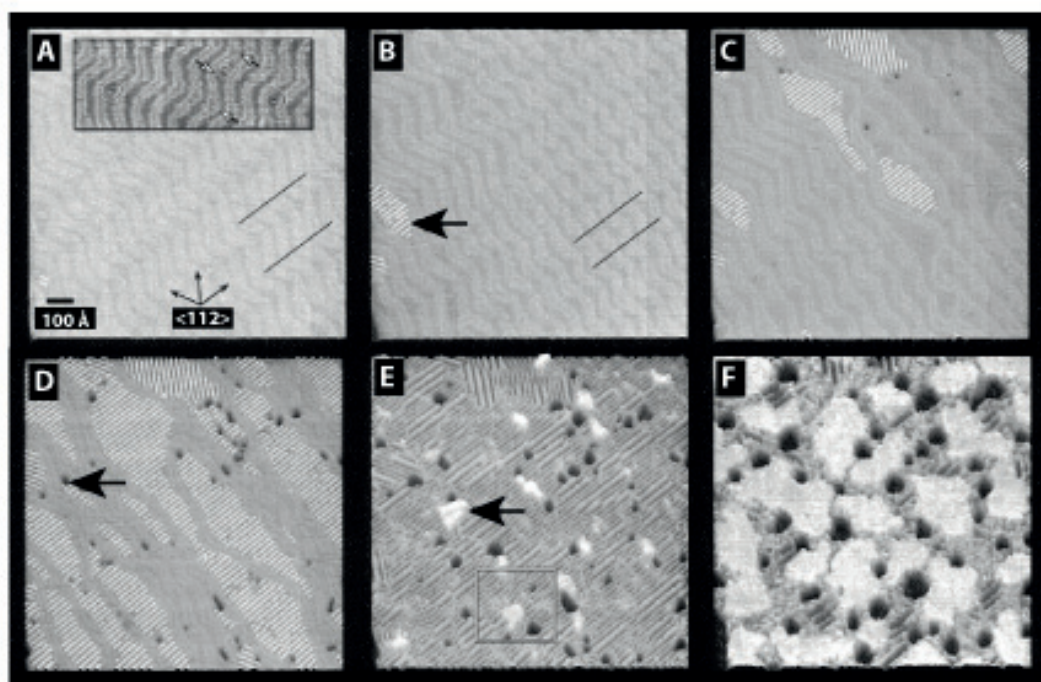


Figure 2.9 (A-F): Constant current STM topography images for increasing exposures of Au (111) surface to mercaptohexanol vapour. Clean $((22\times\sqrt{3})$ “herringbone” reconstructed) Au (111) surface (A). Striped phase island formation (arrow) (B) and continued striped phase growth displacing herringbone elbows (C). Continued striped phase growth with Au pits (arrow) formation becoming visible (D). Nucleation of standing-up phase (square and arrow) within striped lying-down phase (E) and subsequent growth of standing-up phase at the expense of the striped phase until saturation (F). Adapted with permission from reference [68].

The temporal evolution of phosphonic acid SAMs formation is a topic still under study and discussion. *In situ* AFM studies have shown that initially disordered patches are formed, which gradually grow and eventually coalesce [20]. Following the formation of a SAM, multilayer islands are formed [21]–[23], following the Stranski-Krastanov model [24], [100]. Other studies however have not observed the formation of multilayers and proposed that in the same or longer time frame only monolayers are formed [19], [25], [26]. An equally great disparity can be found in the available information regarding the conditions that allow ligand organization and SAM ordering and the overall stability of the SAMs. Numerous studies on alkylphosphonic acid adsorption on Al_2O_3 by various groups have found SAMs formed by ligands of various length to be extremely stable over time [30], in ambient conditions and aqueous environments [27], [28], at acidic and alkaline pH [31], and under small mechanical loads [32]. In contrast, a study by Hauffman et al. has shown that SAMs formed from ethanolic solutions of octylphosphonic acid are unstable and quick to dissolve, at the same time etching the underlying native oxide [33], while a study by Branch et al. also found that octadecylphosphonic acid SAMs lack long-term stability in aqueous environments [34].

Other studies have further shown that a thermal annealing step is necessary to induce covalent bonding between the headgroup and the substrate [29], also for alkylphosphonic acid SAMs on other oxide surfaces [35].

2.7.2. Multilayer formation

Multilayer formation can be either a physical or chemical process. The formation of chemically bound multilayers is usually controlled and guided by the careful selection of a reactive or chelating end functionality [101]–[104]. These types of multilayers are typically very stable and employed as tunable dielectrics.

Physisorbed multilayer formation is usually an inadvertent process, and entails the loose physisorption of ligand molecules on top of an already formed SAMs via weak interatomic forces. Physisorbed multilayers are unstable and can typically be removed easily by rigorous rinsing or mechanical means. The formation of physisorbed multilayers has been extensively observed in phosphonic acid SAMs, as already discussed in paragraph 2.7.1.

In this thesis, as will be presented in Chapters 4 and 5, multilayer formation was observed for mercaptosuccinic acid (MSA) and trimethylaminethiol (TMA) SAMs, as well as octadecylphosphonic acid (ODPA) SAMs at long monolayer formation time.

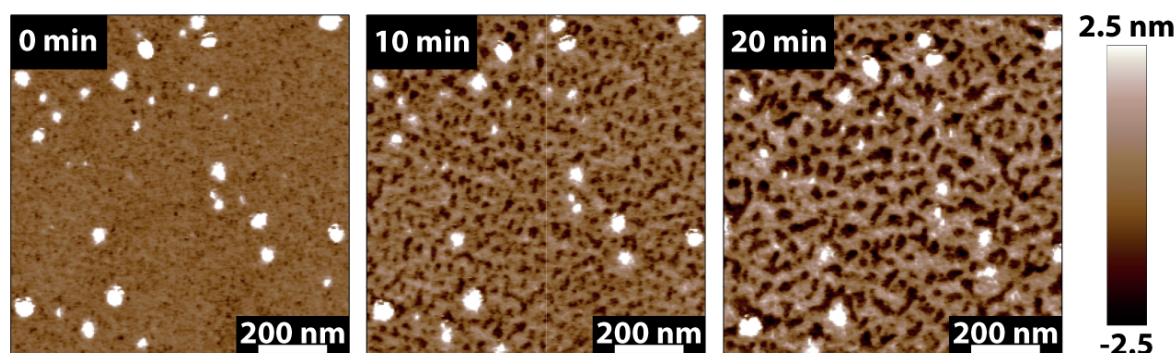


Figure 2.10: Displacement of octadecylphosphonic acid (ODPA) multilayer by an AFM tip. Scanning was performed using a work to free amplitude ratio equal to 0.75, exerting an average force of 10 nN on the sample. The clear displacement of the physisorbed material by low loads highlights the low mechanical stability of the multilayer film. Inset indicates scanning time.

2.7.3 The role of bimodal AFM

At different monolayer formation times the ligands adopt a different configuration: from loosely physisorbed states, to lying down, disorganized islands, to increasing order and packing density and finally to multilayer formation. Characteristic properties of SAMs, such as elasticity and wetting, are expected to vary alongside the different formation states. The different steps of monolayer formation have been recorded for thiol SAMs,

but in the case of alkylphosphonic acids observation of the temporal evolution of SAMs and resulting properties is lacking. Bimodal AFM can be used to measure the temporal evolution of the elasticity of alkylphosphonic acid SAMs and its direct correlation to the recorded topography. The results can provide information on the evolution of ligand density and packing with increasing monolayer formation time, t_M , and allow the visualization of different steps in monolayer and multilayer formation.

2.8. References

- [1] A. Ulman, *An introduction to ultrathin organic films: From Langmuir-Blodgett to self-assembly*, 1st ed. Boston: Academic Press, 1991.
- [2] J. Gao, F. Li, and Q. Guo, "Balance of forces in self-assembled monolayers," *J. Phys. Chem. C*, vol. 117, no. 47, pp. 24985–24990, 2013.
- [3] F. W. Delrio, C. Jaye, D. A. Fischer, and R. F. Cook, "Elastic and adhesive properties of alkanethiol self-assembled monolayers on gold," *Appl. Phys. Lett.*, vol. 94, no. 13, pp. 10–13, 2009.
- [4] N. J. Brewer, B. D. Beake, and G. J. Leggett, "Friction force microscopy of self-assembled monolayers: Influence of adsorbate alkyl chain length, terminal group chemistry, and scan velocity," *Langmuir*, vol. 17, no. 6, pp. 1970–1974, 2001.
- [5] G. E. Poirier and E. D. Pylant, "The self-assembly mechanism of alkanethiols on Au(111)," *Science (80-.)*, vol. 272, no. 5265, pp. 1145–1148, 1996.
- [6] O. Voznyy and J. J. Dubowski, "c (4 x 2) structures of alkanethiol monolayers on Au (111) compatible with the constraint of sense packing," *Langmuir*, vol. 25, no. 111, pp. 7353–7358, 2009.
- [7] C. Vericat, M. E. Vela, G. Corthey, E. Pensa, E. Cortés, M. H. Fonticelli, F. Ibañez, G. E. Benitez, P. Carro, R. C. Salvarezza, E. Cortes, M. H. Fonticelli, F. Ibanez, G. E. Benitez, P. Carro, and R. C. Salvarezza, "Self-assembled monolayers of thiolates on metals: a review article on sulfur-metal chemistry and surface structures," *RSC Adv.*, vol. 4, no. 53, pp. 27730–27754, 2014.
- [8] M. Nakaya, M. Shikishima, M. Shibuta, N. Hirata, and T. Eguchi, "Molecular-scale and wide-energy-range tunneling spectroscopy on self-assembled monolayers of alkanethiol molecules," *ACS Nano*, vol. 6, no. 10, pp. 8728–8734, 2012.
- [9] N.-S. S. Lee, D. Kim, H. Kang, D. K. Park, S. W. Han, and J. Noh, "Structural transitions of octanethiol self-assembled monolayers on gold nanoplates after mild thermal annealing," *J. Phys. Chem. C*, vol. 115, no. 13, pp. 5868–5874, 2011.
- [10] V. B. Engelkes and C. Daniel Frisbie, "Simultaneous nanoindentation and electron tunneling through alkanethiol self-assembled monolayers," *J. Phys. Chem. B*, vol. 110, no. 20, pp. 10011–10020, 2006.
- [11] W. J. Price, S. A. Leigh, S. M. Hsu, T. E. Patten, and G. Y. Liu, "Measuring the size dependence of young's modulus using force modulation atomic force microscopy," *J. Phys. Chem. A*, vol. 110, no. 4, pp. 1382–1388, 2006.
- [12] W. Kiridena, V. Jain, P. K. Kuo, and G. Liu, "Nanometer-scale elasticity

- measurements on organic monolayers using scanning force microscopy," *Surf. Interface Anal.*, vol. 25, no. 6, pp. 383–389, 1997.
- [13] J. E. Houston and H. I. Kim, "Adhesion, friction, and mechanical properties of functionalized alkanethiol self-assembled monolayers," *Acc. Chem. Res.*, vol. 35, no. 7, pp. 547–553, 2002.
- [14] R. Henda, M. Grunze, and A. J. Pertsin, "Static energy calculations of stress-strain behavior of self-assembled monolayers," *Tribol. Lett.*, vol. 5, pp. 191–195, 1998.
- [15] D. M. Spori, N. V Venkataraman, S. G. P. Tosatti, F. Durmaz, N. D. Spencer, and S. Zürcher, "Influence of alkyl chain length on phosphate self-assembled monolayers," *Langmuir*, vol. 23, no. 15, pp. 8053–60, 2007.
- [16] K. Fukuda, T. Hamamoto, T. Yokota, T. Sekitani, U. Zschieschang, H. Klauk, and T. Someya, "Effects of the alkyl chain length in phosphonic acid self-assembled monolayer gate dielectrics on the performance and stability of low-voltage organic thin-film transistors," *Appl. Phys. Lett.*, vol. 95, no. 20, p. 203301, 2009.
- [17] M. D. Losego, J. T. Guske, A. Efremenko, J.-P. Maria, and S. Franzen, "Characterizing the molecular order of phosphonic acid self-assembled monolayers on indium tin oxide surfaces," *Langmuir*, vol. 27, no. 19, pp. 11883–8, 2011.
- [18] R. Luschtinetz, A. F. Oliveira, H. A. Duarte, and G. Seifert, "Self-assembled monolayers of alkylphosphonic acids on aluminum oxide surfaces - A theoretical study," *Zeitschrift für Anorg. und Allg. Chemie*, vol. 636, no. 8, pp. 1506–1512, 2010.
- [19] A. Khassanov, H. G. Steinrück, T. Schmaltz, A. Magerl, and M. Halik, "Structural investigations of self-assembled monolayers for organic electronics: Results from X-ray reflectivity," *Acc. Chem. Res.*, vol. 48, no. 7, pp. 1901–1908, 2015.
- [20] I. Doudevski, W. a Hayes, J. T. Woodward, and D. K. Schwartz, "Atomic force microscope imaging of molecular aggregation during self-assembled monolayer growth," *Colloids Surfaces A Physicochem. Eng. Asp.*, vol. 174, no. 1–2, pp. 233–243, 2000.
- [21] W. Vogel, B. Rosner, and B. Tesche, "Structural investigations of octadecylphosphonic acid multilayers," *J. Phys. Chem.*, vol. 97, no. 1, pp. 11611–11616, 1993.
- [22] I. Gouzman, M. Dubey, M. D. Carolus, J. Schwartz, and S. L. Bernasek, "Monolayer vs. multilayer self-assembled alkylphosphonate films: X-ray photoelectron spectroscopy studies," *Surf. Sci.*, vol. 600, no. 4, pp. 773–781, 2006.
- [23] G. Guerrero, J. G. Alauzun, M. Granier, D. Laurencin, and P. H. Mutin, "Phosphonate

- coupling molecules for the control of surface/interface properties and the synthesis of nanomaterials.," *Dalton Trans.*, vol. 42, no. 35, pp. 12569–85, 2013.
- [24] T. Hauffman, O. Blajiev, J. Snauwaert, C. van Haesendonck, A. Hubin, and H. Terryn, "Study of the self-assembling of n-octylphosphonic acid layers on aluminum oxide.," *Langmuir*, vol. 24, no. 23, pp. 13450–6, 2008.
- [25] A. G. Koutsoubas, N. Spiliopoulos, D. L. Anastassopoulos, A. A. Vradis, and G. D. Priftis, "Formation of alkane-phosphonic acid self-assembled monolayers on alumina: An in situ SPR study," *Surf. Interface Anal.*, vol. 41, no. 11, pp. 897–903, 2009.
- [26] R. Hofer, M. Textor, and N. D. Spencer, "Alkyl phosphate monolayers, self-assembled from aqueous solution onto metal oxide surfaces," *Langmuir*, vol. 17, no. 13, pp. 4014–4020, 2001.
- [27] P. Thissen, M. Valtiner, and G. Grundmeier, "Stability of phosphonic acid self-assembled monolayers on amorphous and single-crystalline aluminum oxide surfaces in aqueous solution," *Langmuir*, vol. 26, no. 1, pp. 156–64, Jan. 2010.
- [28] S. Lassiaz, A. Galarneau, P. Trens, D. Labarre, H. Mutin, and D. Brunel, "Organo-lined alumina surface from covalent attachment of alkylphosphonate chains in aqueous solution," *New J. Chem.*, vol. 34, no. 7, p. 1424, 2010.
- [29] S. P. Pujari, L. Scheres, A. T. M. Marcelis, and H. Zuilhof, "Covalent surface modification of oxide surfaces.," *Angew. Chem. Int. Ed. Engl.*, vol. 53, no. 25, pp. 6322–56, 2014.
- [30] A. Vioux, J. Le, B. P. Hubert, and M. Dominique, "Hybrid Organic-Inorganic Materials Based on Organophosphorus Derivatives," *Top Curr Chem*, no. 232, pp. 145–174, 2004.
- [31] I. L. Liakos, R. C. Newman, E. McAlpine, and M. R. Alexander, "Study of the resistance of SAMs on aluminium to acidic and basic solutions using dynamic contact angle measurement.," *Langmuir*, vol. 23, no. 12, pp. 995–999, 2007.
- [32] T. T. Foster, M. R. Alexander, G. J. Leggett, and E. McAlpine, "Friction force microscopy of alkylphosphonic acid and carboxylic acids adsorbed on the native oxide of aluminum," *Langmuir*, vol. 22, no. 22, pp. 9254–9259, 2006.
- [33] T. Hauffman, A. Hubin, and H. Terryn, "Study of the self-assembling of n-octylphosphonic acid layers on aluminum oxide from ethanolic solutions," *Surf. Interface Anal.*, vol. 45, no. 10, pp. 1435–1440, 2013.
- [34] B. Branch, M. Dubey, A. S. Anderson, K. Artyushkova, J. K. Baldwin, D. Petsev, and

- A. M. Dattelbaum, "Investigating phosphonate monolayer stability on ALD oxide surfaces," *Appl. Surf. Sci.*, vol. 288, pp. 98–108, Jan. 2014.
- [35] M. S. Lim, K. J. Smiley, and E. S. Gawalt, "Thermally driven stability of octadecylphosphonic acid thin films grown on SS316L," *Scanning*, vol. 32, no. 5, pp. 304–311, 2010.
- [36] G. a. DeVries, F. R. Talley, R. P. Carney, and F. Stellacci, "Thermodynamic study of the reactivity of the two topological point defects present in mixed self-assembled monolayers on gold nanoparticles," *Adv. Mater.*, vol. 20, no. 22, pp. 4243–4247, Nov. 2008.
- [37] R. P. Carney, G. A. DeVries, C. Dubois, H. Kim, J. Y. Kim, C. Singh, P. K. Ghorai, J. B. Tracy, R. L. Stiles, R. W. Murray, S. C. Glotzer, and F. Stellacci, "Size Limitations for the Formation of Ordered Striped Nanoparticles," *J. Am. Chem. SOC*, vol. 130, no. 3, pp. 798–799, 2007.
- [38] J. P. Folkers, P. E. Laibinis, G. M. Whitesides, and J. Deutch, "Phase behavior of two-component self-assembled monolayers of alkanethiolates on gold," *J. Phys. Chem.*, vol. 98, pp. 563–571, 1994.
- [39] L. A. Bumm, J. J. Arnold, L. F. Charles, T. D. Dunbar, D. L. Allara, and P. S. Weiss, "Directed self-assembly to create molecular terraces with molecularly sharp boundaries in organic monolayers," *J. Am. Chem. Soc.*, vol. 121, no. 35, pp. 8017–8021, 1999.
- [40] R. Smith and S. Reed, "Phase separation within a binary self-assembled monolayer on Au {111} driven by an amide-containing alkanethiol," *J. Phys. Chem.*, vol. 105, no. 6, pp. 1119–1122, 2001.
- [41] A. Ulman, "Formation and Structure of Self-Assembled Monolayers," *Chem. Rev.*, vol. 96, no. 4, pp. 1533–1554, 1996.
- [42] R. G. Nuzzo and D. L. Allara, "Adsorption of bifunctional organic disulfides on gold surfaces," *J. Am. Chem. SOC*, vol. 105, no. 13, pp. 4481–4483, 1983.
- [43] G. M. Whitesides, J. K. Kriebel, and J. C. Love, "Molecular engineering of surfaces using self-assembled monolayers," *Sci. progress*, vol. 88, no. 1, pp. 17–48, 2005.
- [44] T. Bürgi, "Properties of the gold–sulphur interface: from self-assembled monolayers to clusters," *Nanoscale*, vol. 7, no. 38, pp. 15553–15567, 2015.
- [45] P. Fenter, P. Eisenberger, and K. S. Liang, "Chain-length dependence of the structures and phases of CH₃(CH₂)_{n-1} SH self-assembled on Au(111)," *Phys. Rev. Lett.*, vol. 70, no. 16, pp. 2447–2450, 1993.

- [46] C. A. Alves, E. L. Smith, and M. D. Porter, "Atomic scale imaging of alkanethiolate monolayers at gold surfaces with atomic force microscopy," *J. Am. Chem. SOC*, vol. 114, no. 2, pp. 1222–1227, 1992.
- [47] E. Delamarche, B. Michel, H. A. Biebuyck, and C. Gerber, "Golden interfaces: The surface of self-assembled monolayers," *Adv. Mater.*, vol. 8, no. 9, pp. 719–729, 1996.
- [48] G. Liu and M. B. Salmeron, "Reversible displacement of chemisorbed n-alkanethiol molecules on Au(111) surface: An atomic force microscopy study," *Langmuir*, vol. 10, no. 12, pp. 367–370, 1994.
- [49] G. E. Poirier. and M. J. Tarlov, "Superlattice of n-alkanethiol monolayers self-assembled on Au(111)," *Langmuir*, vol. 10, no. 9, pp. 2853–2856, 1994.
- [50] M. S. Yeganeh, S. M. Dougal, R. S. Polizzotti, and P. Rabinowitz, "Interfacial atomic structure of a self-assembled alkyl thiol monolayer/Au(111): A sum-frequency generation study," *Phys. Rev. Lett.*, vol. 74, no. 10, pp. 1811–1814, 1995.
- [51] A. J. Pertsin and M. Grunze, "Monte Carlo studies of self-assembled monolayers using simple generalized models . II . A two-site molecular model," *J. Chem. Phys.*, vol. 106, no. 17, pp. 7343–7351, 1997.
- [52] R. Bhatia and B. J. Garrison, "Phase transitions in a methyl-terminated monolayer self-assembled on Au { 111 }," *Langmuir*, vol. 13, no. 4, pp. 765–769, 1997.
- [53] K. M. Beardmore, J. D. Kress, A. R. Bishop, and L. Alamos, "Ab-initio calculations of the gold-sulfur interaction for alkanethiol monolayers," *Synth. Met.*, vol. 84, pp. 317–318, 1997.
- [54] R. Bhatia and B. J. Garrison, "Structure of c (4 × 2) superlattice in alkanethiolate self-assembled monolayers," *Langmuir*, vol. 13, no. 15, pp. 4038–4043, 1997.
- [55] A. J. Pertsin and M. Grunze, "Low-energy structures of a monolayer of octadecanethiol," *Langmuir*, vol. 10, no. 10, pp. 3668–3674, 1994.
- [56] P. Fenter, F. Schreiber, L. Berman, G. Scoles, P. Eisenberger, and M. J. Bedzyk, "On the structure and evolution of the buried S / Au interface in self-assembled monolayers : X-ray standing wave results," *Surf. Sci.*, vol. 413, pp. 213–235, 1998.
- [57] A. Cossaro, R. Mazzarello, R. Rousseau, L. Casalis, A. Verdini, A. Kohlmeyer, L. Floreano, S. Scandolo, A. Morgante, and G. Scoles, "X-ray diffraction and computation yield the Structure of alkanethiols on Gold(111)," *Science (80-.)*, vol. 321, no. 5891, pp. 943–946, 2008.
- [58] N. A. Kautz and S. A. Kandel, "Alkanethiol monolayers contain gold adatoms, and

- adatom coverage is independent of chain length," *J. Phys. Chem. C*, vol. 113, no. 111, pp. 19286–19291, 2009.
- [59] P. Maksymovych, D. C. Sorescu, and J. T. Yates, "Gold-adatom-mediated bonding in self-assembled short-chain alkanethiolate species on the Au (111) surface," *Phys. Rev. Lett.*, vol. 97, no. 146103, pp. 1–4, 2006.
- [60] H. Grönbeck and H. Häkkinen, "Polymerization at the alkylthiolate - Au (111) interface," *J. Phys. Chem. B Lett.*, vol. 111, no. 13, pp. 3325–3327, 2007.
- [61] R. Mazzarello, A. Cossaro, A. Verdini, R. Rousseau, L. Casalis, M. F. Danisman, L. Floreano, S. Scandolo, A. Morgante, and G. Scoles, "Structure of a CH₃S monolayer on Au (111) solved by the interplay between molecular dynamics calculations and diffraction measurements," *Phys. Rev. Lett.*, vol. 98, no. 1, pp. 161021–161024, 2007.
- [62] D. Jiang, "Au adatom-linked CH₃S – Au – SCH₃ complexes on Au (1 1 1)," *Chem. Phys. Lett.*, vol. 477, no. 1–3, pp. 90–94, 2009.
- [63] A. Nagoya and Y. Morikawa, "Adsorption states of methylthiolate on the Au (111) surface," *J. Phys. Condens. Matter*, vol. 19, no. 36, pp. 5245–5252, 2007.
- [64] "Primary Aluminium Production." [Online]. Available: <http://www.world-aluminium.org/statistics/#data>. [Accessed: 28-Jul-2017].
- [65] Z. Łodziana, J. K. Nørskov, and P. Stoltze, "The stability of the hydroxylated (0001) surface of α -Al₂O₃," *J. Chem. Phys.*, vol. 118, no. 24, pp. 11179–11188, 2003.
- [66] X.-G. Wang, A. Chaka, and M. Scheffler, "Effect of the environment on α -Al₂O₃ (0001) surface structures," *Phys. Rev. Lett.*, vol. 84, no. 16, pp. 3650–3653, 2000.
- [67] C. L. Perkins, "Molecular anchors for self-assembled monolayers on ZnO: A direct comparison of the thiol and phosphonic acid moieties," *J. Phys. Chem. C*, vol. 113, no. 111, pp. 18276–18286, 2009.
- [68] F. Schreiber, "Structure and growth of self-assembling monolayers," *Prog. Surf. Sci.*, vol. 65, no. 5–8, pp. 151–257, 2000.
- [69] C. E. Taylor and D. K. Schwartz, "Octadecanoic acid self-assembled monolayer growth at sapphire surfaces," *Langmuir*, vol. 19, no. 12, pp. 2665–2672, 2003.
- [70] S. Pawsey, K. Yach, J. Halla, and L. Reven, "Self-assembled monolayers of alkanolic acids: A solid-state NMR study," *Langmuir*, vol. 16, no. 7, pp. 3294–3303, 2000.
- [71] R. Luschtinetz, A. F. Oliveira, J. Frenzel, J. O. Joswig, G. Seifert, and H. A. Duarte, "Adsorption of phosphonic and ethylphosphonic acid on aluminum oxide surfaces," *Surf. Sci.*, vol. 602, no. 7, pp. 1347–1359, 2008.

- [72] T. Bauer, T. Schmaltz, T. Lenz, M. Halik, B. Meyer, and T. Clark, "Phosphonate- and carboxylate-based self-assembled monolayers for organic devices: a theoretical study of surface binding on aluminum oxide with experimental support," *ACS Appl. Mater. Interfaces*, vol. 5, no. 13, pp. 6073–80, 2013.
- [73] L. G. Hector, S. M. Opalka, G. A. Nitowski, L. Wieserman, D. J. Siegel, H. Yu, and J. B. Adams, "Investigation of vinyl phosphonic acid/hydroxylated α -Al₂O₃(0001) reaction enthalpies," *Surf. Sci.*, vol. 494, no. 1, pp. 1–20, 2001.
- [74] C. Queffelec, M. Petit, P. Janvier, D. A. Knight, and B. Bujoli, "Surface modification using phosphonic acids and esters," *Chem. Rev.*, vol. 112, no. 7, pp. 3777–3807, 2012.
- [75] L. G. Hector, G. A. Nitowski, S. M. Opalka, and L. Wieserman, "Investigation of vinyl phosphonic acid/hydroxylated α -Al₂O₃ (0001) reaction enthalpies," *Surf. Sci.*, vol. 494, no. 1, pp. 1–20, 2001.
- [76] A. Phan, D. R. Cole, and A. Striolo, "Liquid ethanol simulated on crystalline alpha alumina," *J. Phys. Chem. B*, vol. 117, no. 14, pp. 3829–3840, 2013.
- [77] S. K. Parida, S. Dash, S. Patel, and B. K. Mishra, "Adsorption of organic molecules on silica surface," *Adv. Colloid Interface Sci.*, vol. 121, no. 1–3, pp. 77–110, 2006.
- [78] X. Chen, E. Luais, N. Darwish, S. Ciampi, P. Thordarson, and J. J. Gooding, "Studies on the effect of solvents on self-assembled monolayers formed from organophosphonic acids on indium tin oxide.," *Langmuir*, vol. 28, no. 25, pp. 9487–95, 2012.
- [79] H.-Y. Nie, N. S. McIntyre, W. M. Lau, and J. M. Feng, "Optical properties of an octadecylphosphonic acid self-assembled monolayer on a silicon wafer," *Thin Solid Films*, vol. 517, no. 2, pp. 814–818, 2008.
- [80] E. L. Hanson, J. Schwartz, B. Nickel, N. Koch, and M. F. Danisman, "Bonding self-assembled, compact organophosphonate monolayers to the native oxide surface of silicon," *J. Am. Chem. Soc.*, vol. 125, no. 51, pp. 16074–16080, 2003.
- [81] P. Thissen, A. Vega, T. Peixoto, and Y. J. Chabal, "Controlled, low-coverage metal oxide activation of silicon for organic functionalization: unraveling the phosphonate bond.," *Langmuir*, vol. 28, no. 50, pp. 17494–505, 2012.
- [82] C. Vericat, M. E. Vela, G. Benitez, P. Carro, and R. C. Salvarezza, "Self-assembled monolayers of thiols and dithiols on gold: new challenges for a well-known system.," *Chem. Soc. Rev.*, vol. 39, no. 5, pp. 1805–1834, 2010.
- [83] E. Pensa, A. A. Rubert, G. Benitez, P. Carro, R. C. Salvarezza, and C. Vericat, "Are 4 -

- Mercaptobenzoic Acid Self Assembled Monolayers on Au(111) a Suitable System to Test Adatom Models?," *J. Phys. Chem. C*, vol. 116, no. 49, pp. 25765–25771, 2012.
- [84] E. Pensa, P. Carro, A. A. Rubert, G. Benitez, C. Vericat, R. C. Salvarezza, D. De Qui, U. D. La Laguna, and A. Astrofi, "Thiol with an unusual adsorption - desorption behavior: 6-mercaptopurine on Au (111)," *Langmuir*, vol. 26, no. 22, pp. 17068–17074, 2010.
- [85] J. C. Azcárate, M. A. F. Addato, A. Rubert, G. Corthey, G. S. K. Moreno, G. Benítez, E. Zelaya, R. C. Salvarezza, and M. H. Fonticelli, "Surface chemistry of thiomalic acid adsorption on planar gold and gold nanoparticles," *Langmuir*, vol. 30, no. 7, pp. 1820–1826, 2014.
- [86] C. M. Jäger, T. Schmaltz, M. Novak, A. Khassanov, A. Vorobiev, M. Hennemann, A. Krause, H. Dietrich, D. Zahn, A. Hirsch, M. Halik, and T. Clark, "Improving the charge transport in self-assembled monolayer field-effect transistors: From theory to devices," *J. Am. Chem. Soc.*, vol. 135, no. 12, pp. 4893–4900, 2013.
- [87] C. Singh, P. K. Ghorai, M. A. Horsch, A. M. Jackson, R. G. Larson, F. Stellacci, and S. C. Glotzer, "Entropy-mediated patterning of surfactant-coated nanoparticles and surfaces," *Phys. Rev. Lett.*, vol. 99, no. 22, pp. 1–4, 2007.
- [88] C. Singh, A. M. Jackson, F. Stellacci, and S. C. Glotzer, "Exploiting substrate stress to modify nanoscale SAM patterns," *J. Am. Chem. Soc.*, vol. 131, no. 45, pp. 16377–16379, 2009.
- [89] M. Himmelhaus, F. Eisert, M. Buck, and M. Grunze, "Self-assembly of n-alkanethiol monolayers. A study by IR-visible sum frequency spectroscopy (SFG)," *J. Phys. Chem. B*, vol. 104, no. 3, pp. 576–584, 2000.
- [90] C. Humbert, M. Buck, A. Calderone, J. P. Vigneron, V. Meunier, B. Champagne, W. Q. Zheng, A. Tadjeddine, P. A. Thiry, and A. Peremans, "In situ monitoring of the self-assembly of p-nitroanilino terminated thiol on gold: A study by IR-vis sum-frequency generation spectroscopy," *Phys. Status Solidi Appl. Res.*, vol. 175, no. 1, pp. 129–136, 1999.
- [91] R. Yamada and K. Uosaki, "In situ, real time monitoring of the self-assembly process of decanethiol on Au (111) in liquid phase. A scanning tunneling microscopy investigation," *Langmuir*, vol. 13, no. 20, pp. 5218–5221, 1997.
- [92] R. Yamada and K. Uosaki, "In situ scanning tunneling microscopy observation of the self-assembly process of alkanethiols on gold(111) in solution," *Langmuir*, vol.

- 14, no. 4, pp. 855–861, 1998.
- [93] M. Godin, P. J. Williams, V. Tabard-Cossa, O. Laroche, L. Y. Beaulieu, R. B. Lennox, and P. Grütter, "Surface stress, kinetics, and structure of alkanethiol self-assembled monolayers.," *Langmuir*, vol. 20, no. 17, pp. 7090–7096, 2004.
- [94] D. G. Matei, H. Muzik, and A. Turchanin, "Structural investigation of 1,1' biphenyl-4-thiol self-assembled monolayers on Au(111) by scanning tunneling microscopy and low-energy electron diffraction," *Langmuir*, vol. 28, no. 9, pp. 13905–13911, 2012.
- [95] G. E. Poirier, W. P. Fitts, and J. M. White, "Two-dimensional phase diagram of decanethiol on Au (111)," *Langmuir*, vol. 17, no. 4, pp. 1176–1183, 2001.
- [96] K. Sotthewes, H. Wu, A. Kumar, G. J. Vancso, P. M. Scho, and H. J. W. Zandvliet, "Molecular dynamics and energy landscape of decanethiolates in self-assembled monolayers on Au(111) studied by scanning tunneling microscopy," *Langmuir*, vol. 29, no. 11, pp. 3662–3667, 2013.
- [97] P. E. Laibinis, G. M. Whitesides, and D. L. Allara, "Comparison of the structures and wetting properties of self-assembled monolayers of n-alkanethiols on the coinage metal surfaces, Cu, Ag, Au," *J. Am. Chem. SOC*, vol. 113, no. 19, pp. 7152–7167, 1991.
- [98] R. G. Nuzzo, B. R. Zegarski, and L. H. Dubois, "Fundamental studies of the chemisorption of organosulfur compounds on Au(111). Implications for molecular self-assembly on gold surfaces," *J. Am. Chem. Soc.*, vol. 109, no. 3, pp. 733–740, 1987.
- [99] X. Torrelles, E. Barrena, C. Munuera, J. Rius, S. Ferrer, and C. Ocal, "New insights in the c(4×2) reconstruction of hexadecanethiol on Au(111) revealed by grazing incidence X-ray diffraction," *Langmuir*, vol. 20, no. 21, pp. 9396–9402, 2004.
- [100] T. Hauffman, L. Van Lokeren, R. Willem, A. Hubin, and H. Terryn, "In situ study of the deposition of (ultra)thin organic phosphonic acid layers on the oxide of aluminum.," *Langmuir*, vol. 28, no. 6, pp. 3167–73, 2012.
- [101] L. Kim, T.; Crooks, R.M.; Tsen, M.; Sun, "Polymeric self-assembled monolayers. 2. Synthesis and characterization of self-assembled polydiacetylene mono- and multilayers," *J. Am. Chem. Soc.*, vol. 117, pp. 3963–3967, 1995.
- [102] J. M. Tour, J. M. Tour, L. R. Jones, D. L. Pearson, J. J. S. Lamba, T. P. Burgin, G. M. Whitesides, D. L. Allara, A. N. Parikh, and S. V. Atre, "Self-assembled monolayers and multilayers of conjugated thiols, α,ω -dithiols, and thioacetyl-containing

- adsorbates. Understanding attachments between potential molecular wires and gold surfaces," *J. Am. Chem. Soc.*, vol. 117, no. 37, pp. 9529–9534, 1995.
- [103] S. A. DiBenedetto, A. Facchetti, M. A. Ratner, and T. J. Marks, "Molecular self-assembled monolayers and multilayers for organic and unconventional inorganic thin-film transistor applications," *Adv. Mater.*, vol. 21, no. 14–15, pp. 1407–1433, 2009.
- [104] D. Käfer, G. Witte, P. Cyganik, A. Terfort, and C. Wöll, "A comprehensive study of self-assembled monolayers of anthracenethiol on gold: solvent effects, structure, and stability," *J. Am. Chem. Soc.*, vol. 128, no. 5, pp. 1723–32, 2006.

Chapter 3

Bimodal Atomic Force Microscopy for the nanomechanical characterization of organic self-assembled monolayers

As discussed in Chapters 1 and 2, the use of bimodal Atomic Force Microscopy is proposed for the nanomechanical characterization of organic SAMs. In this chapter the basis of dynamic AFM will be briefly discussed in paragraphs 3.1 and 3.2. The way interaction forces between the tip and sample affect the cantilever motion, and how this effect can be detected and quantified will be discussed in paragraph 3.3. In the context of this thesis contact mechanics forces dominate the response of the cantilever, and their modeling will be discussed in paragraph 3.4. Multifrequency AFM, utilizing the nonlinearities of the tip-sample forces to enhance resolution and access information on material properties will be presented in paragraph 3.5. The theory of bimodal AFM and its use for the nanomechanical characterization of organic SAMs will be presented in subparagraph 3.5.5. The derivation of all mathematical expressions for the single mode excitation has been done following the work of Garcia in reference [3]. For bimodal excitation, the model used correlating experimental observables to material properties is presented as derived by Amo et al. in reference [36] and Labuda et al. in reference [45].

3.1. The working principle of the AFM

Atomic Force Microscopy is a technique widely applied for the detailed characterization of surface structures and surface properties. Belonging to the family of Scanning Probe Microscopy, the heart of an AFM is a cantilever with a microfabricated tip, which is scanned over a surface in a raster-like pattern. A laser beam is reflected off the back of the cantilever and the signal is detected by a quartered photodiode. Distortions of the cantilever during its motion result in a deflection of the beam at a position other than the center of the photodiode, allowing for tracking of the cantilever motion and subsequent reconstruction of the surface topography. A controller regulates, collects, and processes the data, and drives the piezoactuator, or piezo for short, scanner. The controller consists of a variable number of A/D converters that receive data from the detection system of cantilever deflections, some D/A converters that give signals to the piezo, and an interface with a computer that stores data [1].

An AFM can be operated in different modes, depending on the application. The cantilever can be held static at the base, in which case the microscope is operated in static mode, or it can be vibrated at the base, usually in a sinusoidal way, in which case the microscope is operated in dynamic mode.

Dynamic modes of operation are in general advantageous for most applications, as they typically allow for extremely high resolution while maintaining a gentle interaction between the tip and the sample. Moreover, the tip motion carries information related to specific tip-sample interactions and there are several observables sensitive to those (amplitude (A), frequency (f) or angular frequency ($\omega = 2\pi f$), phase shift ($\Delta\varphi$), deflection), which can be used to quantitatively characterize materials' properties at the nanoscale [2].

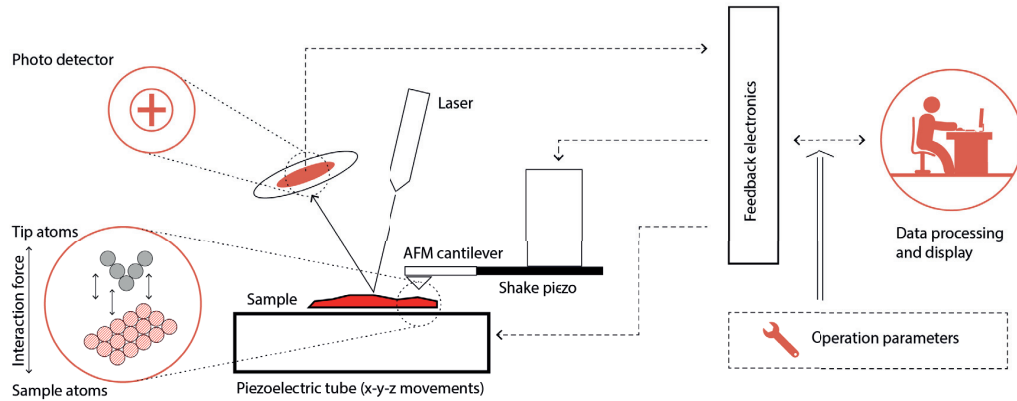


Figure 3.1: Schematic representation of the working principle of an AFM. A cantilever is scanned over a sample in a raster pattern. The cantilever can be held static or oscillated by the shake piezo. The motion of the cantilever is tracked by the reflection of a laser beam off the back of the cantilever and to a photodetector (quartered photodiode). Deviations of the laser reflection from the zero position, caused by interactions of the tip with the sample, are the feedback signal sent to the control electronics of the system, which monitor and control the motion of the cantilever.

At present, two dynamic AFM modes are used: amplitude modulation, AM-AFM, and frequency modulation, FM-AFM. In most cases, where the measurement is performed in air or liquid, the dynamic AFM is operated in AM-AFM mode. FM-AFM mode is in general preferred when a higher Q factor can be achieved, such as operation in vacuum or operation of a higher eigenmode. In the present work the fundamental frequency was always driven in the AM mode, while the higher eigenmodes were driven in FM. An in-depth analysis of the two techniques can be provided in reference [3] and chapter 17 of reference [4] respectively.

3.2. Equation of motion for an oscillating cantilever: The Euler-Bernoulli beam and the equivalent point-mass model

The purpose during an AFM measurement is to correlate the observables, in the case of AM-AFM amplitude and phase shift, to tip-sample forces. To do so, it is necessary to construct a model that describes this relationship.

An AFM cantilever can be modeled as a continuous beam using a modified Euler-Bernoulli equation, as shown by equation 3.1 [3].

$$\begin{aligned}
EI \frac{\partial^4}{\partial^4 x} \left[w(x, t) + a_1 \frac{\partial w}{\partial t} \right] + \rho W h \frac{\partial^2 w(x, t)}{\partial t^2} \\
= -a_0 \frac{\partial w}{\partial t} + \delta(x - L) [F_{exc}(x, t) + F_{ts}(d)]
\end{aligned} \tag{3.1}$$

Where E , I and ρ the Young modulus, linear moment of inertia and linear mass density of the cantilever, W , h and L the width, height and length of the cantilever, $w(x, t)$ the perpendicular from the x axis displacement of the cantilever as a function of distance from one end, x , and time, t . a_0 and a_1 refer to external and internal damping of the cantilever respectively. $F_{exc}(x, t)$ is the excitation force applied to the cantilever, depending on both distance and time, $F_{ts}(d)$ the sum of all tip-surface forces, depending on the instantaneous displacement of the tip of the cantilever, $d = z_o + z$. For $d > 0$ the tip and sample are not in mechanical contact and d is referred to as the instantaneous tip-sample separation. For $d \leq 0$ the two bodies are considered in contact and we denote $d = \delta$, indentation. The delta function $\delta(x - L)$ signifies that all forces are applied at the apex of the cantilever.

Given the complexity of the general Euler-Bernoulli equation, in most cases the well-known equivalent point-mass model is used. In order to pass from the continuous model of the beam to an equivalent spring-mass system with discrete solutions, equation 3.1 can be solved by separating the general solution, $w(x, t)$ into a spatial and a temporal component, $X(x)$ and $Y(t)$ respectively, as described by Garcia [3]:

$$w(x, t) = X(x)Y(t) \tag{3.2}$$

By fixing the beam on one end ($X(0)=0$, $X'(0)=0$) and imposing no torque and no internal force at the free end ($X''(L)=0$ and $X'''(L)=0$), equation 3.2 has n discrete solutions, each one corresponding to one of the eigenmodes of the cantilever. The general solution can be expressed as a superposition of the solution for each mode, as shown by equation 3.3.

$$w(x, t) = \sum_{n=1}^{\infty} X_n(x)Y_n(t) \tag{3.3}$$

Following the solution of Garcia, the spatial component of each eigenmode at the fixed end and at $x=L$ is defined as $X_n(0) = 0$ and $X_n(L) = 2(-1)^n$, respectively. The temporal component of the motion follows, for each eigenmode n , is the solution of equation 3.4.

$$m_n \ddot{Y}_n(t) + \frac{m_n \omega_n}{Q_n} \dot{Y}_n(t) + m_n \omega_n^2 Y_n(t) = 2(-1)^n [F_{ts}(d) + F_{exc}(t)] \quad (3.4)$$

For the tip, its motion can be calculated by setting $x = L$ in equation 3.3, and defining $z_n(t)$ as the mode projection at the tip end. The actual tip motion is a superposition of the movement of the cantilever in each eigenmode.

$$w(L, t) = \sum_{n=1}^{\infty} 2(-1)^n Y_n(t) \equiv \sum_{n=1}^{\infty} z_n(t) \quad (3.5)$$

From equations 3.4 and 3.5, the general equation of motion for the tip can be calculated, as shown in equation 3.6.

$$m \ddot{z}_n(t) + \frac{m \omega_n}{Q_n} \dot{z}_n(t) + m \omega_n^2 z_n(t) = F_{ts}(d) + F_{exc}(t) \quad (3.6)$$

Equation 3.6 is known as the general form of the equation of motion of an oscillating tip, or cantilever. When operating an AFM under regular conditions, it is frequently considered that the total motion is dominated only by the first eigenmode. Moreover, the cantilever is excited at one frequency, usually at or close to the first eigenmode. The equivalent point-mass model describing the cantilever in this case is considered a sinusoidally driven harmonic oscillator with damping, as expressed by equation 3.7, where $F_o = QA_o/k$ and φ the angle by which the driving force leads the displacement. This simplification will be revisited in paragraph 3.5.5, where bimodal AFM is introduced.

$$m \ddot{z}(t) + \frac{m \omega_{o,1}}{Q_1} \dot{z}(t) + k_1 z(t) = F_{ts} + F_o \cos(\omega t + \varphi) \quad (3.7)$$

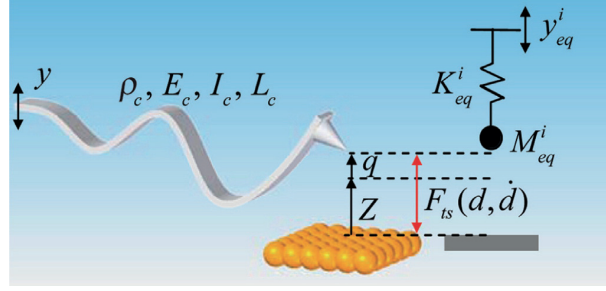


Figure 3.2: Equivalent point-mass representation of a continuous AFM cantilever oscillating in a single eigenmode. The continuous cantilever is characterized by linear mass density, ρ_c , Young's modulus E_c , area moment, I_c , and length, L_c . The point mass model is characterized by equivalent mass, M_{eq} and spring constant, K_{eq} . Reproduced with permission from reference [5].

The steady state solution of equation 3.7 in the underdamped regime, the most relevant in dynamic AFM experiments, and for $F_{ts} = 0$ is given by equation 3.8.

$$z(t) = z_o + A \cos(\omega t + \varphi) \quad (3.8)$$

The experimental observables, amplitude and phase shift, can be expressed as a function of the excitation frequency, ω , as per equations 3.9 and 3.10, respectively.

$$A(\omega) = \frac{F_o/m}{[(\omega_o^2 - \omega^2)^2 + (\omega\omega_o/Q)^2]^{1/2}} \quad (3.9)$$

$$\tan\varphi = \frac{\omega\omega_o/Q}{\omega_o^2 - \omega^2} \quad (3.10)$$

It is noted that damping modifies the resonance frequency of the oscillator. The new resonance frequency, ω_r , is given by equation 3.11.

$$\omega_r = \omega_o \left(1 - \frac{1}{4Q^2}\right)^{1/2} \quad (3.11)$$

For most cantilevers however, when operating in air $Q > 10$ and the approximation $\omega_r = \omega_o$ can be made.

3.3. Tip-sample interaction forces and their effect in cantilever oscillation parameters

In paragraph 3.2 the general equation of motion for the equivalent point mass model of an oscillating cantilever excited at the fundamental eigenmode, in the absence of F_{ts} was given. When $F_{ts} \neq 0$, a shift of the resonance frequency will be caused, experimentally observable through amplitude and phase shifts.

3.3.1. Weakly perturbed harmonic oscillator

A first approximation for the effect of linear forces acting on the oscillating cantilever close to the surface is presented by the model of the weakly perturbed harmonic oscillator:

$$F = F_o + \left(\frac{dF}{dz} \right)_{z_o} (z - z_o) \quad (3.12)$$

The tip-sample interaction is characterized by the gradient of the force in respect to distance, called the tip-sample stiffness, k_{ts} :

$$k_{ts} = - \left(\frac{dF}{dz} \right)_{z_o} \quad (3.13)$$

Substituting the new effective spring constant, $k_{eff} = k - k_{ts}$, into equation (3.7), the motion of the cantilever is given by equation 3.14.

$$m\ddot{z}(t) + \frac{m\omega_{o,1}}{Q_1} \dot{z}(t) + (k - k_{ts})z(t) = F_{ts} + F_o \cos(\omega t + \varphi) \quad (3.14)$$

Conversely, the effective frequency of the cantilever, ω_{eff} , is calculated as:

$$\omega_{eff} = (k_{eff}/m)^{1/2} \quad (3.15)$$

The frequency shift between the effective and the resonance frequency, $\Delta\omega$, under the influence of short-range, linear forces is calculated:

$$\Delta\omega = \omega_{eff} - \omega_o \approx -\frac{\omega_o k_{ts}}{2k} \quad (3.16)$$

As apparent from equation 3.13, the tip-sample stiffness is dependent on the gradient of the tip-sample interatomic forces. Therefore, if properly interpreted, it can be used as an indication for the qualitative and quantitative description of those forces. A change in tip-sample stiffness can be experimentally observed through a frequency shift, as shown by equation 3.16.

In AM - AFM, the frequency of oscillation is kept constant, and any necessary corrections in the movement of the cantilever are applied by the electronics of the system to the amplitude of oscillation, A . In FM - AFM, necessary corrections are applied directly on the frequency.

Equations 3.12 to 3.16 are true only when the interaction forces induce a frequency shift without a simultaneous energy transfer, the force gradient is independent of separation and the tip-sample stiffness is much smaller than the spring constant of the cantilever. These conditions however are not always met in an AFM experiment. In these cases a more general expression relating the tip-sample forces to experimental observables must be used.

3.3.2. The Virial Dissipation method

The Virial Dissipation method, as developed by Garcia and coworkers [6]–[8], relates the amplitude and phase of an oscillating cantilever to the dissipated energy and the virial of the force over one period of oscillation:

$$E_{ts} \equiv -\int_0^T F_{ts}(d)\dot{z}(t)dt = \frac{\pi kA}{Q}(A_o \sin\varphi - A) \quad (3.17)$$

$$V_{ts} = \frac{1}{T} \int_0^T F_{ts}(d)z(t)dt = -\frac{kA_o}{2Q} A \cos\varphi \quad (3.18)$$

Solving the system of equations 3.17 and 3.18 for A and φ , the following equations are obtained:

$$A = A_o \left[(2v)^2 + \left(\frac{1 \pm \sqrt{1 - (4v)^2 - 4\beta/\pi}}{2} \right)^2 \right]^{1/2} \quad (3.19)$$

$$\varphi = -\arctan \left(\frac{1 \pm \sqrt{1 - (4v)^2 - 4\beta/\pi}}{4v} \right) \quad (3.20)$$

Where $v = QV_{ts}/kA_o$ and $\beta = QE_{ts}/kA_o$.

The average tip-sample interaction force can also be calculated as:

$$\langle F_{TS} \rangle \approx \frac{kA_o}{2Q} \left[1 - \left(\frac{A}{A_o} \right)^2 \right]^{1/2} \quad (3.21)$$

The Virial Dissipation method is applicable for both conservative and non-conservative interactions.

3.3.3. Net repulsive, net attractive regime and bistability

Considering the net sum of the tip-sample forces, two distinct regimes can be distinguished: the net attractive and the net repulsive regime. In the net attractive regime attractive forces are dominant. The sum of the tip-sample interaction forces is negative, causing a shift of the resonance frequency to lower values and a phase advance. The tip is not in mechanical contact with the sample. In the repulsive regime repulsive forces are dominant and the net force acting on the oscillating cantilever is positive. The resonance frequency is shifted to higher values and a phase lag is observed. When operating in the net repulsive regime the tip is in intermittent contact with the sample. In the work presented in chapters 4 and 5 of this thesis the cantilever was oscillated in the net repulsive regime.

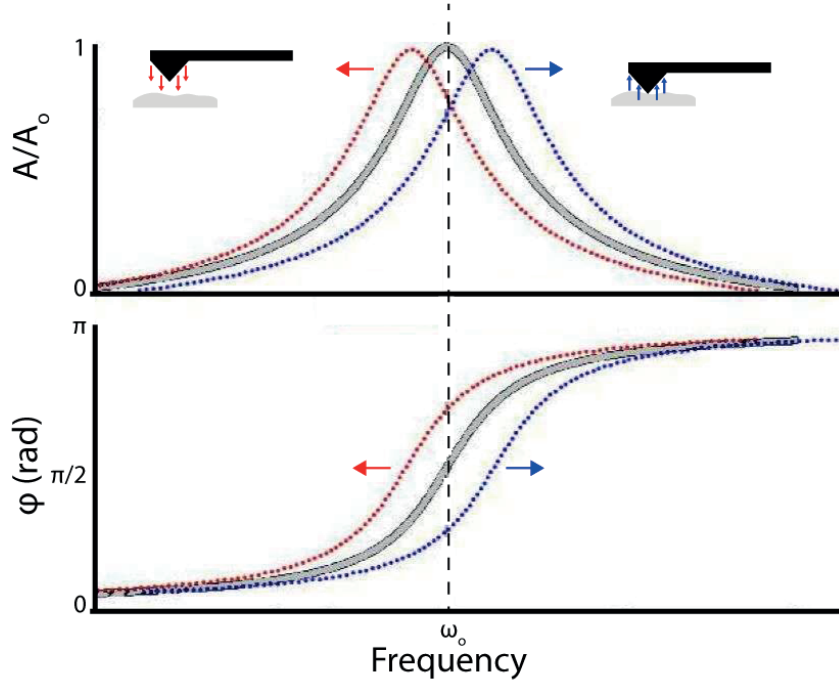


Figure 3.3: Amplitude and phase versus frequency response of a forced damped harmonic oscillator in the absence of tip-sample interaction forces (grey solid line). A small attractive force acting on the cantilever results in a small frequency shift towards lower values, and translates into a phase increase (red dotted line). A small repulsive force results in a small frequency shift towards higher values, which translates into a phase decrease (blue dotted line).

One of the effects of the non-linear nature of the tip-sample interactions is the appearance of non-linear features in the cantilever motion, such as the coexistence of several oscillatory states. This behavior, called bistability, can be perceived while scanning as noise, abrupt and chaotic changes in phase and the appearance of features on the topography that resemble artefacts from a dirty or broken tip.

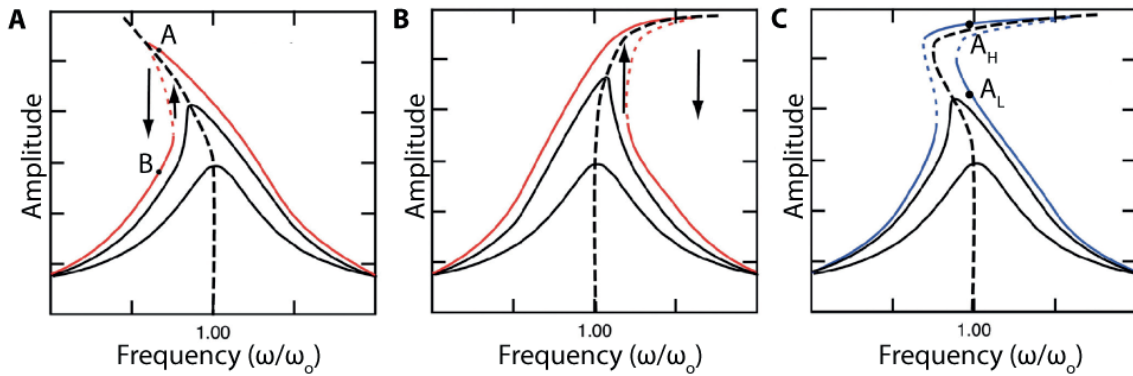


Figure 3.4 (A-C): Schematic illustration of bistability and hysteresis in a one-dimensional non-linear system. (A) Purely attractive interaction. For small oscillations the tip does not ‘see’ the non-linearity and the resonance is very well approximated by the harmonic oscillator. For a stronger driving the resonance line in

the amplitude vs. frequency plot is bent to the left side due to the attractive non-linear interaction. The resonance folds (red), i.e., there is more than one possible amplitude for a given frequency as for example in points A and B. This leads to bistability, where the system can oscillate either with a large or a small amplitude. Between the two stable solutions there is an unstable periodic solution (dotted line). The bistability is responsible for the hysteresis during a frequency sweep as indicated with the arrows. The black dashed line is the backbone line of the non-linear resonance. (b) The same plot for a purely repulsive interaction. (c) Non-linear resonance for a combined attractive-repulsive potential. The two possible solutions, A_H and A_L are marked. Adapted with permission from reference [9].

Bistability is caused by the fact that more than one solutions of the equation of motion of an oscillating cantilever are possible for the same frequency, as shown numerically by Garcia and San Paulo [10]. The two solutions, one at high amplitude (A_H) and one at low amplitude (A_L) can be explained by the coexistence of the attractive and repulsive regimes. The solution A_H corresponds to the repulsive regime, while A_L corresponds to the attractive regime. Experimentally, bistability has been observed by multiple authors as discontinuities in amplitude versus frequency graphs [11]–[15].

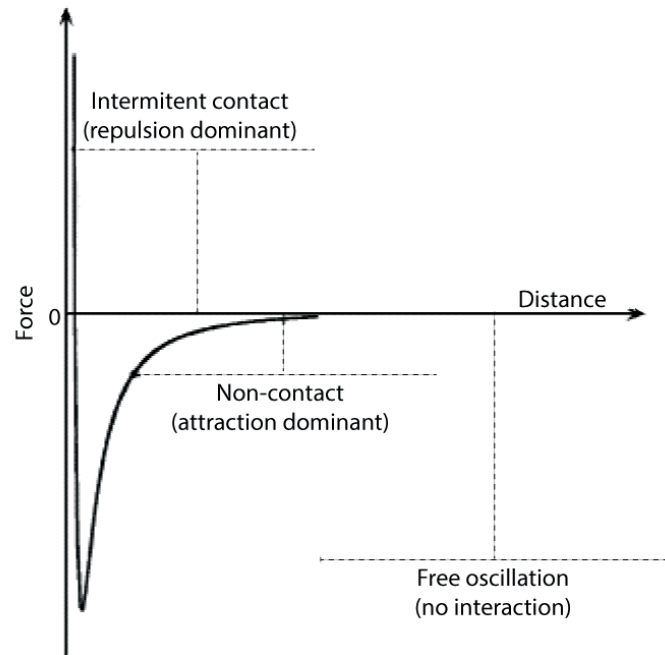


Figure 3.5: Schematic illustration of three distance-dependent regimes of interaction between an oscillating cantilever and a sample surface. The horizontal dashed lines mark the distance intervals explored by the tip at the attractive and repulsive interaction regimes, as well as the no interaction regime. Intermittent contact and non-contact regimes overlap for a small area, resulting in a bistable regime. Adapted with permission from reference [11].

3.4. Conservative and dissipative forces in Atomic Force Microscopy

Regardless of whether the net tip-sample interaction force is positive or negative, a number of different tip-sample interaction forces, F_{ts} , typically act on a cantilever during one period of oscillation, each influencing the motion of the cantilever differently. The variety of forces acting during an oscillation period makes it difficult for the tip-surface interaction to be properly identified and quantified. Under carefully controlled operating conditions however, it is possible to isolate the type of interaction, extracting quantifiable information about material properties.

As two general categories of tip-surface interaction types, one can divide the forces into conservative and dissipative.

Conservative forces for a dynamic AFM experiment performed in ambient conditions, include van der Waals forces [3], [16], capillary forces [3], [16], [17], and contact mechanics forces [1], [3]. Contact mechanics forces are considered dominant in the framework of the presented experimental work and are discussed in detail below.

Dissipative forces are often present in a dynamic AFM experiment and provide an important source of material contrast. The mechanisms of energy dissipation in dynamic AFM operated in air can be divided into surface adhesion hysteresis and velocity dependent processes [16], [18], [19].

3.4.1. Contact mechanics forces

Contact mechanics forces are used to model the interaction between two bodies and their deformation upon contact. The deformation can be fully recovered, in which case the contact is described as elastic, partly recovered, with the deformation referred to as elastoplastic, or permanent, described as plastic deformation. Elastic, plastic, and elastoplastic deformation can be exhibited by any and all materials, depending on the applied load and the material properties. The most commonly used contact mechanics models are presented here, for the elastic contact between a spherical indenter and a flat surface, which most closely resembles the AFM tip and sample geometries.

A handy tool to determine which model is suitable to describe the contact between a tip and sample is the adhesion map shown in Figure 3.6, proposed by Johnson and Greenwood [20]. The map is divided in areas characterized by the ratio of load to adhesive forces and the elasticity parameter, λ .

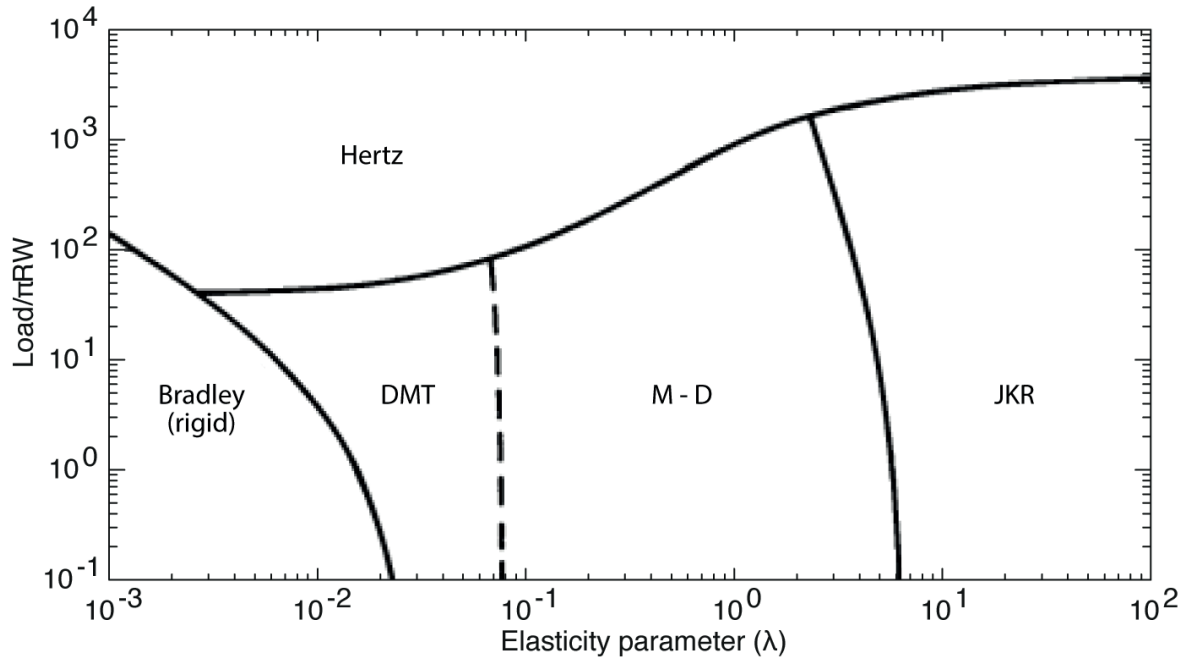


Figure 3.6: Adhesion map for the mechanical contact of elastic bodies, showing the range of application for each contact mechanics model. Adapted with permission from reference [20].

Hertz model

Historically, the elastic contact between two infinite bodies without any adhesive forces was the first to be mathematically formulated, by Hertz. Hertz contact theory does not take into account surface or adhesive forces. At zero load there is no contact between the two bodies. The simple Hertz model for the elastic contact between a spherical indenter of radius R (in the case of the AFM the tip) and a flat surface is given by equation 3.22, and describes the relationship between applied load, deformation (indentation, δ) and material properties, in particular effective elasticity as expressed by Young's modulus [1], [3], [21].

$$F_{Hertz} = \frac{4}{3} \pi E^* \sqrt{R} \delta^{3/2} \quad (3.22)$$

At this point the distinction between the effective elasticity, E^* , and the Young's modulus for either body, E_1 and E_2 or, in the case of AFM tip and sample, E_t and E_s respectively, should be made. E^* , as defined by Hertz, is the convoluted elasticity of the indenter, in this case the tip, and the sample:

$$\frac{1}{E_{eff}} = \frac{1 - \nu_s^2}{E_s} + \frac{1 - \nu_t^2}{E_t} \quad (3.23)$$

In the case of soft materials $E_s \ll E_t$ resulting in $1 - \nu_s^2/E_s \gg 1 - \nu_t^2/E_t$. Moreover, $\nu_s^2 \ll 1$, leading to $1 - \nu_s^2/E_s \approx 1/E_s$. Equation 3.23 can be simplified and $E_{eff} \approx E_s$.

Derjaguin-Muller-Toporov (DMT) Model

The DMT theory describes the elastic contact between two bodies, while taking into account adhesion forces acting outside the contact area, as per equation 3.24 [1], [3], [22]. The adhesive forces produce a finite contact area, irrespective of the external load.

$$F_{adh} = -4\pi R\gamma \quad (3.24)$$

γ denotes surface energy, with $W_{adh} = 2\gamma$ the work required to separate two surfaces in contact.

The repulsive force between the bodies is described by equation 3.25, and the total force acting on the cantilever for $d \leq a_o$ is the sum of the adhesive and repulsive force, as shown in equation 3.26.

$$F_{rep} = \frac{4}{3}\pi E^* \sqrt{R}(a_o - d)^{3/2} \quad (3.25)$$

$$F_{DMT} = -4\pi R\gamma + \frac{4}{3}\pi E^* \sqrt{R}(a_o - d)^{3/2} \quad (3.26)$$

DMT theory is applicable for low adhesion forces and small tip radii.

Johnson-Kendall-Roberts (JKR) model

The JKR theory considers only short-range adhesion forces, given by equation 3.27, acting inside the contact area [1], [3], [23].

$$F_{adh} = 3\pi R\gamma \quad (3.27)$$

Indentation, δ , can be calculated as per equation 3.28.

$$\delta = \frac{a^2}{R} - \frac{8}{3} \sqrt{\frac{3\pi\gamma a}{E^*}} \quad (3.28)$$

The contact radius, a , can be expressed as a function of applied and adhesive force:

$$a = \sqrt[3]{\frac{R}{E^*} \left[F_{JKR} + 6\pi R\gamma + 2 \sqrt{3\pi R\gamma F_{JKR} + (3\pi R\gamma)^2} \right]} \quad (3.29)$$

The JKR theory behaves hysteretically and is suitable for highly adhesive systems and large tip radii.

3.5. Multifrequency Atomic Force Microscopy

As briefly discussed in paragraph 3.2, the motion of an oscillating cantilever is most frequently considered as dominated by only one flexural mode. However, as short-distance forces have an extinction length typically lower than that of the commonly used oscillation amplitude (1 nm versus > 5 nm respectively), a non-linear net tip-sample force is acting on the cantilever during one period of oscillation. This, intrinsic to the system, non-linearity, introduces motion components from the higher harmonics, encoded in the frequency spectra. Following the simple scheme presented by equation 3.7, the experimental observables are mostly used to reconstruct surface topography. The additional information encoded in the higher frequency components of the motion is lost.

Multifrequency AFM has been developed recently, in order to address this issue. The basic concept is to excite the cantilever at multiple frequencies, distinct or a whole band, and take advantage of the extra experimental observables to gain a particular insight into materials' properties (electric, magnetic, mechanical etc.), while using the fundamental frequency to track the topography. The scheme of multifrequency excitation also offers the advantage of enhancing the amplitude of the higher eigenmodes, easing their detection, while the sensitivity of the additional mode is also enhanced by the coupling between simultaneously excited eigenmodes, improving the sensitivity of the second mode to material properties [24].

Multiple schemes of multifrequency AFM have been developed. The most widely used include multiharmonic AFM imaging, bimodal AFM, band excitation, torsional harmonic AFM and nanomechanical holography [25].

3.5.1. Multiharmonic AFM imaging

In this mode, the cantilever is excited at one frequency, usually the first eigenmode. Harmonic frequency components are generated and can be seen in the Fourier space. The amplitude and phase at the driving frequency are monitored by one lock-in amplifier, and the received signal is used for imaging. The amplitude of a higher harmonic is monitored by a second lock-in amplifier and plotted independently [26].

3.5.2. Band excitation

In Band excitation AFM the cantilever is excited by a composite signal generated by a band of frequencies centered around one of the eigenmodes. The signal, produced in the frequency domain, is inverse FFT to the temporal space and used to excite the cantilever. The response temporal signal is then FFT back into the frequency domain and amplitude-frequency and phase-frequency curves are generated. Using this information the energy dissipated at each point can be calculated and areas where different energy dissipation takes place can be highlighted in the produced 2D images [27].

3.5.3. Torsional harmonic AFM

In torsional harmonic AFM, as in multiharmonic AFM, the cantilever is driven at one frequency, usually the first eigenmode, and information is collected for additional frequencies, in this case the torsional harmonics. The cantilevers used for this technique are usually specially fabricated, with the tip being offset from the main longitudinal axis. The non-linear tip-sample interaction generates a torque, which, in turn, leads to an enhanced lateral deflection. The vertical deflection signal is used to plot the topography of the surface, while the lateral deflection is used for obtaining simultaneous information on material properties. The torsional harmonics are more sensitive to local variations in material properties as they are only excited by the tip-sample forces and not the driving force. Moreover, the torsional harmonics are typically at higher frequencies than the flexural harmonics. Since the bandwidth is limited by the frequency, torsional harmonic AFM provides better time resolution [28].

3.5.4. Nanomechanical holography

In nanomechanical holography both the cantilever and the sample are excited, the first acoustically as in regular dynamic AFM imaging, the latter mechanically from below. The mechanical excitation of the sample generates waves, which, as they travel through the sample, are scattered and deflected by the material's subsurface structure. The propagating waves reaching the surface, exhibiting a phase and amplitude shift depending on the mechanical properties of the buried structures they have already interacted with, provide an additional tip-sample interaction force. The main contrast mechanisms are the amplitude shift between the matrix and the matrix-buried structure and the phase shift between the matrix and matrix-buried structures. The former is caused by wave scattering from the buried obstacles. The latter is related to the shift of the tip-sample interaction stiffness, Δk^* , due to differences between the tip-matrix interaction stiffness and the tip-matrix-buried structure stiffness. Δk^* is related to phase shift via a coefficient dependent on cantilever, sample and oscillation parameters [29]. Nanomechanical holography, in the form of Ultrasonic Force Microscopy (UFM), Heterodyne Force Microscopy (HFM), Atomic Force Acoustic Microscopy (AFAM) and Scanning Near Field Ultrasonic Holography (SNFUH) can provide information on subsurface structures both in soft and hard systems. However, the complexity of the required setup and the difficulties of properly interpreting the received data hinder the wider use of the technique.

3.5.5. Bimodal AFM

In bimodal AFM the cantilever is excited using two driving forces at frequencies matching two of its eigenmodes, usually the first and second. The complex driving signal generates a complex movement, described in its general form by equation 3.30 [25], where q_i the temporal component of the movement of the i^{th} eigenmode and n refers to the harmonics.

$$z(t) = z_o + \sum_{i=1}^M q_i(t) = z_o + \sum_{n=1}^N A_n \cos(n\omega t - \varphi_n) \quad (3.30)$$

Equation 3.30 can be simplified for two driving forces to equation 3.31 [30].

$$z(t) \approx A_1 \cos(\omega_1 t - \varphi_1) + A_2 \cos(\omega_2 t - \varphi_2) \quad (3.31)$$

Information on A_i , φ_i and ω_i is collected from the electronics of the AFM and used to reconstruct the desired information. Usually the first eigenmode is used to track surface topography, while the higher eigenmode, carried along the first, is used to extract information on material properties. Bimodal AFM is compatible with operation both in air and liquid, and can be performed in the attractive [31], [32] and repulsive [33]–[36] regime, depending on the information the user wishes to gain access to.

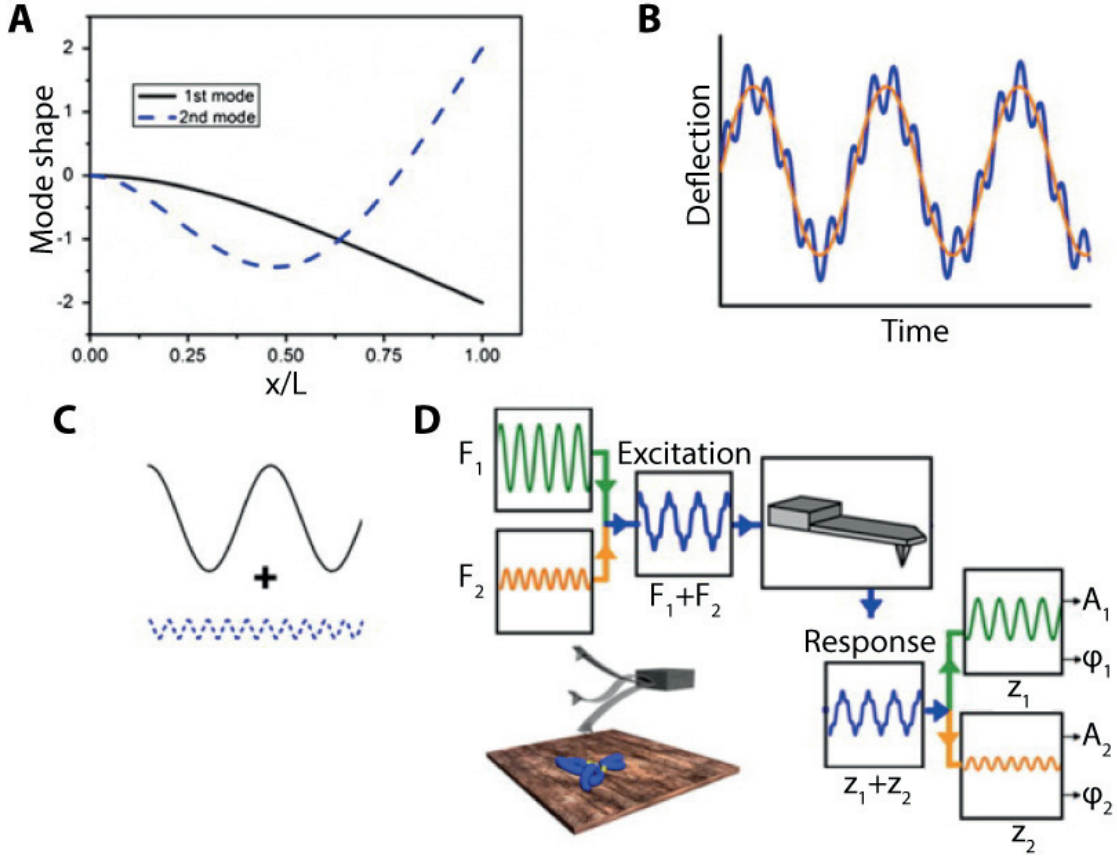


Figure 3.7: Shape of the first and second eigenmodes for a tipless rectangular cantilever (A). Scheme of the bimodal tip excitation (B) resulting from the combination of the two frequencies (C). Schematic representation of a bimodal AFM experiment in the AM-AM configuration (D). Reproduced with permission from reference [35].

The expression of the experimental observables as a function of any tip-sample interaction forces can be achieved if the energy conservation theory and the virial theorem are applied to the tip-sample interaction forces, as demonstrated by Lozano and Garcia for the continuous beam [30], [37]. Following the mathematical derivation proposed by the authors, the dissipated energy over one period of oscillation, $E_{ts}(i)$, can be calculated for each eigenmode as per equation 3.32. Conversely, the virial of each eigenmode, $V_{ts}(i)$, can be expressed by equation 3.33.

$$E_{ts}(i) \equiv - \int_0^T F_{ts}(d) \dot{z}_i(t) dt \quad (3.32)$$

$$V_{ts}(i) = \frac{1}{T} \int_0^T F_{ts}(d) z_i(t) dt \quad (3.33)$$

Where d is the instantaneous tip-sample separation, as per equation 3.34, for a continuous beam.

$$d = z_c + w(L, t) \quad (3.34)$$

Substituting equation 3.31 into equations 3.32 and 3.33, it can be calculated for each eigenmode:

$$E_{ts}(i) = \frac{\pi k_i A_i}{Q_i} (A_{o,i} \sin \varphi_i - A_i) \quad (3.35)$$

$$V_{ts(i)} = - \frac{k_i A_{o,i}}{2Q_i} A_i \cos \varphi_i \quad (3.36)$$

The frequency and spring constant of the higher eigenmodes of rectangular cantilevers are related to the spring constant and frequency of the fundamental mode as per equations 3.37 and 3.38 respectively [25], [38].

$$f_n = \left(\frac{\kappa_i}{\kappa_1} \right)^\zeta f_1 \quad (3.37)$$

$$k_i = k_1 \left(\frac{f_n}{f_1} \right)^\zeta \quad (3.38)$$

The operator ζ can be experimentally determined for any cantilever and accounts for the deviation of the real shape of a rectangular cantilever from the rectangular beam. Some values for commonly used cantilevers have been determined by Labuda et al. [38]. As the process for calculating ζ is not trivial, the value is often set to 2.

Equations 3.35 and 3.36 show how experimental observables, such as amplitude and frequency shift, are related to tip-sample processes, allowing for material contrast to be obtained. Depending on the operating mode (AM, FM, PM), the absence or not of non-conservative forces, and the specific operating conditions, the above equations can be further simplified [30], [35], [39], [40]. Equations 3.35 and 3.36 are true for any tip-sample interaction force, and can thus be solved to correlate the experimental observables to specific material properties.

One of the most interesting applications of bimodal AFM has been its use for nanomechanical characterization of soft matter. Operating in the repulsive regime, the mechanical contact between the tip and the sample can be modeled using a suitable contact mechanics model and the oscillation parameters correlated to material mechanical properties [33], [36], [41]. Effective surface elasticity, E^* , and indentation, δ , can be calculated for $A_1 \gg \delta$ and a spherical tip shape as per equations 3.39 and 3.40 respectively [36].

$$E^* = \sqrt{\frac{32}{R}} Q_1 \sqrt{\frac{A_1}{A_{o,1}^2 - A_1^2} \frac{k_2^2 \Delta f_2^2}{k_1 f_{o,2}^2}} \quad (3.39)$$

$$\delta = \frac{1}{2} \frac{k_1}{Q_1} \frac{f_{o,2}}{k_2 \Delta f_2} \sqrt{A_{o,1}^2 - A_1^2} \quad (3.40)$$

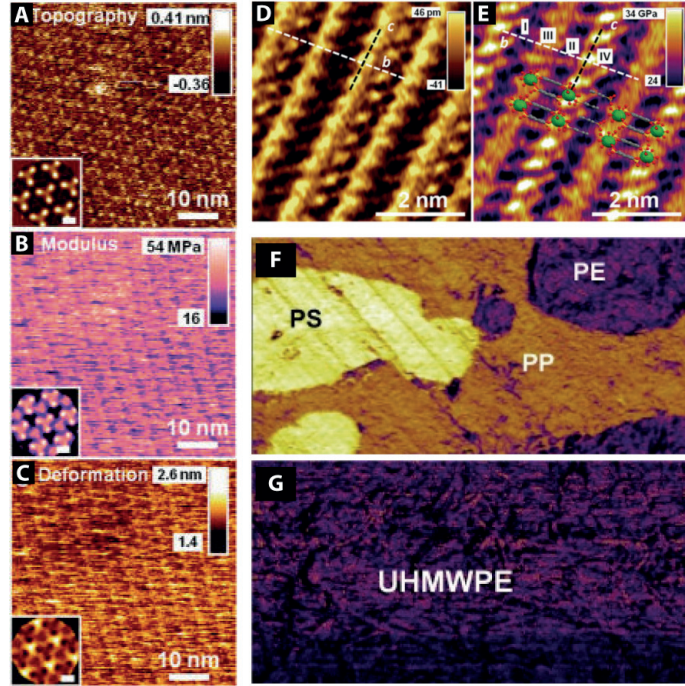


Figure 3.8 (A-G): Bimodal AFM can provide accurate nanomechanical characterization of a wide range of materials, showing good material contrast and obtaining subnanometer resolution. Topography (A), elasticity (B) and deformation δ (C) for purple membrane in buffer solution. The insets show the 3-fold symmetrized averages of each channel (scale bar 2 nm). Topography (D) and elasticity (E) of a Ce, O, S metal-organic framework. Reproduces with permission from reference [36]. Elasticity map of ternary polymer blend of polystyrene (PS), polyethylene (PE) and polypropylene (PP) (G) and elasticity of ultra-high molecular weight polyethylene (UHMWPE). Reproduced with permission from reference [35].

3.5.5.1. Using Bimodal AFM for nanomechanical characterization of soft matter

Bimodal AFM can provide information on a number of material properties, including magnetic [42], electrostatic [43], and adhesive interactions [44]. When operating in a net-repulsive regime, mechanical contact between the tip and sample is achieved [33]. A suitable contact mechanics model can then be used to model the tip-sample interaction forces, which, in turn, can be expressed in terms of the cantilever's characteristics or parameters of oscillation.

As used by Amo et al. [36] and Herruzo et al. [41], among others, the mechanical properties of a material in terms of Young's modulus, E , and viscosity, η , can be correlated to experimental observables as briefly described in paragraph 3.5.5. A different approach towards a mathematical formulation between F_{ts} and experimental observables, based on the concept of the weakly perturbed oscillator, has been provided by Labuda et al. [45] and is briefly explained here.

The interaction stiffness between the tip and sample as a function of the vertical displacement, z , or the indentation depth, δ , can be expressed by equation 3.41.

$$k_{int}(z) = \frac{\partial F}{\partial z} \text{ or } k_{int}(\delta) = \frac{\partial F}{\partial \delta} \quad (3.41)$$

Assuming that the conservative forces are dominant, the contact between the tip and sample is considered purely elastic [35]. Using a simple general Hertzian contact model [1], [21], the interaction stiffness between the tip and the sample can be calculated as per equation 3.42 [45], where E_{eff} is the tip-sample effective Young's modulus, α_c the contact radius correction factor, L the characteristic length scale of the tip which depends on tip shape and size, and δ the indentation depth.

$$k_{int}(\delta) = 2E^*\alpha_c L^{2-m} \delta^{m-1} \quad (3.42)$$

The parameter $m \in [1,2]$ is related to tip shape and can take different values within the defined field. For a paraboloid tip, which most closely resembles a typical commercially available AFM tip, $m = 3/2$, L equals tip diameter $2R$ and $\alpha_c = \sqrt{1/2}$ and equation 3.42 can be simplified as such:

$$k_{int}(\delta) = 2E^*\sqrt{R\delta} \quad (3.43)$$

To calculate the time-averaged change in effective stiffness of each eigenmode, Δk_i , the interaction stiffness, $k_{int}(\delta)$, will be integrated over one period of oscillation for each eigenmode. For the first eigenmode, Δk_1 can be calculated by integrating $k_{int}(\delta(t))$ for one cycle of oscillation, using a semi-circular weighing function [46], [47] and replacing the variable $\delta(t)$ with the modified distance, $u = (\delta_{max} - \delta)/A_1$.

$$\Delta k_1 = \frac{2}{\pi} \int_0^2 k_{int}(\delta_{max} - uA_1) \sqrt{2u - u^2} du \quad (3.44)$$

For $A_1 \gg \delta_{max}$ it is approximated that $\sqrt{2u - u^2} \cong \sqrt{2u}$. With this simplification and replacing equation 3.43 into equation 3.44, the time average change in stiffness of the first eigenmode can be related to the effective Young's modulus and maximum indentation as per equation 3.45.

$$\Delta k_1 = \sqrt{\frac{R}{2A_1^3}} E^* \delta_{max}^2 \quad (3.45)$$

The higher eigenmode is driven at amplitude $A_{o,2} \ll A_{o,1}$ [48], [49]. Under these conditions, Δk_2 does not vary significantly during one oscillation cycle spanning from $-A_2$ to A_2 , but does vary as it rides on the oscillation cycle of the first eigenmode [31]. In order to calculate Δk_2 , $k_{int}(\delta(t))$ is integrated over one period of oscillation of the first eigenmode.

$$\Delta k_2 = \frac{1}{T} \int_0^T k_{int} \delta(t) dt \quad (3.46)$$

Substituting $t = \cos^{-1}(u)/\omega_1$ and using the weighing function $1/\sqrt{2u - u^2}$, which, as for the first mode, can be approximated by $1/\sqrt{2u}$, equation 3.46 can be rewritten as:

$$\Delta k_2 = \frac{1}{\pi} \int_0^2 k_{int}(\delta_{max} - uA_1) \frac{1}{\sqrt{2u}} du \quad (3.47)$$

Replacing equation 3.43 into equation 3.47, the time average change in stiffness for the second mode can be calculated:

$$\Delta k_2 \approx \sqrt{\frac{R}{2A_1}} E^* \delta_{max} \quad (3.48)$$

The system of equations 3.45 and 3.48 can be solved for E_{eff} and δ_{max} , resulting in equations 3.49 and 3.50.

$$E^* = \sqrt{\frac{2}{RA_1} \frac{\Delta k_2^2}{\Delta k_1}} \quad (3.49)$$

$$\delta_{max} = A_1 \frac{\Delta k_1}{\Delta k_2} \quad (3.50)$$

In this way, the effective material elasticity as expressed by Young's modulus, E_{eff} , and the maximum sample indentation, δ_{max} , can be measured experimentally, through Δk_1 and Δk_2 .

Δk_i can be experimentally measured as a function of cantilever characteristics and operating conditions [45], [50]:

$$\Delta k = k_c \left(\frac{\omega^2}{\omega_c^2} - 1 \right) + \frac{k_c}{Q_c} \left(\frac{A_r}{A} \frac{D}{D_r} \cos \varphi \right) \quad (3.51)$$

The proposed equation 3.51 is true for all dynamic AFM operation modes when the cantilever is driven at resonance. The parameters k_c and Q_c are characteristics of each mode of the cantilever. The selection between the operating parameters ω , ω_c , A_r , A , D , D_r and φ , as to which will be kept constant and which will be left free to vary during an AFM measurement depends on the selected operating configuration and is eigenmode invariant.

In the AM configuration, $D = D_r$ and $\omega = \omega_c$, and one can calculate:

$$\Delta k^{AM} = \frac{k_c}{Q_c} \frac{A_r}{A} \cos \varphi \quad (3.52)$$

In the FM configuration, $A = A_r$, $\varphi = \pi/2$ and one calculates [47]:

$$\Delta k^{FM} = 2k_c \frac{\Delta \omega}{\omega_c} = 2k_c \frac{\Delta f}{f_c} \quad (3.53)$$

In the PM configuration, setting $A = A_r$ and $\omega = \omega_c$:

$$\Delta k^{PM} = \frac{k_c}{Q_c} \frac{D}{D_r} \cos \varphi \quad (3.54)$$

Each mode can be used for each driving eigenmode. Of all the possible configuration combinations, the most widely used are the AM-AM, FM-FM and AM-FM.

In the present thesis the mode bimodal operation was carried out using the AM-FM configuration (AM-FM, US patents 8,024,963, 7,937,991, 7,603,891, 7,921,466 and 7,958,563 with others pending, Oxford Instruments Asylum Research, Inc., Santa

Barbara, CA, USA). The first eigenmode was operated in amplitude modulation (AM) and the higher eigenmode, always the second unless otherwise specified, was operated in frequency modulation (FM). Under these conditions, $\Delta k_1 = \Delta k^{AM}$ and $\Delta k_2 = \Delta k^{FM}$, and equation 3.49 can be expanded to an experimentally friendly form:

$$E^* = \sqrt{\frac{32}{R} \frac{\sqrt{A_1}}{A_{o,1}} \frac{k_2}{k_1} \frac{k_2 Q_1}{f_{o,2}^2} \Delta f^2 \frac{1}{\cos \varphi_1}} \quad (3.55)$$

3.5.5.2. Nanomechanical characterization of SAMs by bimodal AFM in the AM-FM configuration

In order to obtain an operating conditions-independent nanomechanical characterization of soft matter in general and organic self-assembled monolayers (SAMs) in particular, some parameters need to be considered.

Amplitude ratio of fundamental and higher eigenmodes

The ratio of free amplitude between the oscillation parameters of the first and higher eigenmodes is an important parameter for tuning the cantilever's response to material properties [48], [49], [51], [52]. The fundamental and the higher eigenmodes are slightly coupled, so energy transfer between them is possible, leading to chaotic cantilever motion [9]. A stabilized repulsive regime in bimodal AFM has been experimentally observed [53]. Stark demonstrated that for $A_{o,1}$ comparable to $A_{o,2}$ the motion of the cantilever is no longer periodic; rather, quasiperiodic jumps between the attractive and repulsive regimes are present, while the phase response of both the first and the higher mode was unstable [51]. Optimum operating conditions were determined for $A_{o,1}:A_{o,2}$ equal to 4:1. Gigler et al. further demonstrated that for bimodal operation in the attractive regime stable imaging and material contrast was obtained for $A_{o,1}:A_{o,2}$ smaller than 10:1, while for operation in the repulsive regime the ratio should be maintained above 10:1 [52].

Regarding material contrast, it was suggested by Stark that the parameter influencing the AFM operation in the bimodal scheme was in fact the ratio of the energy stored in each mode, $E_1:E_2$, and not the ratio of amplitudes [51]. The experimental and theoretical results obtained by Kiracofe et al. further supported this claim. Imaging a ternary polymer blend while maintaining $A_{o,1}:A_{o,2} > 10:1$, it was demonstrated that material

contrast was reversed when the energy of the two modes was comparable [49]. This observation can be related to the energy dissipated by each mode.

Work to free amplitude ratio of the fundamental eigenmode

The mathematical formulation previously described, relating experimental observables to mechanical properties, was carried out for operation in the repulsive regime, considering only conservative forces. An operational range for $A_1:A_{o,1}$ in which both mechanical contact between the tip and sample is maintained, while simultaneously no plastic deformation is induced, needs to be determined. In this regime the measured moduli are independent of the operating conditions. An octadecylphosphonic acid SAM was scanned in the AM-FM configuration. $A_{o,1}$ was kept constant and A_1 was changed approximately every 100nm in the slow scan direction. $A_{o,1}:A_{o,2}$ was kept at 50:1. The sample's Young's modulus was calculated at each interval and was found constant for $A_1:A_{o,1} \in [0.65, 0.80]$ (see Figure 3.9). It should be stressed that the absolute values of A_1 and $A_{o,1}$ do not greatly affect the measured E values; rather it is the ratio of the two that significantly affects the force at which the sample is probed. As demonstrated by Rodriguez and Garcia, when $A_{o,1} \gg A_{o,2}$, φ_1 does not show any material contrast [31]. In fact, solving equation 3.35 for negligible energy dissipation, it is clear that φ_1 depends only on the ratio $A_1:A_{o,1}$. Therefore, as long as the conditions $A_{o,1} \gg A_{o,2}$ and $A_1:A_{o,1} \in [0.65, 0.80]$ are met, the absolute values of the free and work amplitude of the first mode can be varied. It should be noted that experimentally it has been observed that extremely high values of $A_{o,1}$ lead to high vibrational noise.

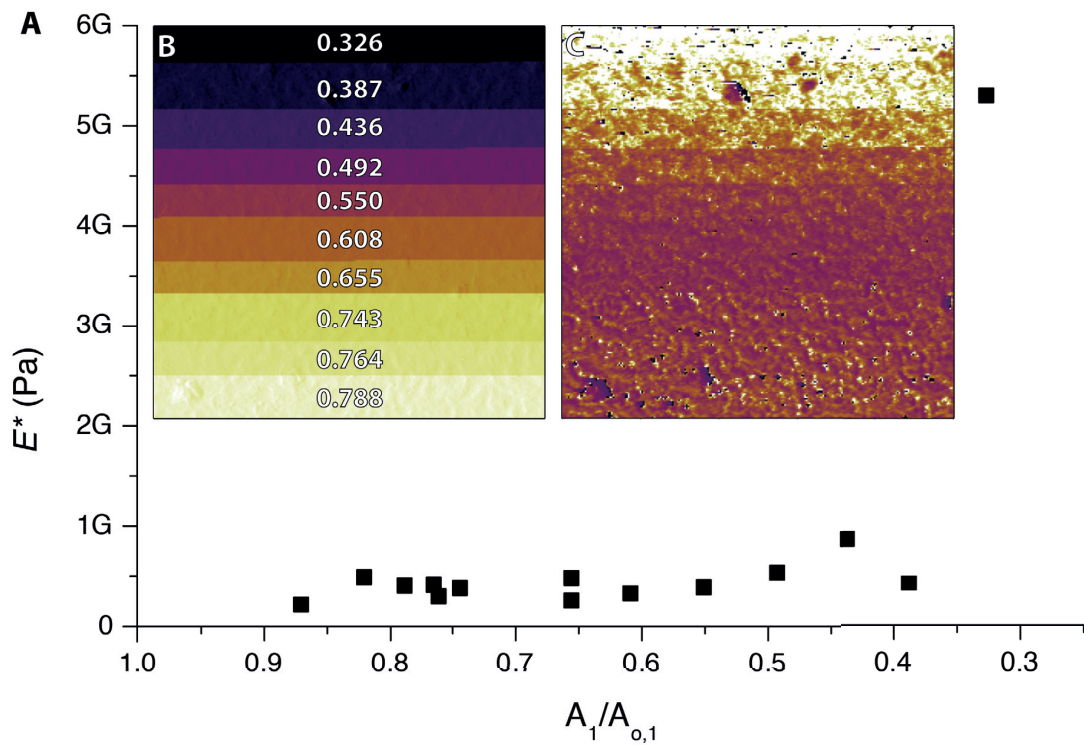


Figure 3.9 (A-C): E dependence on imaging conditions experimentally determined at 400kHz using nominal tip shape sphere and $R = 10\text{nm}$ for ODPA SAMs (A). Work (A_I) to free ($A_{0,I}$) amplitude ratio (B) and corresponding E^* (C).

Tip shape and size

Equations 3.39 and 3.55 have been rigorously derived for a paraboloid tip of radius R . Nonetheless, the tip shape and size should be calibrated. For the most accurate calibration, the cantilever tip can be imaged via Scanning Electron Microscopy (SEM); the radius can be directly measured and the shape confirmed. This method however is time and resources consuming and, therefore, not ideal for day-to-day use. An indirect and widely used calibration method involves the scanning of a reference sample of known mechanical properties; R and shape are backcalculated from the experimentally recorded values of E and modulated in order to obtain the known value of the sample's elasticity. The calibration sample used should have nanomechanical properties close to the expected values of the material to be measured. In the present thesis all cantilevers were calibrated on a polystyrene (PS) calibration thin film ($12\text{ }\mu\text{m}$, Bruker, Santa Barbara, CA, U.S.A.) with nominal Young's modulus $E = 2\text{ GPa}$.

Cantilever characteristics

As seen in equation 3.55, effective Young's modulus, E^* , is calculated as a function of oscillation parameters and cantilever characteristics like resonance frequency,

frequency of the higher modes, spring constant of the fundamental and higher modes, frequency shift of the higher mode. The cantilever characteristics take different values for different probe types. As a result, the values of E^* , as well as δ_{max} , calculated by bimodal AFM for different probe types will be numerically different, none the least because the sensitivity of probes with variable stiffness to the same forces will be different. In order for the obtained data to be comparable it is important that the same probe type is consistently used for all samples.

This effect can also be seen when different combinations of the first and higher eigenmodes are used, for example the first and second versus the first and third eigenmodes. Since $E^* \propto k_i/f_i$, where i the higher eigenmode, it can be written, for the combination first and second:

$$E^*_{1,2} \propto \frac{k_2}{f_2} = \frac{(f_2/f_1)^2 k_1}{(\kappa_2/\kappa_1)^2 f_1} \cong \frac{39.31 k_1}{6.27 f_1} \quad (3.56)$$

And for the first and third:

$$E^*_{1,3} \propto \frac{k_3}{f_3} = \frac{(f_3/f_1)^2 k_1}{(\kappa_3/\kappa_1)^2 f_1} \cong \frac{308 k_1}{17.55 f_1} \quad (3.57)$$

Even though the same material properties will be probed [49], numerically the two values, $E^*_{1,2}$ and $E^*_{1,3}$ will be different. It is therefore important for the same combination of first and higher eigenmode to be consistently used for all samples.

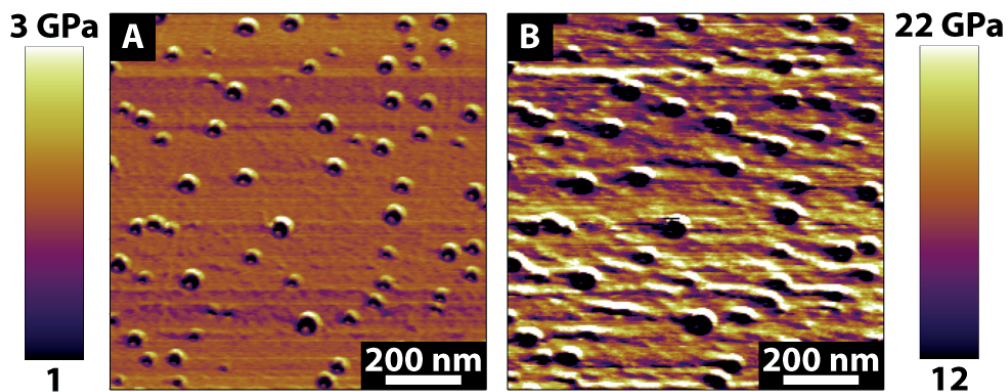


Figure 3.10: Recorded E^* of the same area of polystyrene (PS) at 400 kHz (first and second eigenmodes) (A) and 1 MHz (first and third eigenmodes) (B).

3.6. References

- [1] B. Cappella and G. Dietler, "Force-distance curves by atomic force microscopy," *Surf. Sci. Rep.*, vol. 34, no. 1–3, pp. 1–104, 1999.
- [2] R. García and R. Perez, "Dynamic atomic force microscopy methods," *Surf. Sci. Rep.*, vol. 47, no. 6–8, pp. 197–301, 2002.
- [3] R. Garcia, *Amplitude Modulation Atomic Force Microscopy*, 1st ed. Weinheim, Germany: Wiley-VCH Verlag GmbH & Co. KGaA, 2010.
- [4] B. Voigtländer, *Scanning Probe Microscopy*, 1st ed. Heidelberg, Germany: Springer, 2015.
- [5] A. Raman, J. Melcher, and R. Tung, "Cantilever dynamics in atomic force microscopy," *Nano Today*, vol. 3, no. 1–2, pp. 20–27, 2008.
- [6] Á. Paulo and R. García, "Tip-surface forces, amplitude, and energy dissipation in amplitude-modulation (tapping mode) force microscopy," *Phys. Rev. B*, vol. 64, no. 19, pp. 1–4, 2001.
- [7] Á. Paulo and R. García, "Unifying theory of tapping-mode atomic-force microscopy," *Phys. Rev. B*, vol. 66, no. 4, pp. 2–5, 2002.
- [8] T. R. Rodríguez and R. García, "Tip motion in amplitude modulation (tapping-mode) atomic-force microscopy: Comparison between continuous and point-mass models," *Appl. Phys. Lett.*, vol. 80, no. 9, pp. 1646–1648, 2002.
- [9] R. W. Stark, "Bistability, higher harmonics, and chaos in AFM," *Mater. Today*, vol. 13, no. 9, pp. 24–32, 2010.
- [10] R. García and A. San Paulo, "Dynamics of a vibrating tip near or in intermittent contact with a surface," *Phys. Rev. B*, vol. 61, no. 20, pp. R13381–R13384, 2000.
- [11] G. Haugstad and R. R. Jones, "Mechanisms of dynamic force microscopy on polyvinyl alcohol: Region- specific non-contact and intermittent contact regimes," *Ultramicroscopy*, vol. 76, no. 1–2, pp. 77–86, 1999.
- [12] A. Kühle, A. H. So/rensen, and J. Bohr, "Role of attractive forces in tapping tip force microscopy," *J. Appl. Phys.*, vol. 81, no. 10, pp. 6562–6569, 1997.
- [13] P. Gleyzes, P. K. Kuo, and A. C. Boccara, "Bistable behavior of a vibrating tip near a solid surface," *Appl. Phys. Lett.*, vol. 58, no. 25, pp. 2989–2991, 1991.
- [14] R. Boisgard, J. P. Aimé, and G. Couturier, "Dynamic operation modes of AFM: Non-linear behavior and theoretical analysis of the stability of the AFM oscillator," *Int. J. Non. Linear. Mech.*, vol. 42, no. 4, pp. 673–680, 2007.
- [15] B. Anczykowski, D. Krüger, and H. Fuchs, "Cantilever dynamics in quasiconnact

- force microscopy: Spectroscopic aspects," *Phys. Rev. B*, vol. 53, no. 23, pp. 15485–15488, 1996.
- [16] J. Israelachvili, *Intermolecular and Surface Forces*, 3rd ed. Waltham, MA, USA: Academic Press, 2011.
 - [17] L. Zitzler, S. Herminghaus, and F. Mugele, "Capillary forces in tapping mode atomic force microscopy," *Phys. Rev. B*, vol. 66, no. 15, p. 155436, 2002.
 - [18] R. Garcia, C. J. Gómez, N. F. Martinez, S. Patil, C. Dietz, and R. Magerle, "Identification of nanoscale dissipation processes by dynamic atomic force microscopy," *Phys. Rev. Lett.*, vol. 97, no. 1, pp. 1–4, 2006.
 - [19] C. J. Gómez Carlos J. and R. Garcia, "Determination and simulation of nanoscale energy dissipation processes in amplitude modulation AFM," *Ultramicroscopy*, vol. 110, no. 6, pp. 626–633, 2010.
 - [20] K. L. Johnson and J. A. Greenwood, "An adhesion map for the contact of elastic spheres," *J. Colloid Interface Sci.*, vol. 192, no. 2, pp. 326–333, 1997.
 - [21] K. L. Johnson, "Normal contact of elastic solids: Hertz theory," in *Contact Mechanics*, 9th ed., Cambridge, UK: Cambridge University Press, 2003, pp. 84–106.
 - [22] B. V Derjaguin, V. M. Muller, and Y. U. P. Toporov, "Effect of contact deformation on the adhesion of particles," *J. Colloid Interface Sci.*, vol. 52, no. 3, pp. 105–108, 1975.
 - [23] K. L. Johnson, K. Kendall, and A. D. Roberts, "Surface Energy and the Contact of Elastic Solids," *Proc. R. Soc. A Math. Phys. Eng. Sci.*, vol. 324, no. 1558, pp. 301–313, 1971.
 - [24] D. Forchheimer, R. Forchheimer, and D. B. Haviland, "Improving image contrast and material discrimination with nonlinear response in bimodal atomic force microscopy," *Nat. Commun.*, vol. 6, p. 6270, 2015.
 - [25] R. Garcia and E. T. Herruzo, "The emergence of multifrequency force microscopy," *Nat. Nanotechnol.*, vol. 7, no. 4, pp. 217–226, 2012.
 - [26] R. Hillenbrand, M. Stark, and R. Guckenberger, "Higher-harmonics generation in tapping-mode atomic-force microscopy: Insights into the tip-sample interaction," *Appl. Phys. Lett.*, vol. 76, no. 23, p. 3478, 2000.
 - [27] S. Jesse, S. V. Kalinin, R. Proksch, A. P. Baddorf, and B. J. Rodriguez, "The Band Excitation Method in Scanning Probe Microscopy for Rapid Mapping of Energy Dissipation on the Nanoscale," *Nanotechnology*, vol. 18, no. 43, p. 435503, 2007.
 - [28] O. Sahin, S. Magonov, C. Su, C. F. Quate, and O. Solgaard, "An atomic force microscope tip designed to measure time-varying nanomechanical forces," *Nat.*

- Nanotechnol.*, vol. 2, no. 8, pp. 507–14, 2007.
- [29] H. Jiryaeei Sharahi, G. Shekhawat, V. Dravid, S. S. Park, P. Egberts, and S. Kim, “Contrast mechanisms on nanoscale subsurface imaging in ultrasonic AFM: Scattering of ultrasonic wave and contact stiffness of tip-sample,” *Nanoscale*, vol. 9, pp. 2330–2339, 2017.
 - [30] J. R. Lozano and R. Garcia, “Theory of multifrequency atomic force microscopy,” *Phys. Rev. Lett.*, vol. 100, no. 7, pp. 76102-1–4, 2008.
 - [31] T. R. Rodríguez and R. García, “Compositional mapping of surfaces in atomic force microscopy by excitation of the second normal mode of the microcantilever,” *Appl. Phys. Lett.*, vol. 84, no. 3, pp. 449–451, 2004.
 - [32] S. Patil, N. F. Martinez, J. R. Lozano, and R. Garcia, “Force microscopy imaging of individual protein molecules with sub-pico Newton force sensitivity,” *J. Mol. Recognit.*, vol. 20, no. 6, pp. 516–523, 2007.
 - [33] R. Proksch, “Multifrequency, repulsive-mode amplitude-modulated atomic force microscopy,” *Appl. Phys. Lett.*, vol. 89, no. 11, pp. 1–4, 2006.
 - [34] C. Dietz, M. Zerson, C. Riesch, A. M. Gigler, R. W. Stark, N. Rehse, and R. Magerle, “Nanotomography with enhanced resolution using bimodal atomic force microscopy,” *Appl. Phys. Lett.*, vol. 92, no. 14, pp. 1–4, 2008.
 - [35] R. Garcia and R. Proksch, “Nanomechanical mapping of soft matter by bimodal force microscopy,” *Eur. Polym. J.*, vol. 49, no. 8, pp. 1897–1906, 2013.
 - [36] C. A. Amo, A. P. Perrino, A. F. Payam, and R. Garcia, “Mapping elastic properties of heterogeneous materials in liquid with Angstrom-scale resolution,” *ACS Nano*, vol. 11, no. 9, pp. 8650–8659, 2017.
 - [37] J. R. Lozano and R. Garcia, “Theory of phase spectroscopy in bimodal atomic force microscopy,” *Phys. Rev. B - Condens. Matter Mater. Phys.*, vol. 79, no. 1, pp. 1–9, 2009.
 - [38] A. Labuda, M. Kocun, T. Walsh, J. Meinhold, T. Proksch, W. Meinhold, and R. Proksch, “Calibration of higher eigenmodes of cantilevers,” *Rev. Sci. Instrum.*, vol. 87, no. 73705, pp. 1–11, 2016.
 - [39] G. Chawla and S. D. Solares, “Mapping of conservative and dissipative interactions in bimodal atomic force microscopy using open-loop and phase-locked-loop control of the higher eigenmode,” *Appl. Phys. Lett.*, vol. 99, no. 7, pp. 18–21, 2011.
 - [40] E. T. Herruzo and R. Garcia, “Theoretical study of the frequency shift in bimodal FM-AFM by fractional calculus,” *Beilstein J. Nanotechnol.*, vol. 3, no. 1, pp. 198–206,

2012.

- [41] E. T. Herruzo, A. P. Perrino, and R. Garcia, "Fast nanomechanical spectroscopy of soft matter," *Nat. Commun.*, vol. 5, p. 3126, 2014.
- [42] J. W. Li, J. P. Cleveland, and R. Proksch, "Bimodal magnetic force microscopy: Separation of short and long range forces," *Appl. Phys. Lett.*, vol. 94, no. 16, pp. 2007–2010, 2009.
- [43] R. W. Stark, N. Naujoks, and A. Stemmer, "Multifrequency electrostatic force microscopy in the repulsive regime," *Nanotechnology*, vol. 18, no. 6, p. 65502, 2007.
- [44] N. F. Martinez, S. Patil, J. R. Lozano, and R. Garcia, "Enhanced compositional sensitivity in atomic force microscopy by the excitation of the first two flexural modes," *Appl. Phys. Lett.*, vol. 89, no. 15, pp. 1–4, 2006.
- [45] A. Labuda, M. Kocun, W. Meinhold, D. Walters, and R. Proksch, "Generalized Hertz model for bimodal nanomechanical mapping," *Beilstein J. Nanotechnol.*, vol. 7, pp. 970–982, 2016.
- [46] U. Dürig, "Extracting interaction forces and complementary observables in dynamic probe microscopy," *Appl. Phys. Lett.*, vol. 76, no. 9, p. 1203, 2000.
- [47] F. J. Giessibl, "A direct method to calculate tip-sample forces from frequency shifts in frequency-modulation atomic force microscopy," *Appl. Phys. Lett.*, vol. 78, no. 1, pp. 123–125, 2001.
- [48] D. Ebeling and S. D. Solares, "Bimodal atomic force microscopy driving the higher eigenmode in frequency-modulation mode: Implementation, advantages, disadvantages and comparison to the open-loop case," *Beilstein J. Nanotechnol.*, vol. 4, no. 1, pp. 198–207, 2013.
- [49] D. Kiracofe, A. Raman, and D. Yablon, "Multiple regimes of operation in bimodal AFM: Understanding the energy of cantilever eigenmodes," *Beilstein J. Nanotechnol.*, vol. 4, no. 1, pp. 385–393, 2013.
- [50] A. Labuda and P. Grütter, "Atomic force microscopy in viscous ionic liquids," *Langmuir*, vol. 28, no. 12, pp. 5319–5322, 2012.
- [51] R. W. Stark, "Dynamics of repulsive dual-frequency atomic force microscopy," *Appl. Phys. Lett.*, vol. 94, no. 6, pp. 10–13, 2009.
- [52] A. M. Gigler, C. Dietz, M. Baumann, N. F. Martinez, R. García, and R. W. Stark, "Repulsive bimodal atomic force microscopy on polymers," *Beilstein J. Nanotechnol.*, vol. 3, no. 1, pp. 456–463, 2012.

- [53] P. Thota, S. MacLaren, and H. Dankowicz, "Controlling bistability in tapping-mode atomic force microscopy using dual-frequency excitation," *Appl. Phys. Lett.*, vol. 91, no. 9, 2007.

Chapter 4

Nanomechanical characterization of homoligand and binary thiolated self-assembled monolayers on Au (111) using bimodal Atomic Force Microscopy

In this chapter the structure-properties relation of SAMs of thiols of varying length and stereochemistry is being presented. Using bimodal Atomic Force Microscopy the effective Young's modulus, E^* , of homoligand SAMs was determined. A clear relation between ligand length and E^* was found, demonstrating that bimodal AFM can be used to characterize the mechanical properties of molecularly thin, largely amorphous materials without a dominant effect from the substrate. The effect of the substrate was deconvoluted from E^* and the elasticity of the monolayers was calculated and used as the basis of a comparative study of the ordering of the deposited alkanethiol SAMs. SAMs of other thiols were markedly different from alkanethiol SAMs. Even when no topographical variation was observed, the measured elasticity revealed differences in the structure of the SAMs, allowing some conclusions regarding potential ligand ordering within these SAMs to be drawn. Bimodal AFM was further used to image binary thiol SAMs showing formation of domains smaller than 10 nm. The domains exhibited different mechanical properties, consistent with the elasticity of SAMs of the constituent ligands. The direct correlation of the surface elasticity to the topographical features allows us to localize the position of the two types of used ligands, a feat that has not been performed before.

4.1. Introduction

Organic self-assembled monolayers (SAMs) are one of the most convenient ways to modify surface properties according to particular needs and applications, without affecting the bulk of a material. SAMs of thiolated molecules on Au (111) are one of the best studied monolayer systems, as they inherently form well ordered monolayers with the ω -terminal oriented almost parallel to the surface normal via simple incubation of the substrate in a suitable ligand solution [1]–[3]. Judicious selection of the spacer chain and end functionalities of a ligand allows the deposition of SAMs with applications ranging from biomolecule sensors [4] to cell immobilization and from antifouling coatings to molecular electronics [5]. Of particular interest are binary SAMs, where a combination of two ligands can allow the controllable formation of highly tailored surfaces [6].

Despite the significant progress in the study and characterization of binary thiol SAMs, some questions still remain unanswered. The most pressing question is the localization of different ligands on a surface. Simulations and theoretical calculations have shown that binary SAMs can adopt a number of different conformations, spanning from fully mixed ligands to nanoseparated domains. Scanning tunneling microscopy (STM) studies have shown the formation of different domains in binary SAMs on flat Au(111) surfaces [7], and recent studies [8] have allowed gauging of the environment around ligand domains on nanoparticles. However, the exact chemical mapping of a surface with lateral resolution on a nanometer scale has not been achieved.

One of the most interesting and still debated aspects of SAMs is their mechanical properties. Variations in ligand length, bulkiness, rigidity and polarity significantly affect molecular ordering and packing density. Disordered SAMs should appear softer, behaving like low-density amorphous polymers. As longer ligands tend to form better-ordered, almost crystalline phases [9], resulting SAMs should theoretically appear stiffer. It is therefore hypothesized that the elasticity of organic SAMs can be used as a quality indicator, providing information on the level of molecular order and ligand packing. A technique that can spatially resolve mechanical properties of molecularly thin films with high lateral resolution (< 10 nm) could, in theory, be used as a method to chemically map a phase-separated SAM.

The first necessary step towards this approach would be establishing a characterization technique and application protocol that allows one to accurately and reproducibly characterize the nanomechanical properties of SAMs, while being sensitive to the

structural variations induced by only slight changes in ligand structure, length or bulkiness.

Experimental [10]–[14] and computational [15] studies on nanomechanical properties of alkanethiol SAMs have been performed. The elasticity of the materials was determined, but a great disparity exists amongst published results, with Young's modulus values, E , ranging from 0.18 GPa to 75 GPa. One of the most startling observations has been the general absence of correlation between ligand length, ordering and SAM elasticity. Most studies showed little or no correlation between ligand length and elasticity [13], [15], yet other studies found significant variations of E for SAMs of the same ligand [11], [12]. In their experimental work, DelRio et al. tried to address the question of ligand ordering and SAM elasticity [14]. Homoligand thiol SAMs on amorphous gold substrates were deposited and orientation and alignment of the ligands were evaluated by near edge x-ray adsorption fine structure spectroscopy (NEXAFS). Monolayer elasticity was measured by performing a series of force-distance curves with an atomic force microscope (AFM). A clear relation between ligand ordering and SAMs' Young's moduli, E , was found.

The use of force-distance curves to determine materials' mechanical properties is a standard practice in the AFM community, allowing minute control over applied loads and indentation depth. However, it is typically a very time consuming method, while little immediate correlation between mechanical and topographical features can be achieved.

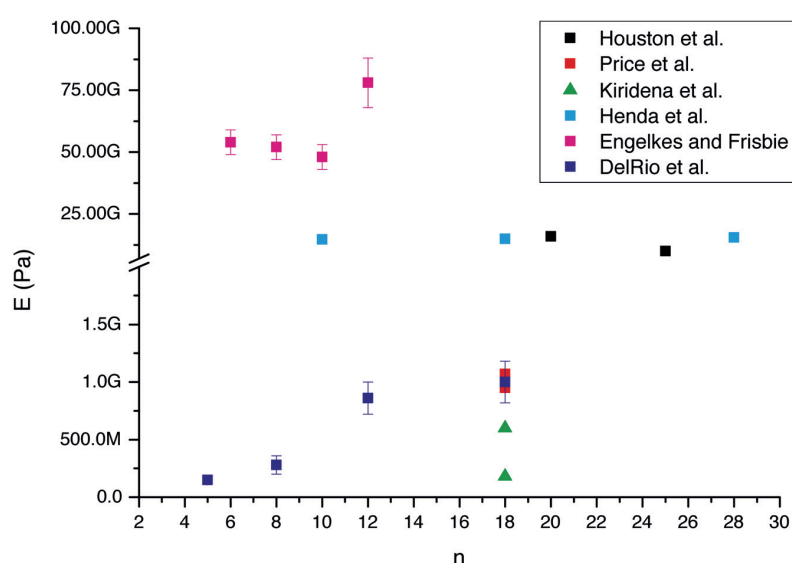


Figure 4.1: Currently available in literature [10]–[15] thiol SAMs' Young's moduli, E , vs. n , where n the number of carbons in the alkane chain.

In the present work we investigate the use of bimodal AFM for the comparative determination of surface elasticity, E^* , of surfaces covered by thiol SAMs. The technique has emerged recently as a method of probing locally and with high lateral resolution material properties, while concurrently recording surface topography. It has been used to measure variations in magnetic properties [16], as well as for the nanomechanical characterization of polymers [17], polymer blends [18] and biomolecules [19], but so far not for the characterization of molecularly thin materials. It is yet unclear whether the effect of the substrate will be too significant to differentiate between different ligand SAMs.

Bimodal AFM combines the typical high resolution of AFM with rapid, accurate and quantifiable material contrast. Bimodal AFM is a dynamic force microscopy technique, where the oscillating cantilever is excited simultaneously at two frequencies, usually the first and second eigenmodes. By introducing a complex, non-linear driving force in the movement of the cantilever, non-linear forces acting between the tip and the sample can be probed simultaneously. Moreover, the bimodal excitation signal doubles the experimental observables; the oscillation parameters of one mode, typically the first, can be used to track surface topography, while the oscillation parameters of the higher mode are used to track material properties [17], [20], [21].

4.2. Materials and Methods

The thiolated ligands used were selected based on their well-established ability to form ordered monolayers. Alkane thiols of varying length were used in order to evaluate the evolution of surface elasticity with increasing ligand length. Commercially available alkanethiols ($C_nH_{2n+2}S$), 4-cyano-1-butanethiol and mercaptosuccinic acid were purchased from Sigma-Aldrich (Sigma-Aldrich Corp., St. Louis, MO, USA) and used without further purification. Trimethylamine terminated decanethiol was synthesized in-house. Au (111) surfaces epitaxially grown on mica (thickness 200 nm) were purchased from Phasis (Geneva, Switzerland) and used without further treatment.

Table 4.1: Table of thiolated ligands, their chemical formulas and abbreviations used.

Compound name	Chemical formula	Abbreviation
1-butanethiol	C ₄ H ₁₀ S	C4
1-heptanethiol	C ₇ H ₁₆ S	C7
1-octanethiol	C ₈ H ₁₈ S	OT
1-nonanethiol	C ₉ H ₂₀ S	C9
1-undecanethiol	C ₁₁ H ₂₄ S	C11
1-dodecanethiol	C ₁₂ H ₂₆ S	C12
1-octadecanethiol	C ₁₈ H ₃₈ S	C18
Trimethylamine terminated decanethiol	C ₁₃ H ₃₀ NS	TMA
4-cyano-1-butanethiol	C ₅ H ₉ NS	CN4T
Mercaptosuccinic acid	C ₄ H ₆ O ₄ S	MSA

Alkanethiol homoligand SAMs were deposited from toluene solutions (Acros Organics, Thermo Fischer Scientific, Waltham, MA, USA). Binary OT:TMA and homoligand TMA SAMs were deposited from ethanolic solutions (Acros Organics, Thermo Fischer Scientific, Waltham, MA, USA).

Monolayer deposition took place via incubation of the surfaces in 10-15 mL of thiol solution at 60 °C for 48 h, unless otherwise specified. Solution concentration for homoligand SAMs deposition varied between 0.27 mM and 0.42 mM. SAM formation was quenched by removal of substrates from the thiol solution and rigorous rinsing in a solvent stream. Surface incubation was followed by an annealing step, during which the monolayer-covered surfaces were rinsed and incubated in 10 mL clean solvent at 60 °C for 10 d, unless otherwise specified. Upon completion of the annealing step, the surfaces were removed from the solvent, rinsed, dried in a N₂ stream and kept under vacuum in order to remove trapped solvent and avoid environmental contamination.

All AFM experiments were conducted using a commercially available Cypher S or MFP3D-Bio AFM (Asylum Research an Oxford Instruments Company, Santa Barbara, CA, USA). Bimodal AFM was performed in the net repulsive regime using the commercially available AMFM mode (Asylum Research, US patents 8,024,963, 7,937,991, 7,603,891, 7,921,466 and 7,958,563 with others pending) and all data was fitted to the Hertz model. Commercially available silicon nitride cantilevers with a first mode stiffness, k_1 , range between 1.0 and 3.5 nN/nm and fundamental resonance frequency $f_{0,1}$ = 50-90

kHz (AC240TS and AC240TSA, Olympus, Tokyo, Japan) were used. Each cantilever was individually calibrated for stiffness and sensitivity of the first mode with the Sader method (GetReal™, Asylum). Stiffness and sensitivity of the higher mode, in this case the second eigenmode, were calculated as reported in the literature [21], [22]. Probes were calibrated for tip shape and size before and after measuring each sample, as well as during each measurement, by scanning a polystyrene (PS) calibration thin film of known elasticity (Bruker Daltonics Inc., Billerica, MA, USA). Tip radius and shape were changed as to obtain the known elasticity of PS (2 GPa) for the recorded images.

Free amplitude of oscillation of the first mode was selected between 1.0 V and 2.0 V (50 nm and 100 nm respectively) and work amplitude of the first mode between 0.70-0.75 V (35-37.5 nm) and 1.4-1.45 V (70-75 nm) respectively. The work to free amplitude ratio of the first mode was always maintained between 0.68 and 0.75, as discussed in paragraph 3.5.5.2. The free amplitude of the second mode, $A_{0,2}$, was set at 100 mV (1.3-1.4 nm).

Image analysis and calculation of E^* was performed using the integrated Asylum Research software (Cypher 14.23.153 and MFP3D 14.23.153, Asylum Research), written for Igor Pro (Igor Pro 6.37, WaveMetrics, Inc., Lake Oswego, OR, U.S.A.). The operating parameters ($A_{0,1}$, A_1 , $f_{0,2}$, Δf_2) were directly loaded from every file. The spring constant for the first and second eigenmodes, as well as the tip shape and size, were manually entered, as determined by the calibration procedures described above. Multiple areas of every sample were scanned and E^* was calculated. The average of all measurements per surface was used as the average E^* of the sample. For every monolayer type samples were prepared in triplicates and measured individually. The values of E^* for every monolayer reported here represent the average of all three samples.

Static water CA measurements were carried out using the DataPhysics OCA 35 instrument with SCA20 software (DataPhysics Instruments GmbH, Filderstadt, Germany). The CA of each surface was calculated as the average of 5 drops of 5 μ L each. The CA values reported per monolayer type are the average value for three samples.

4.3. Results and Discussion

4.3.1. Contact mechanics model selection

Under the operating conditions, the tip interacts with short range repulsive forces, allowing information on the mechanical properties of the sample to be accessed [23]. An

elastic contact between the tip and sample is assumed. Conservative forces are considered dominant and non-conservative forces, such as viscoelasticity [18] and adhesion hysteresis, negligible. Experimentally, the above-mentioned assumptions were confirmed by performing a series of force-distance curves on the alkanethiol SAMs used. No SAM showed a viscoelastic response. Moreover, adhesion hysteresis was less than 10% of the applied force for all SAMs, and almost non-existent for freshly prepared samples (see Figure 4.2).

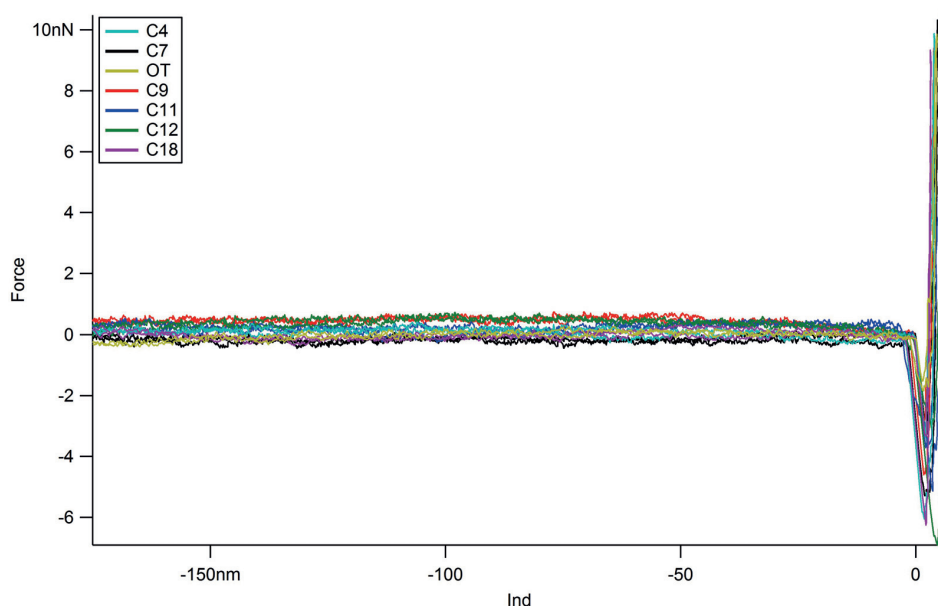


Figure 4.2: Force-indentation curves for all tested alkanethiol SAMs. No viscoelastic component can be observed.

The tip-sample interaction is modeled using the Hertz contact model. Under the operating conditions no plastic deformation of the monolayers is observed, supporting the assumption of an elastic contact. In the recorded force-distance curves an adhesive component was observed. Using the adhesion map proposed by Johnson and Greenwood [24] and the information on W_{adh} as extracted from the force curves, the elastic contact between the tip and sample can be modeled using the Hertz contact model. Contact models such as the Derjaguin-Mueller-Toporov (DMT) model do take into account adhesive forces outside the area of contact. The selection of the contact mechanics model was further confirmed by calculating the effective surface Young's moduli, E^* , of the used alkanethiol SAMs via force spectroscopy, and fitting the data with both Hertz and DMT model. The difference between the two values did not exceed 11.7% (maximum difference calculated, for freshly prepared OT SAM), while for most

SAMs it was found less than 5%. In every case, the difference of E^* between the two models was smaller than the standard deviation of the values within each model. We therefore conclude that the use of the Hertz model to describe the interaction between the tip and sample is a fair approximation and does not introduce a significant error in the calculated values.

Table 4.2: E^* for alkanethiol SAMs as determined via force-distance curves and calculated using the Hertz model (E^*_{Hertz}) and the DMT model (E^*_{DMT}). The standard deviation (σ) of values within each model is larger than the difference in E^* between the two models.

Sample	E_{Hertz} (GPa)	σ (GPa)	E_{DMT} (GPa)	σ (GPa)	Difference ($E_{\text{Hert}} - E_{\text{DMT}}$) %
C4	1.512	0.592	1.497	0.391	1.00%
C7	1.742	0.670	1.818	0.657	-4.27%
OT	1.919	0.617	1.935	0.586	-0.83%
C9	1.739	0.622	1.746	0.874	-0.40%
C11	1.304	0.294	1.347	0.249	-3.24%
C12	1.686	1.112	1.737	0.656	-2.98%
C18	2.178	0.753	1.937	0.639	11.71%

4.3.2. Comparative study of homoligand alkanethiol SAMs

Homoligand thiol SAMs have been deposited and the evolution of the effective Young's modulus of a SAM covered surface, E^* , with varying ligand length was measured. A SAM covered surface can be viewed as a composite material, with both elastic phases, the monolayer and the substrate, contributing to the overall experimentally resolved values of E^* , much like two springs in series. The contribution of the substrate is expected to be higher for surfaces covered by shorter SAMs, as reported for thin polymer films on hard substrates [25].

A clear decrease of E^* with increasing ligand length could be observed (see Figure 4.3 and Figure 4.4), even for a variation as small as the addition of one $-\text{CH}_2$ group in the alkyl spacer chain, indicating that bimodal AFM is capable of distinguishing variations in elasticity of molecularly thin soft layers on hard substrates. C4 SAMs exhibited the highest E^* , measured at $2.79 \text{ GPa} \pm 0.13 \text{ GPa}$. Alkanethiols with $7 \leq n \leq 12$ showed a significant decrease in E^* and exhibiting a small local maximum for C12. Measured values were found equal to $1.87 \text{ GPa} \pm 0.09 \text{ GPa}$ for C7, $1.80 \text{ GPa} \pm 0.11 \text{ GPa}$ for OT, $1.77 \text{ GPa} \pm$

0.29 GPa for C9, $1.75 \text{ GPa} \pm 0.19 \text{ GPa}$ for C11 and $1.93 \text{ GPa} \pm 0.06 \text{ GPa}$ for C12. E^* was minimized for C18 SAMs, the longest ligand used, and found equal to $0.96 \text{ GPa} \pm 0.07 \text{ GPa}$.

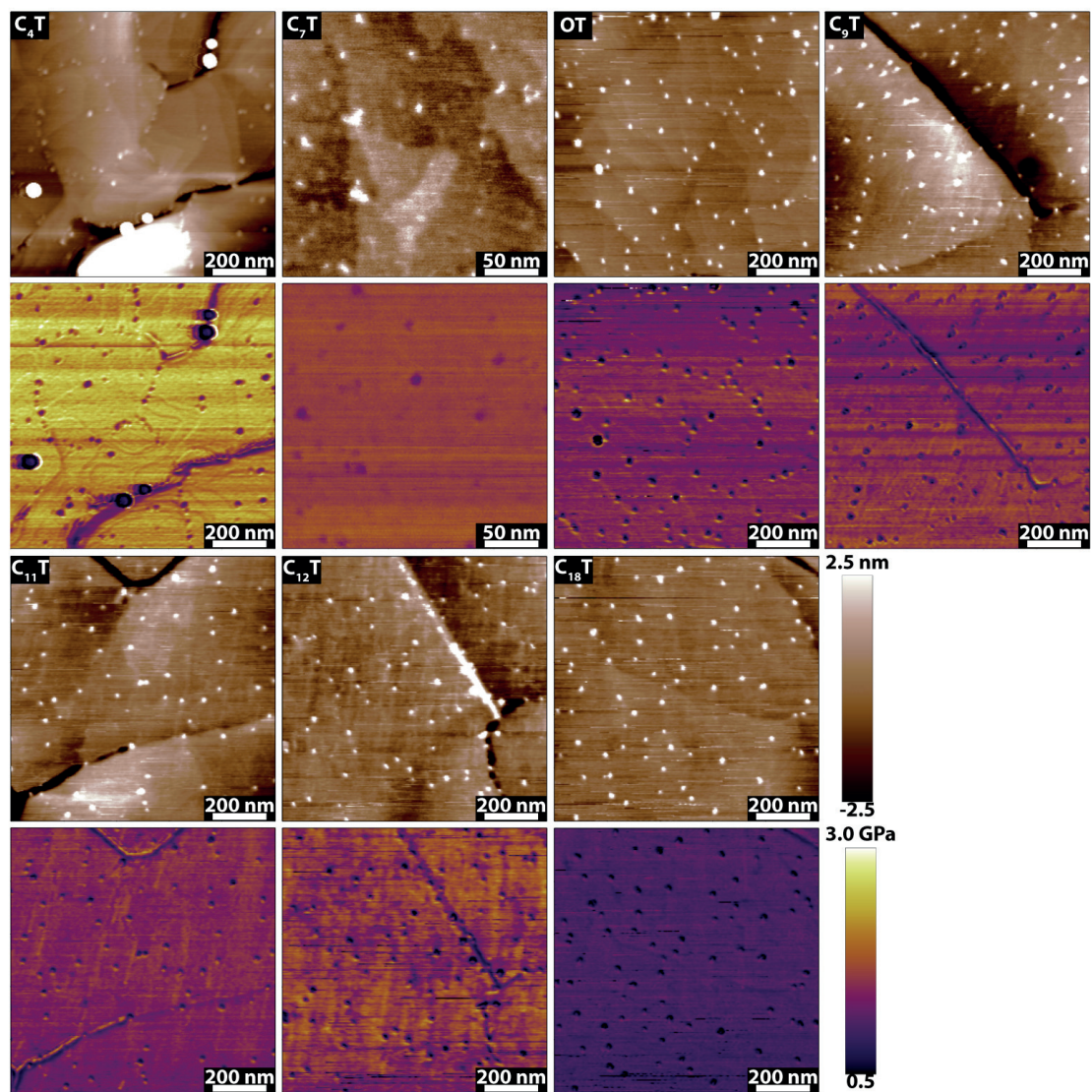


Figure 4.3: Typical morphology (brown) and simultaneously recorded corresponding E^* (yellow-purple) images for alkanethiol SAMs of increasing ligand length. The colour scales are the same for all images.

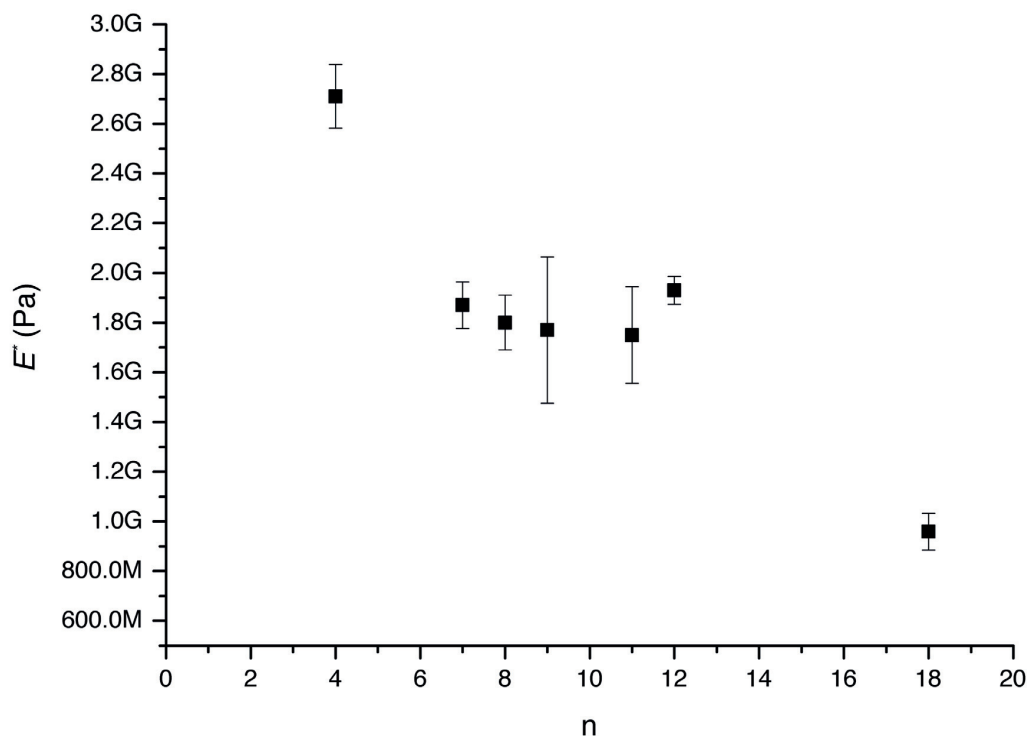


Figure 4.4: Evolution of average E^* vs. n for all tested SAMs, where n is the number of carbons in the alkane chain. The effect of the substrate appears to be more significant for shorter alkanethiol SAMs, giving rise to a higher measured E^* .

Capillary forces between the tip and the sample due to the, unavoidable in ambient conditions, presence of a thin film of water on the surfaces can affect the accuracy of the performed measurements. This effect can be experimentally observed as a “softening” of hydrophilic surfaces, as observed by Scandella et al. [26] and Kiridena et al. [12]. Indeed, by measuring the elasticity of unmodified Au (111) by bimodal AFM, E is found at approximately 700 MPa, appearing softer than the organic SAMs.

This effect could become significant particularly if extremely hydrophilic surfaces, such as unmodified gold, would be compared to hydrophobic surfaces, such as $-\text{CH}_3$ terminated SAMs.

Static contact angle (C.A.) values of all alkanethiol SAMs were measured and were found between $65.3^\circ \pm 2.4^\circ$ for C18 SAMs and $86.7^\circ \pm 2.5^\circ$ for C9 SAMs. Therefore the assumption that the capillary forces between each alkanethiol SAM and the AFM tip did not differ greatly was made.

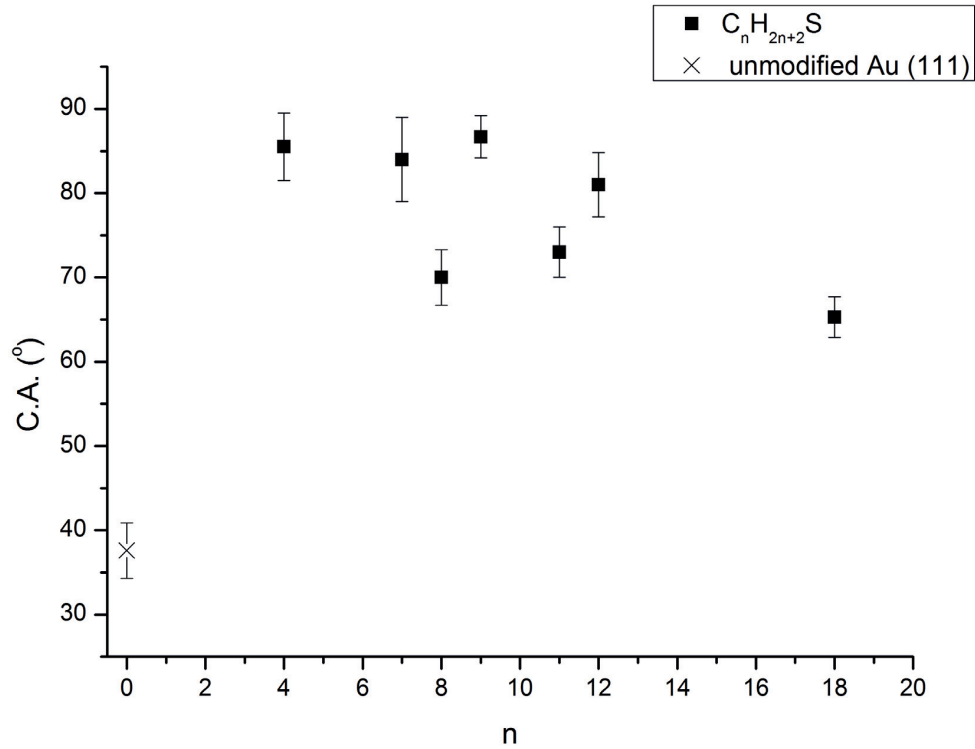


Figure 4.5: Static CA of alkanethiols vs. n , where n the number of carbons in the alkane chain, and unmodified Au (111).

The effect of the surface water layer could be screened out by performing elasticity measurements in a suitable liquid; however this is beyond the primary scope of this study, namely to establish a framework that would allow to differentiate between similar SAMs through their mechanical properties, and was thus not addressed.

4.3.3. Deconvolution of substrate-film elasticity

Having established that even small variations in ligand length lead to measureable differences in elasticity, we attempted to deconvolute the elasticity of the SAMs, E_{SAM} , from the elasticity of the monolayer-surface complex, E^* . To deconvolute the effect of substrate elasticity from the experimentally determined composite elasticity, E^* , equation 4.1 has been employed, as formulated by Xu and Pharr [27] and used by DelRio et al. [14].

$$\frac{1}{E^*} = \frac{1}{2} [1 - \nu_{sub} + (\nu_{sub} - \nu_{SAM}) I_1] \left[\frac{2(1 + \nu_{sub})}{E_{sub}} (1 - I_o) + \frac{2(1 + \nu_{SAM})}{E_{SAM}} I_o \right] \quad (4.1)$$

With ν_{sub} Poisson's ratio of the gold substrate, equal to 0.42, ν_{SAM} Poisson's ratio of the

organic SAMs, equal to 0.44, E_{sub} Young's modulus of the gold substrate, equal to 74 GPa, and I_0 and I_1 weighing functions. The weighing functions [27], as expressed in equations 4.2 and 4.3 are accounting for Poisson's ratio effects, and the ratio of monolayer thickness, t , to indenter radius, R , ξ .

$$I_1(\xi) = \frac{2}{\pi} \arctan \xi + \frac{\xi}{\pi} \ln \frac{1 + \xi^2}{\xi^2} \quad (4.2)$$

$$I_0(\xi) = \frac{2}{\pi} \arctan \xi + \frac{1}{2\pi(1 - \nu_{sub})} \left[(1 - 2\nu_{sub}) \xi \ln \frac{1 + \xi^2}{\xi^2} - \frac{\xi}{1 + \xi^2} \right] \quad (4.3)$$

Equations 4.2 and 4.3 have been rigorously calculated for a flat punch indenter. However, as the calibration step before each measurement shows, an AFM tip's geometry resembles more closely that of a sphere than a punch. In order to be able to fit our experimental data with the model of equation 4.1, a suitable correction factor must be calculated.

According to the basic Hertz theory, the force profiles for a spherical and punch indenter are given by equations 4.4 and 4.5, respectively.

$$F = \frac{4}{3} E^* \sqrt{R_{sphere}} \delta^{3/2} \quad (4.4)$$

$$F = 2R_{punch} E^* \delta \quad (4.5)$$

For a set force, F , in order to obtain the same maximum displacement, δ_{max} , the indenters of different geometries cannot have the same radius, R . An equivalent radius for a punch indenter, R_{punch}^{eq} , can be calculated as a parameter of R_{sphere} , by solving equations 4.4 and 4.5 for equal F , E^* and δ_{max} , as shown in equation 4.6.

$$R_{punch}^{eq} = \frac{2}{3} \sqrt{\delta_{max}} \sqrt{R_{sphere}} \quad (4.6)$$

R_{punch}^{eq} was calculated using the calibrated value for R for every cantilever used and the experimentally determined average δ_{max} , which under the typically employed working conditions was approximately equal to 0.5 nm.

Experimentally determined values for the thickness of the SAMs available in the literature have been used [14], [28]. For SAMs where no such values were available (C4 and C9) the maximum thickness of the monolayers was calculated by assuming a close packed configuration of fully extended chains and a 30° tilt relative to the surface normal plane.

For every SAM studied, ξ was calculated and an approximate deconvolution of the SAM elasticity, E_{SAM} , from the substrate can be attempted, as shown in Figure 4.6.

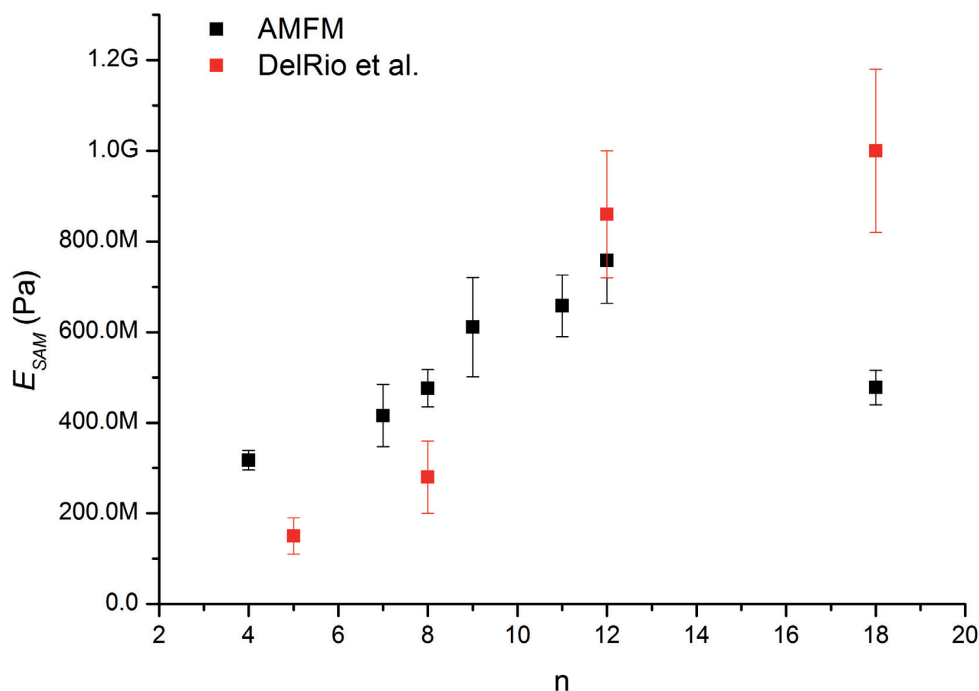


Figure 4.6: Evolution of E_{SAM} vs. n , where n the number of carbons in the alkane chain, after deconvolution of substrate-film elasticity.

The deconvoluted values for E_{SAM} can then be used to gain some information about ligand ordering within each SAM. Ligand packing density and ordering is affected by chain length and bulkiness. Alkanethiols with $n \leq 3$ tend to form more disordered SAMs, as substrate-spacer chain interatomic interactions promote a higher tilt of the molecules towards the surface and an overall disordered configuration. These interactions become less dominant with increasing ligand length ($3 < n \leq 12$) [14], as van der Waals interactions between neighboring chains promote tail alignment in an almost perpendicular to the surface orientation [29], [30]. This effect has been demonstrated to saturate for $n > 12$ for thiols [14] and for $n > 14$ for alkylphosphonic acids [31]. The additional $-\text{CH}_2$ spacer groups no longer contribute to ordering but rather can lead to a higher degree of disorder. Their larger number of possible spatial configurations can

lead to a higher concentration of gauche defects close to the SAM-environment interface. The calculated elastic behavior of SAMs can be used to give an insight into the possible degree of ordering of different SAMs. Short C4 ligands appear to lead to softer SAMs, with E_{SAM} equal to $0.32 \text{ GPa} \pm 0.02 \text{ GPa}$.

Addition of 3 $-\text{CH}_2$ groups in the spacer chain leads to a significant increase in E_{SAM} , to $0.42 \text{ GPa} \pm 0.07 \text{ GPa}$, indicating a large enhancement of ordering for C7 SAMs. Addition of one more $-\text{CH}_2$ group leads to further increase of E_{SAM} for OT SAMs, a system known to routinely yield highly ordered monolayers, to $0.48 \text{ GPa} \pm 0.04 \text{ GPa}$. E_{SAM} continues to increase upon addition of $-\text{CH}_2$ groups, with E_{SAM} equal to $0.61 \text{ GPa} \pm 0.11 \text{ GPa}$ for C9 and $0.66 \text{ GPa} \pm 0.07 \text{ GPa}$ for C11 SAMs, suggesting an additional increase in ligand ordering. E_{SAM} is maximized for C12, reaching $0.76 \text{ GPa} \pm 0.10 \text{ GPa}$, but significantly decreased for C18 SAMs, to $0.48 \text{ GPa} \pm 0.04 \text{ GPa}$. This behavior can indicate that interatomic interactions lead to a maximum degree of ordering for $n = 12$, but further increase of the ligand length does indeed introduce disorder to the system, as theoretically expected.

The general trend of E_{SAM} vs. n evolution is in reasonable agreement with the values for E_{SAM} reported by DelRio et al. The arithmetic values of E_{film} can diverge from those reported in the literature due to approximations and estimations during the fitting of the experimental data to equation 4.1, as well as differences in the experimental procedures followed.

4.3.4. Other thiols

Thiols with a structure different from the linear alkanethiols are expected to result in monolayers exhibiting varying ligand density and organization. Trimethylamine terminated decanethiol (TMA), mercaptosuccinic acid (MSA) and 4-cyano-1butanethiol (CN4T) homoligand SAMs have been deposited and characterized via bimodal AFM. TMA has a bulky headgroup, MSA is a short, bulky, branched molecule, and CN4T is a short, linear molecule with an endgroup that can coordinate with Au.

TMA SAMs appear to be composed of taller and shorter areas (see Figure 4.7). The height difference between the two corresponds to the length of a fully extended TMA molecule, 1.7nm, leading to the hypothesis that bilayer islands are formed on top of one fully formed SAM. The average E^* of the formed SAMs was measured at $1.32 \text{ GPa} \pm 0.18 \text{ GPa}$, much softer than E^* of C9 or C11 SAMs. The appearance and behavior of TMA SAMs could be explained by the formation of sparse, disorganized layers, as the bulky headgroup discourages the close packing of ligands.

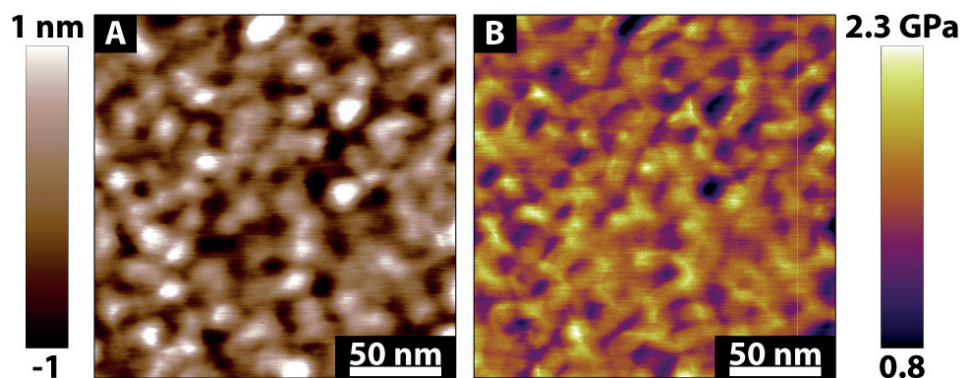


Figure 4.7 (A, B): TMA SAM, topography (A) and E^* (B). Islands of approximately 1.7 nm in height can be observed, causing a variation in E^* .

Bilayers appear also to be formed by MSA, with an average height difference from the underlying phase equal to 0.4 nm, equal to the distance between the -SH headgroup and the $^1\text{COOH}$ (see Figure 4.8). What is interesting in this case is that despite the presence of physisorbed molecules in the SAM, average surface elasticity is close to that of C4 SAMs. It is possible that the charged -COOH groups interact electrostatically with the gold substrate, providing extra stabilization in an otherwise presumably sparse monolayer. Moreover, hydrogen bonding between the exposed -COOH groups can promote the formation of more stable physisorbed islands. MSA SAMs average E^* was found equal to $2.63 \text{ GPa} \pm 0.75 \text{ GPa}$, similar to C4 SAM, exhibiting on average E^* equal to $2.71 \text{ GPa} \pm 0.13 \text{ GPa}$.

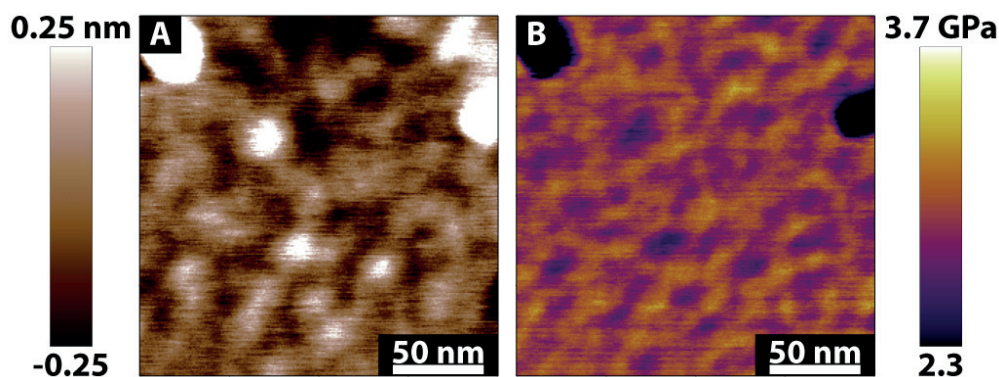


Figure 4.8 (A, B): MSA SAM, topography (A) and E^* (B). Islands of approximately 0.4 nm in height can be observed, causing a variation in E^* .

Very interesting is also the case of the cyano- terminated 4-cyano-1-butanethiol (CN4T) (see Figure 4.9). The short, linear ligands form SAMs that appear generally smooth, but are much softer than C4 SAMs, with an average E^* at $1.07 \text{ GPa} \pm 0.04 \text{ GPa}$. The formation of Au-CN complexes is a well-known reaction [32]. It is therefore hypothesized that the -CN endgroup of the ligand can coordinate with the substrate, causing the molecules to

adopt a tilted, sparse and disordered conformation, perceived as softer SAMs.

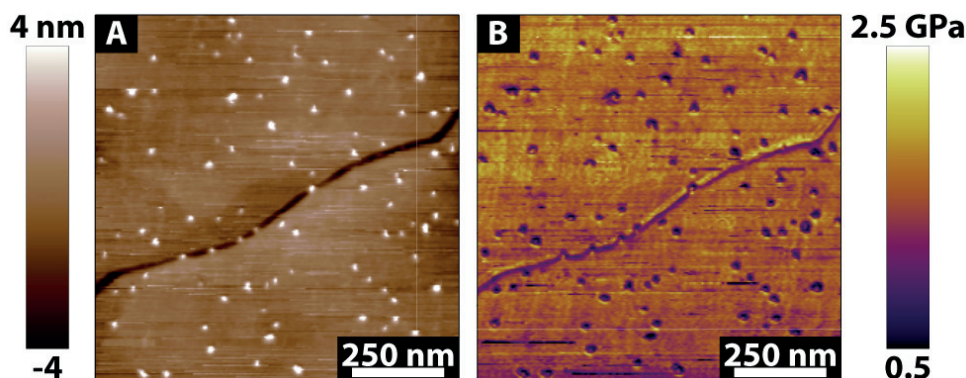


Figure 4.9 (A, B): CN4T SAM topography (A) and E^* (B). The monolayer appears smooth, topographically similar to alkanethiol SAMs. The low average E^* points to a disordered, lying-down phase.

4.3.5. Binary SAMs: Surface Chemical Recognition

Binary SAMs offer a unique freedom of surface functionalization. By a judicious selection of the end functionality of two, or more, ligands, SAMs can be tailored to a wide range of specific applications. Factors like length, bulkiness, and hydrophobicity affect the way the molecules macroscopically mix or separate into domains [7], [33]–[36]. The properties themselves of the mixed ligand SAMs can either follow the mixture rule, or, more often, be the result of interactions between individual molecules.

Bimodal AFM has been shown in paragraphs 4.3.2 and 4.3.4 to offer accurate nanomechanical characterization of surface - SAMs systems, allowing to distinguish between alkanethiols differing only in length, as well as possibly sparser or more disorganized SAMs of bulkier or charged ligands. OT:TMA mixed ligand SAMs have been formed on Au (111) using a feedstock solution ratio of 20:80. Linear sweep voltammetry of the binary SAMs showed a peak at approximately -0.93 V, between the peak of homoligand OT SAMs, at -0.91 V, and TMA, at -0.96 V (see Figure 4.10A). The presence of both molecules on the surface was further confirmed via XPS, as both N and S were detected on the surface (see Figure 4.10D, E). The surface concentration of TMA was calculated at 58%, through the ratio of bound, non-oxidized S to N, equal to S:N 3.09:1.80. STM showed the presence of domains, approximately 10 nm in the lateral dimension (see Figure 4.10B, C). The height variation between the domains, 0.6 nm, indicates the formation of an OT-rich and a TMA-rich phase.

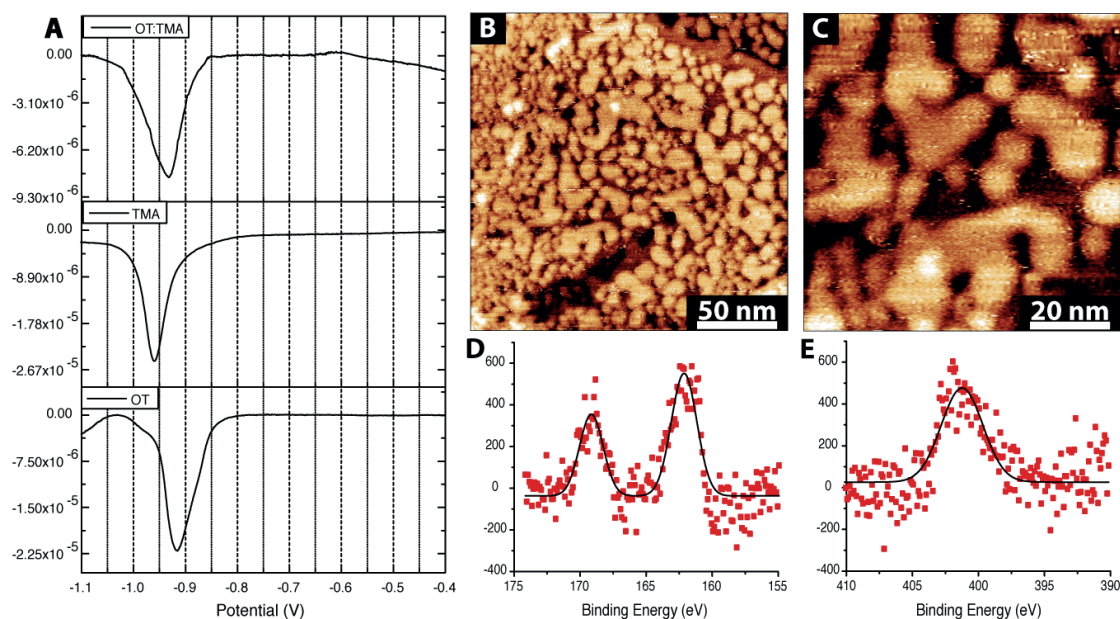


Figure 4.10 (A-E): Linear Sweep Voltammetry (A) spectra of OT, TMA homoligand SAMs and OT:TMA binary SAM, confirming the presence of both ligands in the binary SAM. STM topography (B, C) showing phase separation and domain formation. Colour scale range 0.6 nm. XPS N1s (D) and S2p (E) spectra of an OT:TMA binary SAM. The detection of both elements on the surface confirms the presence of both OT and TMA in the SAM.

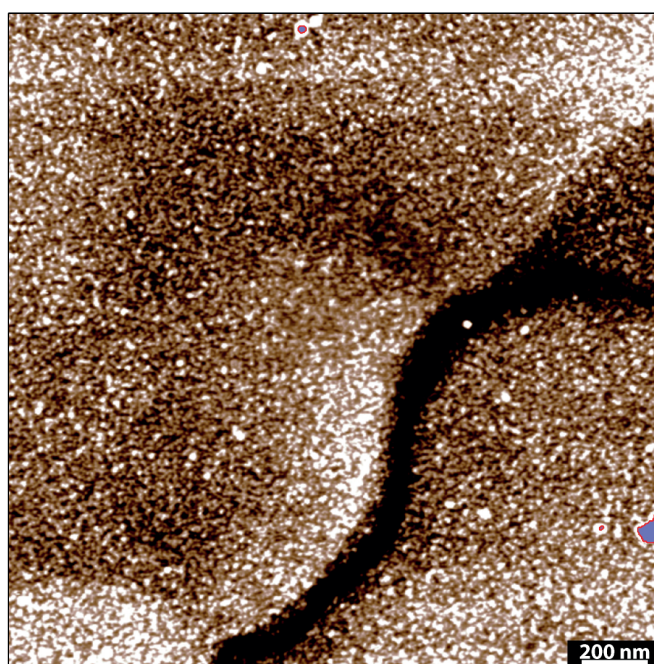


Figure 4.11: Representative topography image of OT:TMA mixed ligand SAM.

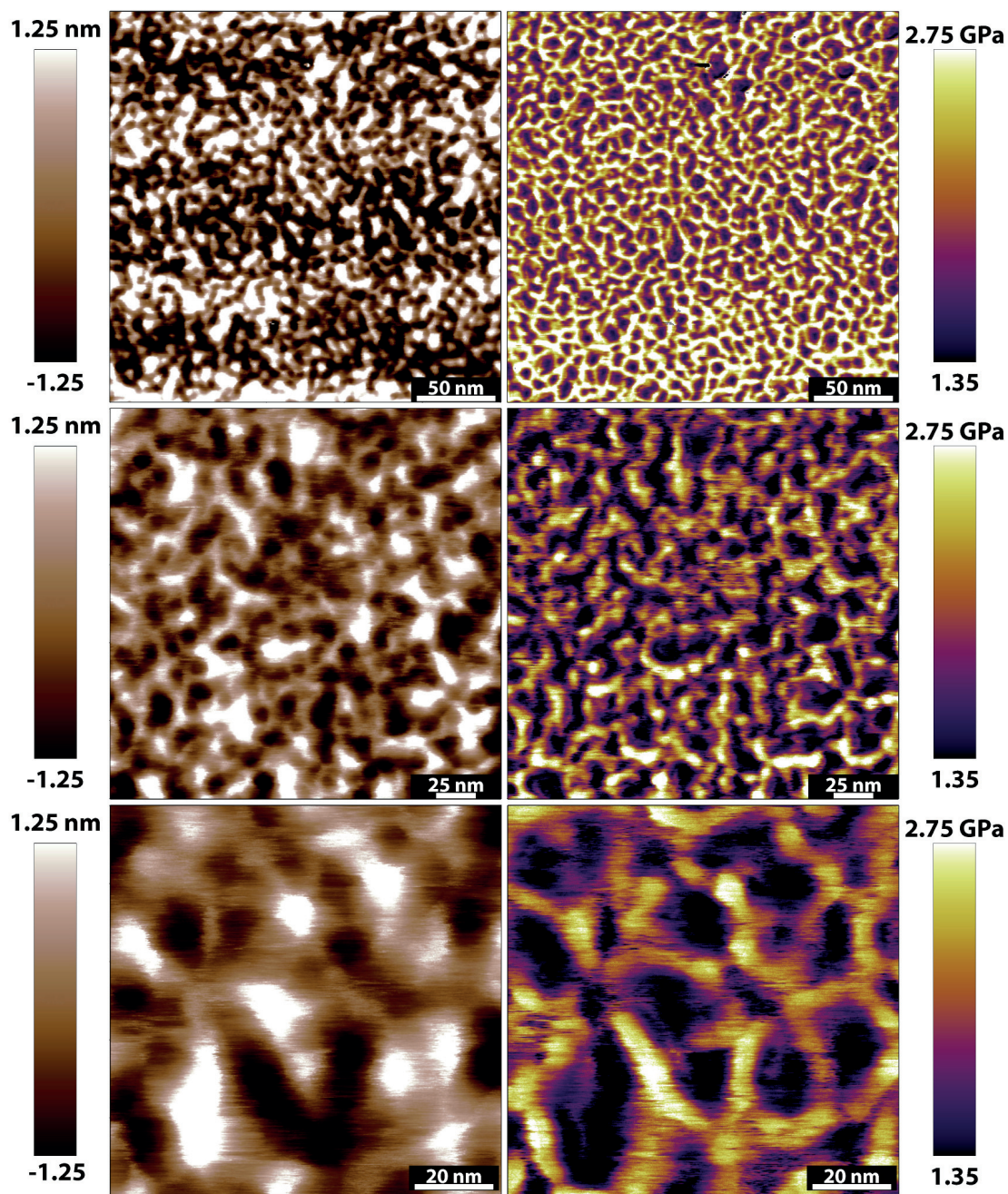


Figure 4.12: OT:TMA mixed SAMs. Different topographical characteristics show differences in E^* .

Imaging of the mixed ligand SAMs revealed domains of varying height, spread throughout the surface (see Figure 4.11). The average surface elasticity, E^* , was found equal to 1.61 ± 0.09 GPa, stiffer than pure TMA SAMs but softer than pure OT. Zooming in reveals that the observed topographical variance is accompanied by a variance in surface elasticity, E^* (see Figure 4.12). In every case, E^* exhibits a non-Gaussian distribution, which can be deconvoluted into three Gaussian peaks, as shown, for different areas and magnifications, in Figure 4.13B, Figure 4.14B and Figure 4.15B. Using

the average $E^* \pm \sigma$ of each peak as the boundary conditions, one can highlight the topographical features that exhibit the corresponding elasticity, as shown in Figure 4.13C-E, Figure 4.14C-E and Figure 4.15C-E.

Areas with the lowest E^* correspond to the highest topographical features, with a relative height close to 1 nm. Elasticity and height lead to the hypothesis that these areas are bi- or multilayers, formed possibly due to electrostatic interactions between the charged headgroup of TMA. Stiffer areas ($E^* = 1.23 \text{ GPa} \pm 0.06 \text{ GPa}$, $1.44 \text{ GPa} \pm 0.21 \text{ GPa}$ and $1.22 \text{ GPa} \pm 0.36 \text{ GPa}$ for Figure 4.13D, Figure 4.14D and Figure 4.15D respectively) correspond to areas of median relative height, at approximately 300 pm, and are ascribed to the TMA rich phase. The stiffest areas, with E^* higher than 1.97 GPa correspond to the shortest topographical features, at relative height lower than -300 pm, and are hypothesized to correspond to an OT rich phase.

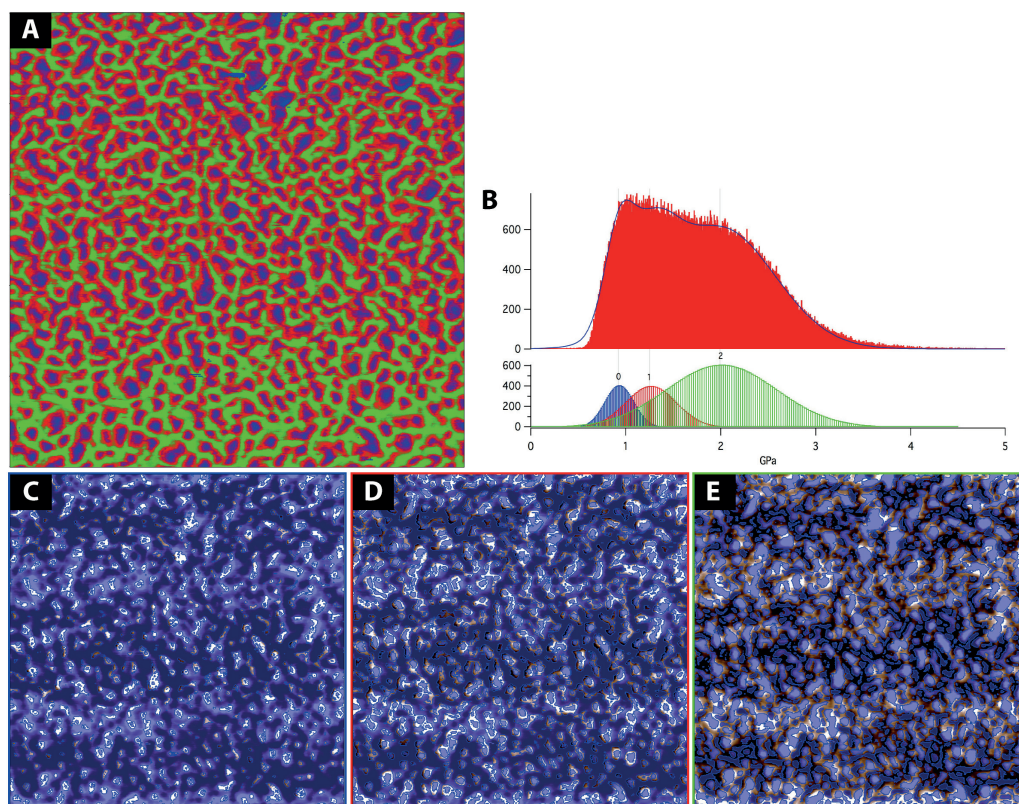


Figure 4.13: Map of surface elasticity, E^* , for an OT:TMA mixed ligand SAM (A). Distribution of E^* can be fitted with three peaks, each centered at a different value ($0.90 \text{ GPa} \pm 0.15 \text{ GPa}$, $1.23 \text{ GPa} \pm 0.26 \text{ GPa}$ and $1.97 \text{ GPa} \pm 0.58 \text{ GPa}$) (B). By thresholding at $E^* \pm \sigma$ for the three average E^* values, certain topographical features can be ascribed to each area. Features with an average $E^* = 0.90 \text{ GPa}$ appear as tall islands, and are ascribed to TMA rich multilayers (C). Features with average $E^* = 1.23 \text{ GPa}$ correspond to areas of median height, surrounding the multilayers and are ascribed to a TMA rich phase (D). Features with average $E^* = 1.97 \text{ GPa}$ correspond to the shortest areas and are ascribed to an OT rich phase (E). Blue, red and green areas of the elasticity map (A) correspond to the three peaks identified in (B). All AFM images correspond to the same area and are 500x500 nm.

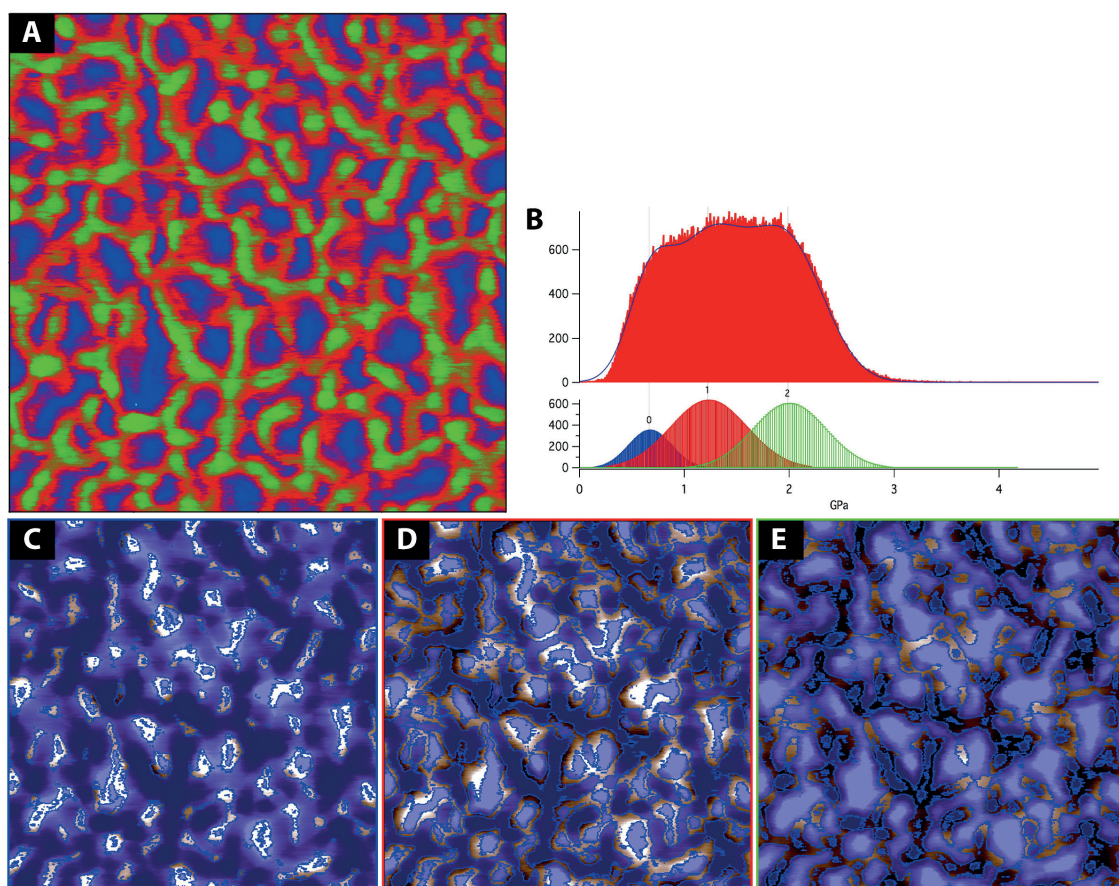


Figure 4.14: Map of surface elasticity, E^* , for an OT:TMA mixed ligand SAM (A). Distribution of E^* can be fitted with three peaks, each centered at a different value (1.07 GPa \pm 0.39 GPa, 1.44 GPa \pm 0.21 GPa and 2.04 GPa \pm 0.35 GPa) (B). By thresholding at $E^* \pm \sigma$ for the three average E^* values, certain topographical features can be ascribed to each area. Features with an average $E^* = 1.07$ GPa appear as tall islands, and are ascribed to TMA rich multilayers (C). Features with average $E^* = 1.44$ GPa correspond to areas of median height, surrounding the multilayers and are ascribed to a TMA rich phase (D). Features with average $E^* = 2.04$ GPa correspond to the shortest areas and are ascribed to an OT rich phase (E). Blue, red and green areas of the elasticity map (A) correspond to the three peaks identified in (B). All AFM images correspond to the same area and are 200x200 nm.

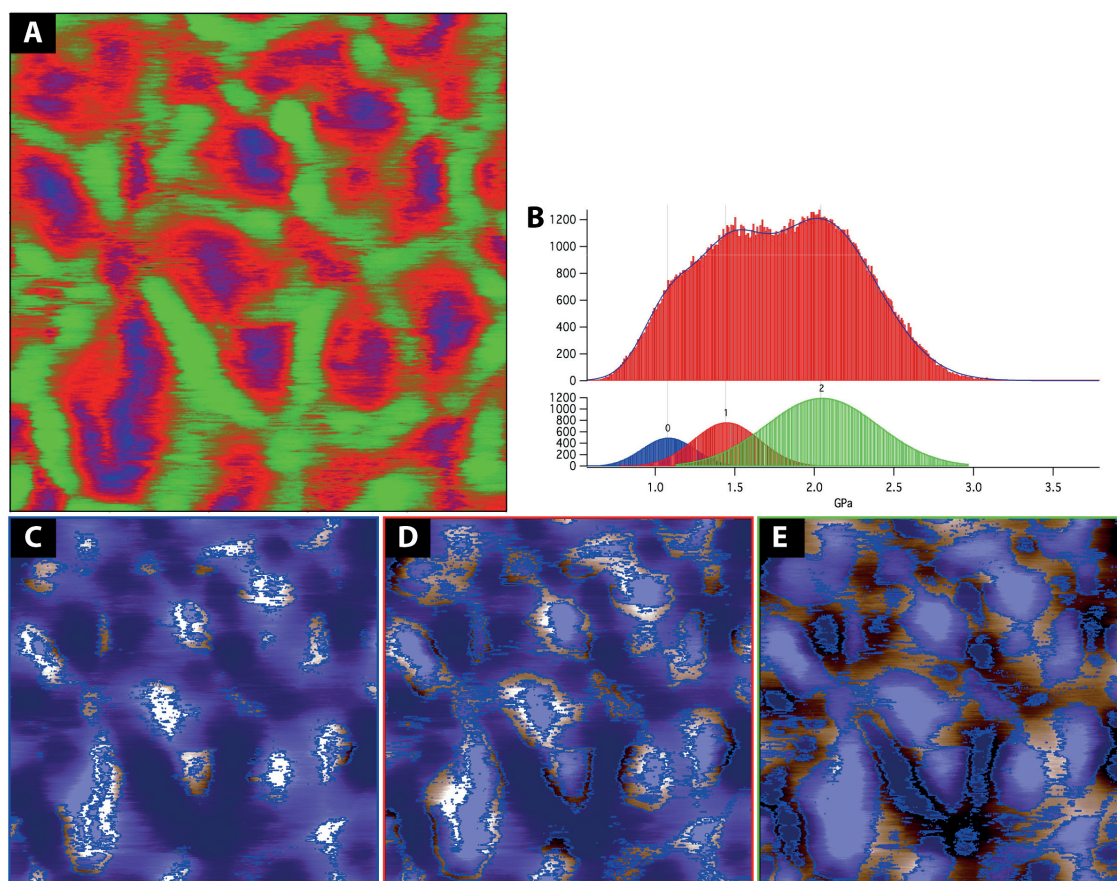


Figure 4.15: Map of surface elasticity, E^* , for an OT:TMA mixed ligand SAM (A). Distribution of E^* can be fitted with three peaks, each centered at a different value ($0.66 \text{ GPa} \pm 0.20 \text{ GPa}$, $1.22 \text{ GPa} \pm 0.36 \text{ GPa}$ and $1.99 \text{ GPa} \pm 0.35 \text{ GPa}$) (B). By thresholding at $E^* \pm \sigma$ for the three average E^* values, certain topographical features can be ascribed to each area. Features with an average $E^* = 0.664 \text{ GPa}$ appear as tall islands, and are ascribed to TMA rich multilayers (C). Features with average $E^* = 1.22 \text{ GPa}$ correspond to areas of median height, surrounding the multilayers and are ascribed to a TMA rich phase (D). Features with average $E^* = 1.99 \text{ GPa}$ correspond to the shortest areas and are ascribed to an OT rich phase (E). Blue, red and green areas of the elasticity map (A) correspond to the three peaks identified in (B). All AFM images correspond to the same area and are $100 \times 100 \text{ nm}$.

Apart from the localization of the different chemical species on the surface at high lateral resolution, via their mechanical properties, the area of each peak can be used to estimate the chemical composition of the SAM. 11.78% of the total area corresponds to a multilayer, 19.95% to a TMA rich phase and 68.27% to an OT rich phase.

4.4. Conclusions

We have demonstrated the capability of bimodal AFM to accurately measure the surface elasticity of SAM-covered surfaces, without a dominant effect from the substrate. We have been able to determine the mechanical properties of SAMs made of chemically

similar ligands but with varying length, distinguishing the induced change of E^* caused by only a few $-\text{CH}_2$ groups.

SAM elasticity can be approximately deconvoluted from substrate elasticity and some information regarding ligand ordering within each SAM can be gained. Even though the obtained results are in good agreement with those reported in the literature [14], a number of approximations and assumptions was made. Further work needs to be carried out for the derivation of a rigorous model if the determination of elasticity of only the SAMs is the research question.

Furthermore, we have been able to use bimodal AFM to measure the local variation of mechanical properties and directly correlate these to topographical features, allowing the identification of chemically different domains in the 5 - 10 nm range. This approach addresses one of the most pertinent questions of binary SAMs formation, namely the arrangement of the two ligands on a flat surface.

All measurements were carried out in ambient conditions using commercially available AFMs and cantilevers. Without needing synchrotron radiation, ultra high vacuum conditions or a sophisticated set up, we were able to detect small local variations in elasticity and use these to map the chemical composition of organic surfaces.

4.5. References

- [1] A. Ulman, "Formation and structure of self-assembled monolayers,," *Chem. Rev.*, vol. 96, no. 4, pp. 1533–1554, 1996.
- [2] A. Ulman, J. F. Kang, Y. Shnidman, S. Liao, R. Jordan, G. Y. Choi, J. Zaccaro, a. S. Myerson, M. Rafailovich, J. Sokolov, and C. Fleischer, "Self-assembled monolayers of rigid thiols," *J. Biotechnol.*, vol. 74, no. 3, pp. 175–188, 2000.
- [3] A. Ulman, *An introduction to ultrathin organic films: From Langmuir-Blodgett to self-assembly*, 1st ed. Boston: Academic Press, 1991.
- [4] V. Spampinato, M. A. Parracino, R. La Spina, F. Rossi, and G. Ceccone, "Surface analysis of gold nanoparticles functionalized with thiol-modified glucose SAMs for biosensor applications," *Front. Chem.*, vol. 4, pp. 1–12, 2016.
- [5] S. Casalini, C. A. Bortolotti, F. Leonardi, and F. Biscarini, "Self-assembled monolayers in organic electronics," *Chem. Soc. Rev.*, vol. 46, no. 1, pp. 40–71, 2017.
- [6] Q. Ong, Z. Luo, and F. Stellacci, "Characterization of ligand shell for mixed-ligand coated gold nanoparticles," *Acc. Chem. Res.*, vol. 50, no. 8, pp. 1911–1919, 2017.
- [7] R. Smith and S. Reed, "Phase separation within a binary self-assembled monolayer on Au {111} driven by an amide-containing alkanethiol," *J. Phys. Chem.*, vol. 105, no. 6, pp. 1119–1122, 2001.
- [8] Z. Luo, J. Hou, L. Menin, Q. K. Ong, and F. Stellacci, "Evolution of the ligand shell morphology during ligand exchange reactions on gold nanoparticles," *Angew. Chemie Int. Ed.*, vol. 56, no. 43, pp. 1–6, 2017.
- [9] A. Khassanov, H. G. Steinrück, T. Schmaltz, A. Magerl, and M. Halik, "Structural investigations of self-assembled monolayers for organic electronics: Results from X-ray reflectivity," *Acc. Chem. Res.*, vol. 48, no. 7, pp. 1901–1908, 2015.
- [10] V. B. Engelkes and C. Daniel Frisbie, "Simultaneous nanoindentation and electron tunneling through alkanethiol self-assembled monolayers," *J. Phys. Chem. B*, vol. 110, no. 20, pp. 10011–10020, 2006.
- [11] W. J. Price, S. A. Leigh, S. M. Hsu, T. E. Patten, and G. Y. Liu, "Measuring the size dependence of young's modulus using force modulation atomic force microscopy," *J. Phys. Chem. A*, vol. 110, no. 4, pp. 1382–1388, 2006.
- [12] W. Kiridena, V. Jain, P. K. Kuo, and G. Liu, "Nanometer-scale elasticity measurements on organic monolayers using scanning force microscopy," *Surf. Interface Anal.*, vol. 25, no. 6, pp. 383–389, 1997.
- [13] J. E. Houston and H. I. Kim, "Adhesion, friction, and mechanical properties of

- functionalized alkanethiol self-assembled monolayers," *Acc. Chem. Res.*, vol. 35, no. 7, pp. 547–553, 2002.
- [14] F. W. Delrio, C. Jaye, D. A. Fischer, and R. F. Cook, "Elastic and adhesive properties of alkanethiol self-assembled monolayers on gold," *Appl. Phys. Lett.*, vol. 94, no. 13, pp. 10–13, 2009.
- [15] R. Henda, M. Grunze, and A. J. Pertsin, "Static energy calculations of stress-strain behavior of self-assembled monolayers," *Tribol. Lett.*, vol. 5, pp. 191–195, 1998.
- [16] J. W. Li, J. P. Cleveland, and R. Proksch, "Bimodal magnetic force microscopy: Separation of short and long range forces," *Appl. Phys. Lett.*, vol. 94, no. 16, pp. 2007–2010, 2009.
- [17] R. Garcia and R. Proksch, "Nanomechanical mapping of soft matter by bimodal force microscopy," *Eur. Polym. J.*, vol. 49, no. 8, pp. 1897–1906, 2013.
- [18] E. T. Herruzo, A. P. Perrino, and R. Garcia, "Fast nanomechanical spectroscopy of soft matter," *Nat. Commun.*, vol. 5, p. 3126, 2014.
- [19] D. Martinez-Martin, E. T. Herruzo, C. Dietz, J. Gomez-Herrero, and R. Garcia, "Noninvasive protein structural flexibility mapping by bimodal dynamic force microscopy," *Phys. Rev. Lett.*, vol. 106, no. 19, pp. 1–4, 2011.
- [20] J. R. Lozano and R. Garcia, "Theory of phase spectroscopy in bimodal atomic force microscopy," *Phys. Rev. B - Condens. Matter Mater. Phys.*, vol. 79, no. 1, pp. 1–9, 2009.
- [21] R. Garcia and E. T. Herruzo, "The emergence of multifrequency force microscopy," *Nat. Nanotechnol.*, vol. 7, no. 4, pp. 217–226, 2012.
- [22] A. Labuda, M. Kocun, T. Walsh, J. Meinhold, T. Proksch, W. Meinhold, and R. Proksch, "Calibration of higher eigenmodes of cantilevers," *Rev. Sci. Instrum.*, vol. 87, no. 73705, pp. 1–11, 2016.
- [23] R. Proksch, "Multifrequency, repulsive-mode amplitude-modulated atomic force microscopy," *Appl. Phys. Lett.*, vol. 89, no. 11, pp. 1–4, 2006.
- [24] K. L. Johnson and J. A. Greenwood, "An adhesion map for the contact of elastic spheres," *J. Colloid Interface Sci.*, vol. 192, no. 2, pp. 326–333, 1997.
- [25] A. Abdel-Mohti, A. N. Garbash, S. Almagahwi, and H. Shen, "Effect of layer and film thickness and temperature on the mechanical property of micro- and nano-layered PC/PMMA films subjected to thermal aging," *Materials (Basel)*, vol. 8, no. 5, pp. 2062–2075, 2015.
- [26] L. Scandella, A. Schumacher, N. Kruse, R. Prins, E. Meyer, R. Lüthi, L. Howald, and

- H. J. Güntherodt, "Tribology of ultra-thin MoS₂ platelets on mica: studies by scanning force microscopy," *Thin Solid Films*, vol. 240, no. 1–2, pp. 101–104, 1994.
- [27] H. Xu and G. M. Pharr, "An improved relation for the effective elastic compliance of a film/substrate system during indentation by a flat cylindrical punch," *Scr. Mater.*, vol. 55, no. 4, pp. 315–318, 2006.
- [28] J. P. Folkers, P. E. Laibinis, and G. M. Whitesides, "Self-assembled monolayers of alkanethiols on gold: Comparisons of monolayers containing mixtures of short- and long-chain constituents with CH₃ and CH₂OH terminal groups," *Langmuir*, vol. 8, no. 5, pp. 1330–1341, 1992.
- [29] N. J. Brewer, B. D. Beake, and G. J. Leggett, "Friction force microscopy of self-assembled monolayers: Influence of adsorbate alkyl chain length, terminal group chemistry, and scan velocity," *Langmuir*, vol. 17, no. 6, pp. 1970–1974, 2001.
- [30] G. E. Poirier and E. D. Pylant, "The self-assembly mechanism of alkanethiols on Au(111)," *Science (80-.)*, vol. 272, no. 5265, pp. 1145–1148, 1996.
- [31] K. Fukuda, T. Hamamoto, T. Yokota, T. Sekitani, U. Zschieschang, H. Klauk, and T. Someya, "Effects of the alkyl chain length in phosphonic acid self-assembled monolayer gate dielectrics on the performance and stability of low-voltage organic thin-film transistors," *Appl. Phys. Lett.*, vol. 95, no. 20, pp. 203301–3, 2009.
- [32] W. P. Griffith, "Cyanide complexes of the transition metals," *Q. Rev. Chem. Soc.*, vol. 16, p. 188, 1962.
- [33] G. a. DeVries, F. R. Talley, R. P. Carney, and F. Stellacci, "Thermodynamic study of the reactivity of the two topological point defects present in mixed self-assembled monolayers on gold nanoparticles," *Adv. Mater.*, vol. 20, no. 22, pp. 4243–4247, Nov. 2008.
- [34] R. P. Carney, G. A. DeVries, C. Dubois, H. Kim, J. Y. Kim, C. Singh, P. K. Ghorai, J. B. Tracy, R. L. Stiles, R. W. Murray, S. C. Glotzer, and F. Stellacci, "Size Limitations for the Formation of Ordered Striped Nanoparticles," *J. Am. Chem. Soc.*, vol. 130, no. 3, pp. 798–799, 2007.
- [35] J. P. Folkers, P. E. Laibinis, G. M. Whitesides, and J. Deutch, "Phase behavior of two-component self-assembled monolayers of alkanethiolates on gold," *J. Phys. Chem.*, vol. 98, pp. 563–571, 1994.
- [36] L. A. Bumm, J. J. Arnold, L. F. Charles, T. D. Dunbar, D. L. Allara, and P. S. Weiss, "Directed self-assembly to create molecular terraces with molecularly sharp boundaries in organic monolayers," *J. Am. Chem. Soc.*, vol. 121, no. 35, pp. 8017–

8021, 1999.

Chapter 5

Kinetic study of the formation of octadecylphosphonic acid self-assembled monolayers on Al_2O_3 and the characteristics thereof

Phosphonic acid SAMs provide an attractive surface modification method for Al_2O_3 surfaces. In this chapter the effect of monolayer formation time (t_M) in the structure and properties of octadecylphosphonic acid (ODPA) SAMs is discussed. The main experimental technique is bimodal AFM. The conducted kinetic study, as described in paragraph 5.3, has revealed that the monolayer formation process can be divided into three consecutive steps: initial rapid adsorption and formation of a disordered submonolayer, slower ligand uptake and ordering to create a well ordered monolayer, and multilayer formation. Each time point is characterized by formations of distinct degrees of ordering, wettability, morphology and elasticity.

5.1. Introduction

Phosphonic acids can readily bind to any hydroxylated surface, such as the surfaces of metal oxides, producing well-ordered self-assembled monolayers (SAMs) [1], [2]. One of the preferred substrates for alkylphosphonic acid SAM formation, due to its high technological importance, is Al_2O_3 . These SAMs have been used as dielectrics in organic electronics [3]–[5] and shells in Al_2O_3 nanoparticles sensors [6], [7].

Numerous studies have focused on the mode of bonding between the $-\text{PO}(\text{OH})_2$ headgroup and the surface of Al_2O_3 . The general consensus is that phosphonic acids can bind on a hydroxylated surface through simple condensation reactions, forming mono-, bi- or tridentate bonds [8]–[10]. Even though all bond types are energetically possible, steric considerations, in particular regarding the accessibility of binding sites by a partially bound headgroup, can inhibit tridentate binding [8], [11]–[13]. Regardless of the number of bonds formed though, the P-O-Al bonds are in general stable and in contrast to the well-known S-Au species, do not exhibit any in-plane mobility; rather, ligands remain at the binding site where they first adsorbed.

Both theoretical and experimental studies have also addressed the question of ligand density and ordering within a phosphonic acid SAM on Al_2O_3 . Lushtinetz et al. calculated, using the self-consistent-charge density-functional based tight-binding (SCC-DFTB) method, that the maximum ligand density on an amorphous surface is approximately 4.3–4.7 molecules/ nm^2 [14]. Ligand ordering in phosphonic acid SAMs on metal oxides has been experimentally and theoretically investigated and found to exhibit a dependence on ligand length [14]–[18]. Alkylphosphonic acids with fewer than 10 carbons tend to form more disordered SAMs. The addition of $-\text{CH}_2$ groups in the spacer chain enhances ligand ordering via intermolecular van der Waals interactions, effect believed to saturate for chains with 14 C. The addition of further $-\text{CH}_2$ groups is believed to introduce *gauche* defects in the upper part of the SAM.

Despite the significant progress in the study of phosphonic acid SAMs, there is still a great disparity in the available literature regarding the state of the formed SAMs and their properties for varying monolayer formation times. While some groups report the formation of full monolayers in a set time period [18]–[20], others report the formation of multilayers [21]–[23]. At the same time, there is little available information regarding the mechanical properties of these SAMs.

Given that the mechanical properties can give valuable information regarding the ordering and arrangement of molecules within a SAM, as discussed in Chapter 4, we

believe that their determination can provide information on the configuration of ligands for varying monolayer formation times. In this study we deposit ODPA SAMs on amorphous Al_2O_3 . SAM deposition was quenched at varying time points, called monolayer formation time, t_M . For every t_M the chemical and elastic behavior, as well as wettability, of the resulting organic layer was studied. By using a commercially available setup, bimodal AFM [24], [25] imaging of all samples was carried out and the evolution of surface elasticity, E^* , in conjunction with surface topography was monitored.

The obtained results indicated that the same molecule does not adopt a rigid configuration from the moment of adsorption; rather SAM formation passes through a number of steps, as an effect of ligand surface concentration and binding mode. It is hypothesized that ODPA SAMs initially form disordered, lying-down phases, which gradually evolve to better ordered standing-up phases, even at low ligand uptake rate. The formation of islands or complete bi- and multilayers on top of a well-ordered ODPA SAM was observed. Every chemisorbed and physisorbed formation exhibited different mechanical properties.

The obtained data of surface ligand concentration have also been fitted to a suitable adsorption model, and two distinct steps regarding adsorption rate were determined.

Moreover, phosphonic acid SAMs were deposited on industrial aluminium alloys of the line 6xxx, and they were imaged via bimodal AFM. E^* was found to vary between different alloys and the recorded values are in the good agreement with those established from the study of ODPA SAMs on smooth, stable Al_2O_3 surfaces. Here it is demonstrated that bimodal AFM can provide accurate nanomechanical description of organic SAMs grown on a number of different substrates, including extremely rough industrial surfaces. Under this light, the use of bimodal AFM as a rapid and robust technique for the characterization and quality control of industrial products is proposed.

5.2. Materials and methods

TiO_2 (110) surfaces with surface roughness less than 0.1 nm were purchased from CrysTec GmbH. Amorphous Al_2O_3 was deposited on top via Atomic Layer Deposition (ALD). The end roughness of the surface remained less than 0.3 nm. Surfaces were activated prior to SAM deposition via O_2 plasma etching for 5 min.

Octadecylphosphonic acid (ODPA) was purchased from Sigma-Aldrich (Sigma-Aldrich Corp., St. Louis, MO, USA) and used without further purification. SAMs were formed via surface incubation in 1 mM ethanolic solutions for the specified t_M (Acros Organics, Thermo Fischer Scientific, Waltham, MA, USA). SAM formation was quenched by

removal of the samples from the ligand solution and rigorous solvent rinsing. The monolayers were dried and kept in vials fluxed with an inert gas (Ar or N₂) until used.

X-Ray Photoelectron Spectroscopy (XPS) measurements were carried out using a PHI VersaProbe II scanning XPS microprobe (Physical Instruments AG, Germany). Analysis was performed using a monochromatic Al K α X-ray source of 24.8 W power with a beam size of 100 μ m. The spherical capacitor analyzer was set at 45° take-off angle with respect to the sample surface. The pass energy was 46.95 eV yielding a full width at half maximum of 0.91 eV for the Ag 3d 5/2 peak. For all measurements the binding energy scale was normalized to the position of the -CH₃ group (284.8 eV). Curve fitting and data analysis was performed using the PHI Multipak software. The reported XPS values are the average value for three samples.

Static water contact angle (CA) measurements were carried out using the DataPhysics OCA 35 instrument with SCA20 software (DataPhysics Instruments GmbH, Filderstadt, Germany). The CA of each surface was calculated as the average of 5 drops of 5 μ L each. The CA values reported per time point, t_m , are the average value for three samples.

All AFM experiments were conducted using a commercially available Cypher S or MFP3D-Bio AFM (Asylum Research an Oxford Instruments Company, Santa Barbara, CA, USA). Bimodal AFM was performed using the commercially available AMFM mode (Asylum Research, US patents 8,024,963, 7,937,991, 7,603,891, 7,921,466 and 7,958,563 with others pending) and all data was fitted to the Hertz model. Commercially available silicon nitride cantilevers with a first mode stiffness, k_1 , range between 1.0 and 3.5 nN/nm and fundamental resonance frequency $f_{0,1}$ = 50-90 kHz (AC240TS and AC240TSA, Olympus, Tokyo, Japan) were used. Each cantilever was individually calibrated for stiffness and sensitivity of the first mode with the Sader method (GetReal™, Asylum Research). Stiffness and sensitivity of the higher mode, in this case the second eigenmode, were calculated as reported in the literature [25], [26]. Probes were calibrated for tip shape and size before and after measuring each sample, as well as during each measurement, by scanning a polystyrene (PS) calibration thin film of known elasticity (Bruker Daltonics Inc., Billerica, MA, USA). Tip radius and shape of the tip were changed as to obtain the known elasticity of PS (2 GPa) for the recorded images. Free amplitude of oscillation of the first mode was selected between 1.0 V (50 nm) and 2.0 V (100 nm) and work amplitude of the first mode between 0.70-0.75 V (35 - 37.5 nm) and 1.4-1.45 V (70-75 nm) respectively. The work to free amplitude ratio of the first

mode was always maintained between 0.68 and 0.75, as discussed in paragraph 3.4.5.2. The free amplitude of the second mode, $A_{0,2}$, was set at 100 mV (1.2-1.4 nm). Image analysis and calculation of E^* was performed using the integrated Asylum Research software (Cypher14.23.153 and MFP3D 14.23.153, Asylum Research), written for Igor Pro (Igor Pro 6.37, WaveMetrics, Inc., Lake Oswego, OR, U.S.A.). The operating parameters ($A_{0,1}$, A_1 , $f_{0,2}$, Δf_2) were directly loaded from every file. The spring constant for the first and second eigenmodes, as well as the tip shape and size, were manually entered, as determined by the calibration procedures described above. Multiple areas of every sample were scanned and E^* was calculated. The average of all measurements per surface was used as the average E^* of the sample. For every monolayer formation time samples were prepared in triplicates and measured individually. The values of E^* for every t_M reported here represent the average of all three samples.

5.3. Results and Discussion

5.3.1. ODPa SAMs on flat Al_2O_3

Monolayer formation was monitored *ex situ* via surface atomic concentration of P as determined by XPS (see Figure 5.1). An initial rapid adsorption followed by a plateau can be observed. The rapid adsorption can be explained by the almost immediate adsorption of ligand molecules on the activated surface, in a sparse and possibly disordered or physisorbed configuration. As time progresses, more ligand molecules can chemisorb to the surface, filling in free binding sites until eventually most accessible binding sites have been occupied by chemisorbed ODPa molecules. For $t_M \geq 6$ h a second significant increase in surface P% was observed, possibly due to ligand physisorption on top of the already formed monolayer. The evolution of ODPa SAMs can then be described as a three-step process, involving initial physisorption and sparse submonolayer formation, monolayer formation and ordering and bi- or multilayer formation.

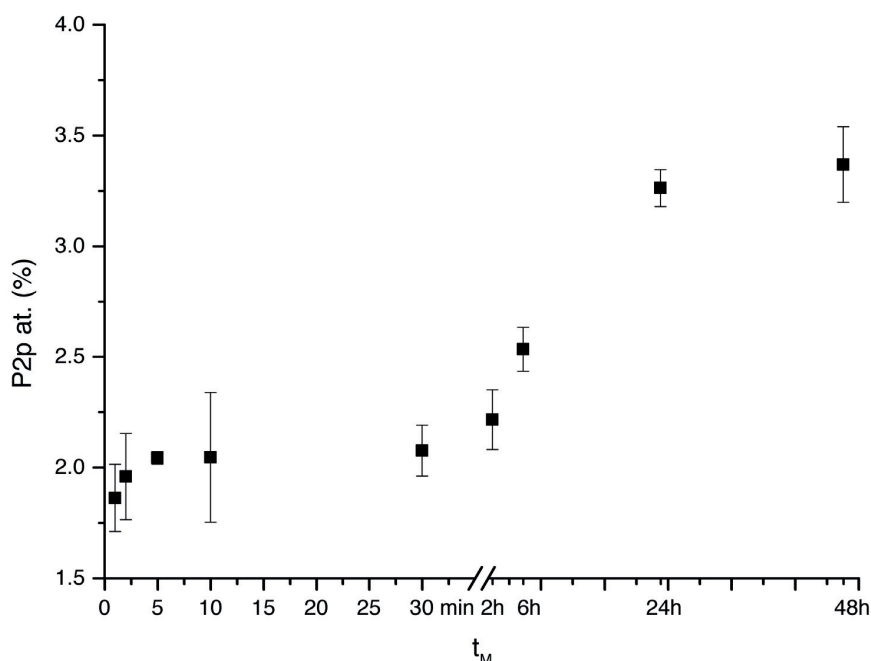


Figure 5.1: Evolution of surface atomic concentration of P for ODPA SAMs deposited at increasing t_M as determined via XPS.

The O1s peak has been deconvoluted to peaks corresponding to three chemical species that could reasonably exist on the surface of the samples: one at 531 eV, corresponding to Al-O-P, one at 532 eV, corresponding to free P-OH and Al-O from the Al_2O_3 and one at 534 eV, corresponding to free P=O [27] (see Appendix B, Figure B.11). By calculating the intensity ratio of the third to the first peak we can estimate the relative density of free P=O to bound Al-O-P. Keeping in mind the mono-, bi- and tridentate mode of bond formation between a $-PO(OH)_2$ headgroup and the Al_2O_3 surface, the evolution of the relative intensity over time can indicate the bonding mode at each t_M tested (see Figure 5.2). The ratio at $t_M = 1$ min was calculated at 0.016 ± 0.004 , and varied little up to, and including, $t_M = 30$ min, when it was found equal to 0.018 ± 0.005 . This behavior can be attributed to an initially very sparse monolayer, where the ligand molecules encounter no steric hindrance from the neighboring molecules and can thus bond to all accessible binding sites, allowing for tridentate bonding. At the same time, ligand density is increasing as more molecules are being added, thus not allowing for a minimization of unconsumed P=O. At $t_M = 2$ h the calculated average P=O:Al-O-P intensity ratio appeared to decrease further, reaching 0.012 ± 0.005 , indicating that addition of new ligands was decelerated, the density of tridentate bound molecules was highest than at any other time point, and the SAM can be assumed to adopt a well-ordered configuration. At

higher t_M the relative intensity increased significantly, to a maximum value of 0.091 ± 0.028 at $t_M = 48h$, indicating a plethora of free $P=O$, attributed either to the addition of few molecules into free, yet confined, binding sites, or the onset and evolution of multilayer formation.

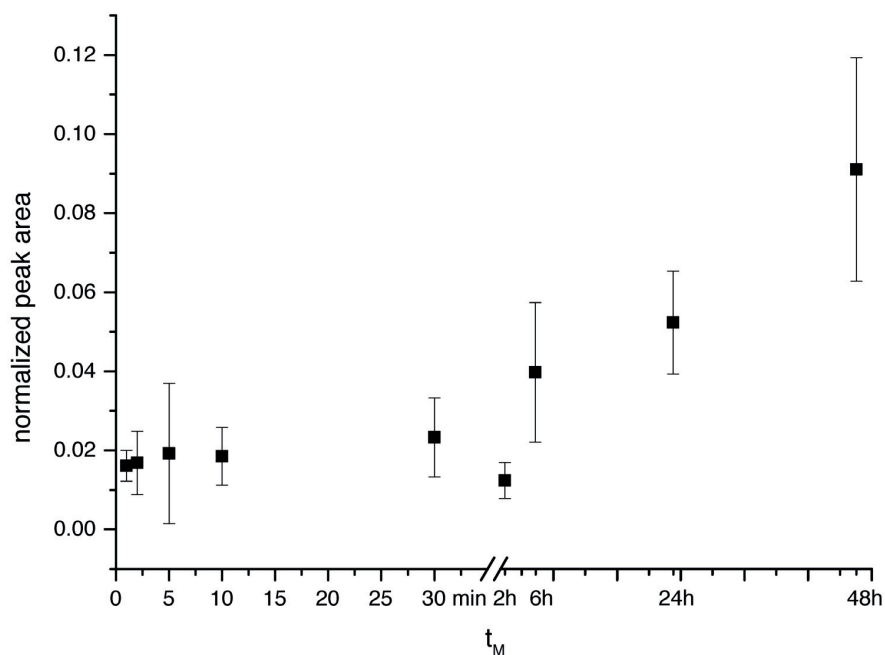


Figure 5.2: Evolution of calculated $P=O:Al-O-P$ peak area ratio with increasing t_M . The chemical species and the area of their respective peaks are identified from the deconvolution of the $O1s$ peak of the formed SAMs, as obtained from the XPS spectra.

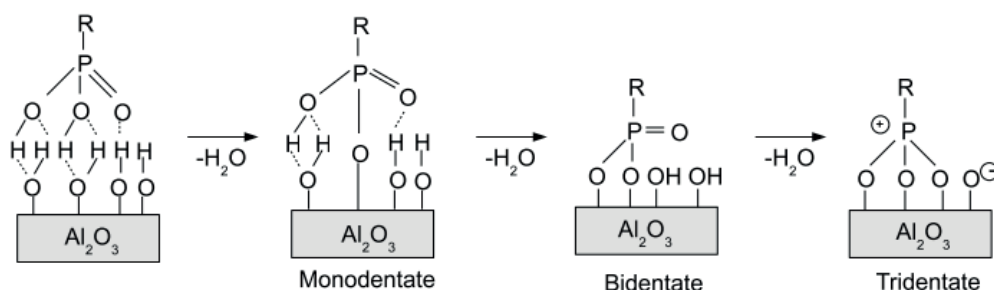


Figure 5.3: Bonding modes for alkylphosphonic acids on the hydroxylated surface of Al_2O_3 . The system passes from an initial physisorbed state to the mono- and bidentate state. The last moiety from the $-PO(OH)_2$ headgroup to be consumed is the $=O$, reaction of which with the surface leads to tridentate bonding mode. Reproduced with permission from reference [8].

CA measurements (see Figure 5.4) appear to support our hypothesis of a three step-process. For $t_M = 1$ min the recorded values are below those typically reported in the literature for organic SAMs [9], [28], which can be attributed to a higher contribution from the hydrophilic, still exposed, substrate. As t_M increases CA increases, reaching a

maximum value of $105.5^\circ \pm 0.5^\circ$ at $t_M = 2$ h, indicating coverage of the surface by a gradually better ordered organic film. The subsequent decrease of recorded values can be attribute to an increasing concentration of exposed hydrophilic $-\text{PO}(\text{OH})_2$ groups, consistent with the formation of bilayers and mixed termination multilayers.

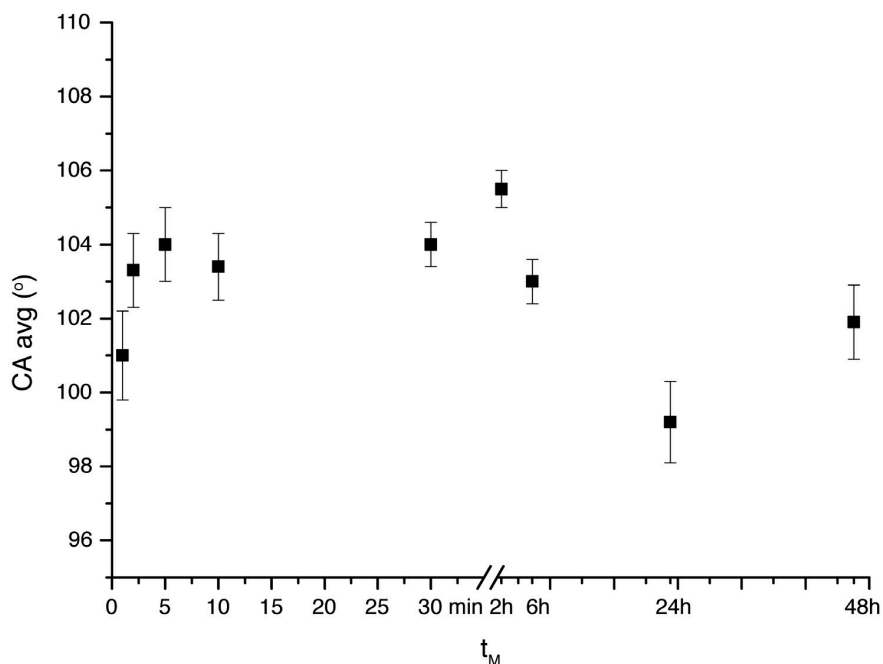


Figure 5.4: Evolution of static CA for ODPAs SAMs formed at increasing t_M . CA of O_2 plasma cleaned Al_2O_3 is equal to 40° [9].

Surface topography and elasticity, E^* , have been recorded by bimodal AFM. For low t_M the surface topographical characteristics were found to follow a narrow distribution, centered at 0 nm. The distribution broadened for $t_M = 6$ h, became narrow anew for $t_M = 24$ h and finally broadened again for $t_M = 48$ h. It was hypothesized that the initial narrow distribution represented the addition of more ligand molecules to the flat substrate and their gradual adoption of an ordered configuration. At $t_M = 6$ h the broadening of the distribution could be attributed to the onset of multilayer formation and the appearance of the first islands on top of the well-ordered, underlying monolayer. Since at $t_M = 24$ h the distribution becomes narrow again, and knowing that for this time point contact angle is minimized, it was assumed that a complete, or near complete, bilayer is formed. At $t_M = 48$ h the surface height distribution exhibited maximum diversity, possibly as multilayer islands are formed on top of the bilayer.

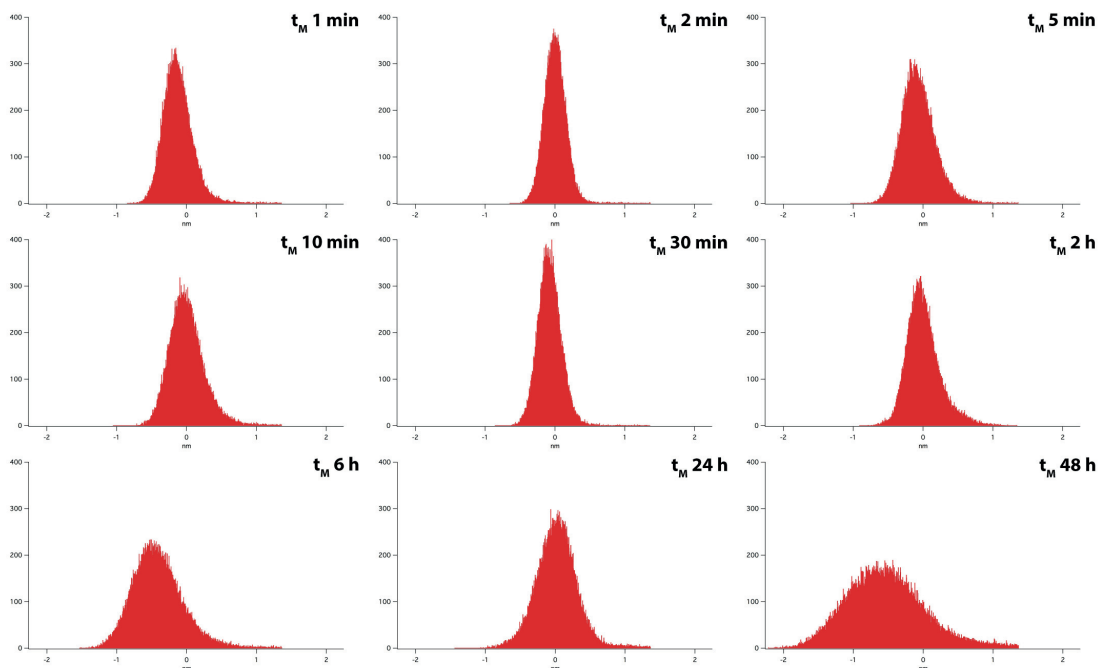


Figure 5.5: Representative height distribution for ODPA SAMs formed on Al_2O_3 for increasing t_M . For $t_M \leq 2\text{ h}$ most features are centered at 0 nm, and the distribution is narrow. Increase of t_M leads to a broadening of the height distribution peaks, indicating the appearance of features of varying height, most probably multilayer islands.

The temporal evolution of E^* (see Figure 5.6 and Figure 5.7) can further support our hypothesis regarding the kinetics of ODPA SAM formation. At $t_M = 1\text{ min}$ E^* was found equal to $1.486\text{ GPa} \pm 0.139\text{ GPa}$, value that increased to $2.116\text{ GPa} \pm 0.148\text{ GPa}$ for $t_M = 2\text{ min}$. This behavior was attributed to an initially physisorbed, disordered and seemingly sparse organic layer covering the surface. As ligands began to bind to the surface and adopt a lying-down configuration, due to dominant substrate-ligand interactions, E^* appears higher, as the contribution of the substrate is higher. This behavior has been recorded also for short alkanethiol SAMs, as discussed in Chapter 4. The adsorption of more ligand molecules to the SAM lead to the formation of a denser, yet still not well-organized submonolayer. As t_M increased E^* increased further, leading to the hypothesis that the initially disorganized monolayer gradually adopted a well-ordered configuration. This evolution, similar to the evolution of thiol SAMs from a lying-down to a standing-up phase upon increased exposure time to the thiol solution or vapour, indicated that as ligand density increases, van der Waals interactions between the neighboring molecules become more significant, allowing the orientation of the ligands to be almost perpendicular to the surface plane. The maximum value of E^* , $2.503\text{ GPa} \pm 0.210\text{ GPa}$, was reached for $t_M = 2\text{ h}$. Island formation at $t_M = 6\text{ h}$ could explain the observed minimization of E^* ; formation of a relatively ordered bilayer at $t_M = 24\text{ h}$ lead to

a uniform increase of E^* along the whole surface. The formation of multilayer islands on top of the underlying mono- and bilayers at $t_M = 48$ h was further confirmed by a lateral variation of the recorded E^* .

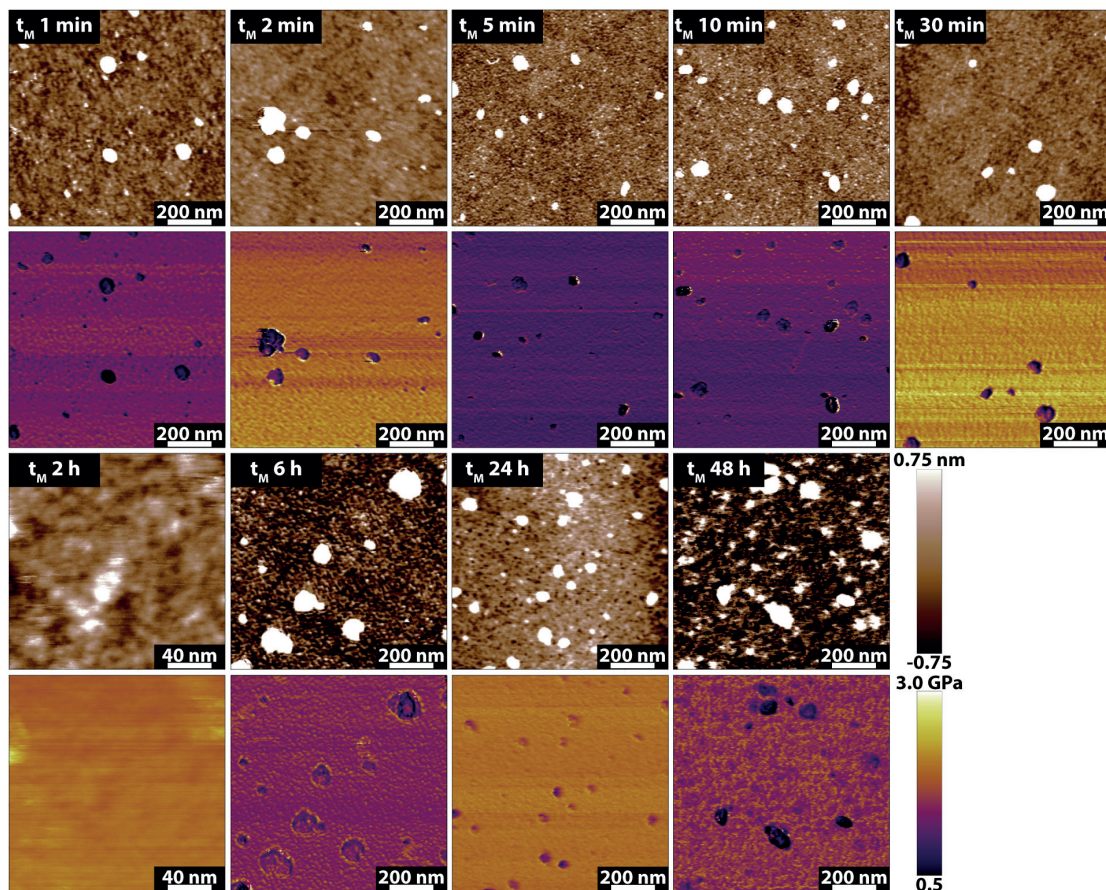


Figure 5.6: Evolution of surface topography and E^* for increasing t_M . SAM formation progresses from initially disordered and largely physisorbed submonolayer, at $t_M = 1$ min, to a chemisorbed submonolayer, at $t_M = 2$ min, mostly in a lying-down configuration. Ligand adsorption progresses rapidly, resulting in a disordered chemisorbed layer for $t_M = 5$ min and 10 min. At $10 \text{ min} < t_M \leq 30 \text{ min}$ ligand surface concentration reaches the maximum possible value, stage that is followed by significant ordering of the molecules. At $t_M = 2$ h a SAM with maximum ligand surface concentration and E^* is obtained, indicating a dense, well-ordered structure. Continuous exposure of the already formed SAMs to ligand solution results in the formation of multilayers. For $t_M = 6$ h the formation of islands on top of the already formed SAM induces an increase in surface roughness and a decrease of E^* . At $t_M = 24$ h the appearance of an almost complete physisorbed layer can be observed, which further develops into multilayer islands for $t_M = 48$ h. At the intermittent step between the appearance of islands, E^* presents a local maximum, indicating that the physisorbed molecules most likely exhibit a degree of ordering, possibly forming an almost complete bi- or multilayer.

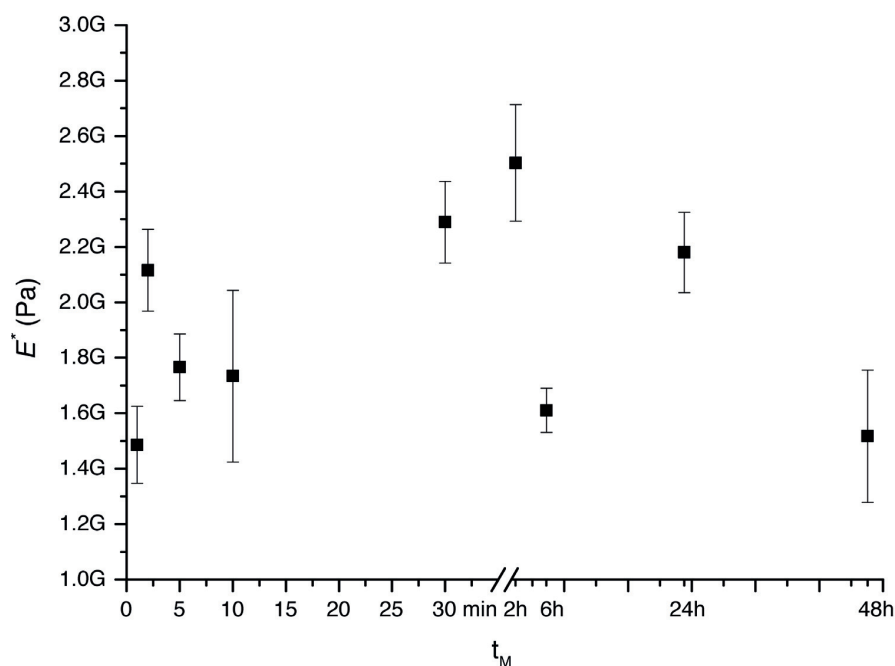


Figure 5.7: Evolution of E^* over t_M . Initial low surface elasticity, E^* , can be attributed to an initially physisorbed disorganized layer of ODPA. Subsequent increase indicates the formation of a chemisorbed monolayer, of gradually increasing order. Maximum E^* for $t_M = 2$ h can be attributed to a well ordered, densely packed ODPA SAM. For higher t_M multilayers begin forming on top of the SAMs. It is interesting to note that even these physisorbed formations exhibit different degrees of ordering and subsequently show varying elasticity.

The above-presented results indicated that ODPA SAM formation can be seen as a three-step process. During the first step, for $t_M \leq 1$ min, the ligand molecules form an initially disordered submonolayer, with a high density of tridentate bonds. For $2 \text{ min} \leq t_M \leq 2 \text{ h}$, a small, gradual increase in ligand surface concentration is observed, indicating that during this second step, already adsorbed molecules begin to form well-ordered structures. Moreover, a few ligands are further bound to the binding sites freed by the standing-up ligands. The bulk of ligand ordering and monolayer densification takes place during this second step. The third step entails physisorption of molecules on top of the already formed monolayer and bi- or multilayer formation.

In order to quantify the kinetics of ODPA SAM and multilayer formation, surface coverage was calculated and fitted to a suitable adsorption model, with the adsorption rate used as one of the fitting parameters.

The models reported in the literature and tested here were the simple Langmuir adsorption model (L), diffusion-limited Langmuir (DLL), non-diffusion limited second order Langmuir (SOL) [19], two-step Langmuir (TSL) [29], simple diffusion model (D)

[19], and the modified Kisliuk (K) model (see Appendix B, Table B.1) [19], [30]. Surface coverage, $\theta(t)$, was calculated as the ratio of experimentally determined surface P% to average maximum P% for a monolayer (2.1%) as reported in the literature [31], [32]. The data was then fitted to multiple adsorption models via regression analysis, using the least squares method (see Appendix B, Table B.2). The best fitting was obtained for a two-step Langmuir model, previously used by Helmy et al. for ODPA SAM formation on TiO_2 and given by equation 5.1 [29].

$$\theta(t) = \theta_o(1 - ae^{-k_{a,1}Ct} - (1 - a)e^{-k_{a,2}Ct}) \quad (5.1)$$

The first step of this model can describe the rapid physisorption and adsorption of ligands on free, easily accessible binding sites on the surface of activated Al_2O_3 . During the first step, up to and including $t_M = 30$ min, 59% of the total material is being absorbed at a rate $k_{a,1} = 2.65 \times 10^3 (\text{M} \times \text{min})^{-1}$, allowing the monolayer to approach the maximum possible ligand density. During the second step ligand adsorption is much slower, with adsorption rate $k_{a,2} = 1.41 (\text{M} \times \text{min})^{-1}$. Grouping of $t_M = 2$ h along with $t_M = 6$ h, 24 h and 48 h, when our experimental data shows that multilayer formation takes place, highlights the importance of continuing incubation of the surfaces in solution even after maximum ligand density has been reached. During the last stage of monolayer formation very few additional ligand molecules are added to the surface, but van der Waals interactions between the already adsorbed molecules enhance ligand ordering. At this stage the maximum number of tridentate-bound ligands is reached.

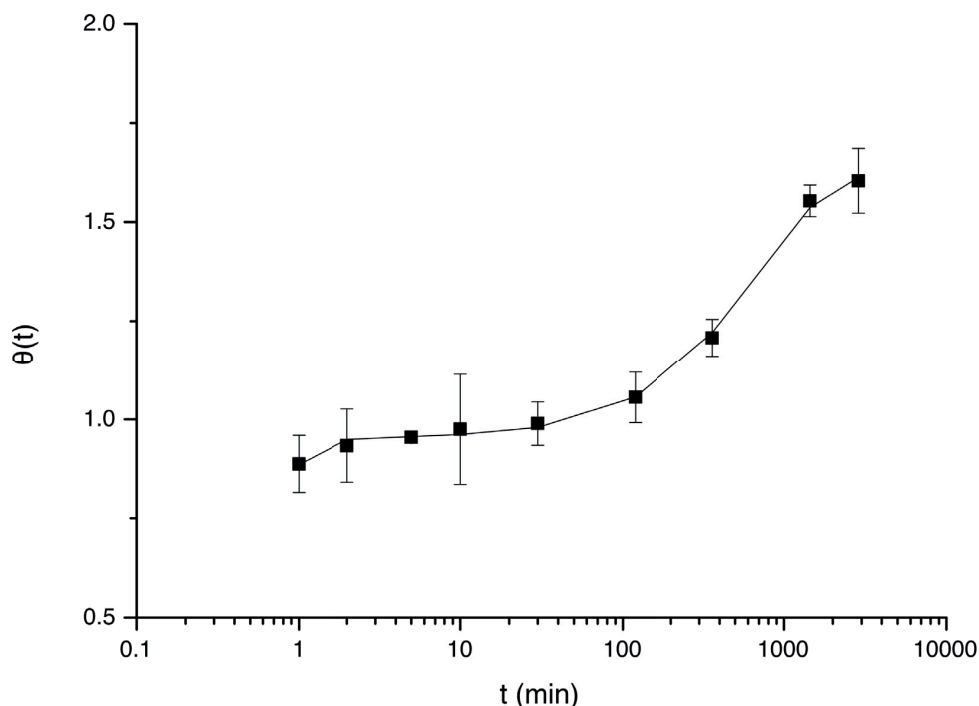


Figure 5.8: Theoretically predicted evolution of ODPA adsorption on Al_2O_3 (solid line) and experimentally calculated surface coverage, $\theta(t)$ (squares). The best fit obtained was produced from a two-step Langmuir adsorption model.

In the available literature the adsorption rate has been calculated by a number of different techniques. Koutsioubas et al. used surface plasmon resonance (SPR) [19], and correlated monolayer thickness to t_M . Helmy et al. used thermogravimetric analysis (TGA) [29], and the total carbon content of the samples was correlated to t_M . The adsorption of ODPA on Al_2O_3 has also been semi-quantitatively determined in a study by Giza et al. [33], who used the quartz crystal microbalance (QCM) to detect the binding of the ligands on plasma pretreated Al_2O_3 . All three studies identified the formation of an ODPA SAM as a two-step process, involving ligand adsorption and ordering. However, in all cases different rates for the formation of ODPA SAMs were calculated. Moreover, in the case of the first two the rate of monolayer formation was significantly lower from the rate $k_{a,1}$ calculated here. In the case of the TGA study, this difference could be attributed to the low resolution limit and large relative error of the technique, that may not allow the detection of the first rapid steps of ligand adsorption. SPR shows in general lower error limit and higher sensitivity, but it is possible that the technique cannot accurately detect the rapid steps of ligand adsorption in a sparse lying-down configuration, leading to the calculation of slower rate of monolayer formation. Moreover, the surfaces used in the study were not treated prior to introduction of the ligand solution into the chamber, and therefore the availability of binding sites would be

low. On the other hand, the QCM study by Giza et al. showed that ligand adsorption was largely completed after 4 min – 6 min, being in good agreement with the experimental results presented here. It should be noted that, apart from the high sensitivity of the technique to binding events, making it perhaps the most suitable method to determine the kinetic evolution of SAMs' formation, the surfaces used were pretreated by plasma etching. This observation highlights that the pretreatment of a surface can be a significant factor of the kinetics of SAM formation.

To further illustrate this point, 5 Al_2O_3 surfaces were rinsed in Milli-Q and isopropanol to remove dust, dried and incubated in 1 mM ethanolic ODPa solution for 24 h. The samples were analyzed via XPS and the average atomic surface concentration for P was found equal to $1.44\% \pm 0.11\%$. It is reminded that for as short as $t_M = 1$ min the P atomic surface concentration on SAMs formed on the plasma activated surfaces was found equal to $1.86\% \pm 0.15\%$. The removal of organic contaminants from a surface and the generation of binding sites via a suitable pretreatment method can significantly accelerate the speed of SAM formation and enhance the final density of the monolayer.

5.3.2. Alkylphosphonic acid SAMs on industrial surfaces

Alkylphosphonic acid SAMs on Al_2O_3 are an interesting system further from purely academic research as they are being used for a number of products: from deposition of organic electronics on extremely smooth surfaces, to monolayers as a form of pretreatment on industrial aluminium and aluminium alloys surfaces. One of the goals of this research is to showcase the conditions under which a laboratory technique can be implemented in the production line of a big company in order to evaluate the quality of its product. Bimodal AFM was performed on industrial aluminium alloy surfaces of the line 6xxx, onto which a phosphonic acid monolayer has been deposited. SAMs formed on different alloys exhibit detectable differences in elasticity. Figure 5.9 shows representative areas of the imaged samples. Recorded values of E^* indicate the formation of supple organic films, consistent with the short t_M used in industrial applications. SAMs formed on surfaces with the highest surface roughness exhibit the lowest E^* .

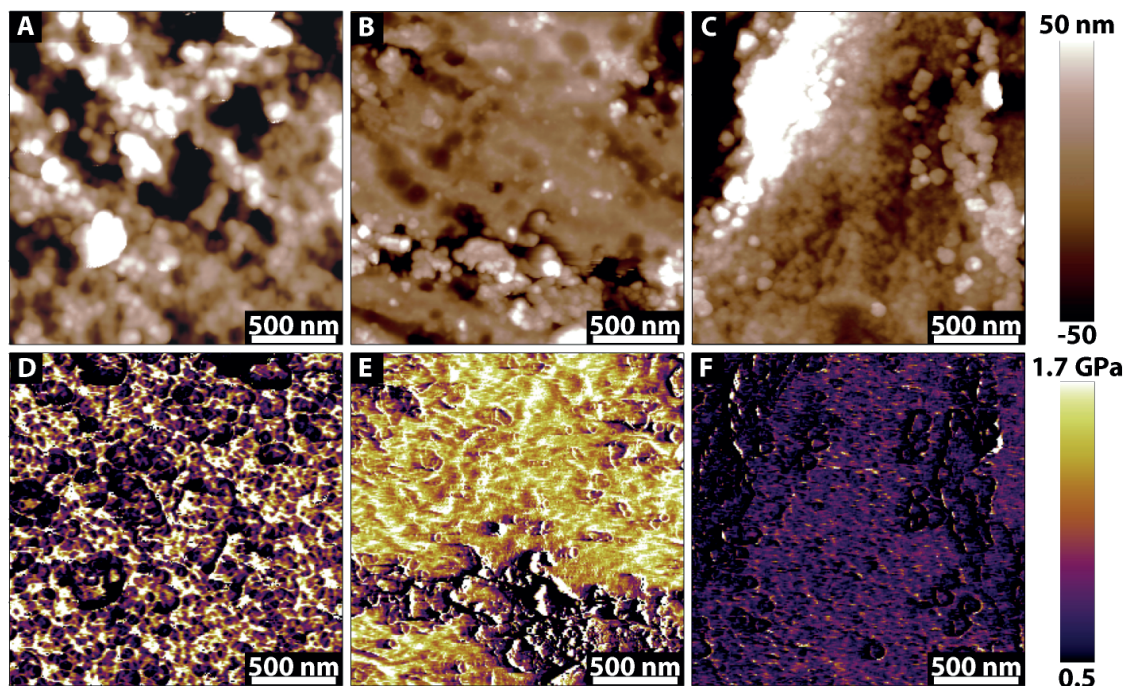


Figure 5.9 (A-F): Topography and E^* for three different aluminium alloys of the series 6xxx. A correlation between surface roughness and E^* can be observed.

5.4. Conclusions

Having established through our previous study on alkanethiol SAMs on Au (111) by bimodal AFM that the technique can be accurately used to gauge the mechanical properties of molecularly thin films with small variations in chemical composition, bimodal AFM was used to evaluate the mechanical properties of SAMs with different configurations of the same molecule, as a result of changes in monolayer formation time, t_M . Supported by XPS and CA, we were able to identify three steps of ODPA adsorption on Al_2O_3 : initial rapid adsorption of ligands in multiple binding sites for $t_M \leq 1$ min, slower adsorption and ligand ordering in the monolayer for $2 \text{ min} \leq t_M \leq 2 \text{ h}$ and, lastly, bi- and multilayer formation for $6 \text{ h} \leq t_M \leq 48 \text{ h}$.

Using the mechanical properties of SAMs at different time points, we can estimate the configuration of amorphous hydrocarbon structures, with no need of synchrotron radiation. Moreover, the mechanical properties and structure of incomplete or disordered SAMs were probed, and a process at which the highest degree of ligand ordering and surface concentration can be achieved.

Fitting our data to a suitable adsorption model revealed two steps in the adsorption process: one extremely rapid, driven by the free energy minimization of the system through bond formation, and one much slower, corresponding to ligand physisorption.

Finally, we demonstrate that bimodal AFM can be applied for the characterization of alkylphosphonic acid SAMs prepared under industrially relevant conditions on aluminium alloys, without being hindered by the high roughness of the substrate. Our results indicate that surface roughness can affect the ordering of the monolayers, as SAMs deposited on alloys with the highest variability in surface features were characterized by the lowest E^* . The observed substrate roughness effect can be explained by entanglement and repulsive interactions between the closely spaced ligand molecules, hindering the formation of a well-ordered SAM.

5.5. References

- [1] W. Gao, L. Dickinson, C. Grozinger, F. G. Morin, and L. Reven, "Self-assembled monolayers of alkylphosphonic acids on metal oxides," *Langmuir*, vol. 12, no. 26, pp. 6429–6435, 1996.
- [2] C. Yee, G. Kataby, A. Ulman, T. Prozorov, H. White, A. King, M. Rafailovich, J. Sokolov, and A. Gedanken, "Self-assembled monolayers of alkanesulfonic and -phosphonic acids on amorphous iron oxide nanoparticles," *Langmuir*, vol. 15, no. 21, pp. 7111–7115, 1999.
- [3] A. Jedaa, M. Burkhardt, U. Zschieschang, H. Klauk, D. Habich, G. Schmid, and M. Halik, "The impact of self-assembled monolayer thickness in hybrid gate dielectrics for organic thin-film transistors," *Org. Electron.*, vol. 10, no. 8, pp. 1442–1447, 2009.
- [4] M. Burkhardt, A. Jedaa, M. Novak, A. Ebel, K. Voïtchovsky, F. Stellacci, A. Hirsch, and M. Halik, "Concept of a molecular charge storage dielectric layer for organic thin-film memory transistors," *Adv. Mater.*, vol. 22, pp. 2525–2528, 2010.
- [5] C. M. Jäger, T. Schmaltz, M. Novak, A. Khassanov, A. Vorobiev, M. Hennemann, A. Krause, H. Dietrich, D. Zahn, A. Hirsch, M. Halik, and T. Clark, "Improving the charge transport in self-assembled monolayer field-effect transistors: From theory to devices," *J. Am. Chem. Soc.*, vol. 135, no. 12, pp. 4893–4900, 2013.
- [6] L. Portilla and M. Halik, "Smoothly tunable surface properties of aluminum oxide core-shell nanoparticles by a mixed-ligand approach," *ACS Appl. Mater. Interfaces*, vol. 6, no. 8, pp. 5977–82, 2014.
- [7] L. Portilla, S. H. Etschel, R. R. Tykwinski, and M. Halik, "Green processing of metal oxide core-shell nanoparticles as low-temperature dielectrics in organic thin-film transistors," *Adv. Mater.*, vol. 27, no. 39, pp. 5950–5954, 2015.
- [8] R. Luschtinetz, A. F. Oliveira, J. Frenzel, J. O. Joswig, G. Seifert, and H. A. Duarte, "Adsorption of phosphonic and ethylphosphonic acid on aluminum oxide surfaces," *Surf. Sci.*, vol. 602, no. 7, pp. 1347–1359, 2008.
- [9] T. Bauer, T. Schmaltz, T. Lenz, M. Halik, B. Meyer, and T. Clark, "Phosphonate- and carboxylate-based self-assembled monolayers for organic devices: a theoretical study of surface binding on aluminum oxide with experimental support," *ACS Appl. Mater. Interfaces*, vol. 5, no. 13, pp. 6073–80, 2013.
- [10] C. Queffelec, M. Petit, P. Janvier, D. A. Knight, and B. Bujoli, "Surface modification using phosphonic acids and esters," *Chem. Rev.*, vol. 112, no. 7, pp. 3777–3807,

2012.

- [11] L. G. Hector, G. A. Nitowski, S. M. Opalka, and L. Wieserman, "Investigation of vinyl phosphonic acid/hydroxylated α -Al₂O₃ (0001) reaction enthalpies," *Surf. Sci.*, vol. 494, no. 1, pp. 1–20, 2001.
- [12] P. Thissen, M. Valtiner, and G. Grundmeier, "Stability of phosphonic acid self-assembled monolayers on amorphous and single-crystalline aluminum oxide surfaces in aqueous solution.," *Langmuir*, vol. 26, no. 1, pp. 156–64, 2010.
- [13] P. Thissen, A. Vega, T. Peixoto, and Y. J. Chabal, "Controlled, low-coverage metal oxide activation of silicon for organic functionalization: unraveling the phosphonate bond.," *Langmuir*, vol. 28, no. 50, pp. 17494–505, 2012.
- [14] R. Lushtinetz, A. F. Oliveira, H. A. Duarte, and G. Seifert, "Self-assembled monolayers of alkylphosphonic acids on aluminum oxide surfaces - A theoretical study," *Zeitschrift für Anorg. und Allg. Chemie*, vol. 636, no. 8, pp. 1506–1512, 2010.
- [15] D. M. Spori, N. V Venkataraman, S. G. P. Tosatti, F. Durmaz, N. D. Spencer, and S. Zürcher, "Influence of alkyl chain length on phosphate self-assembled monolayers.," *Langmuir*, vol. 23, no. 15, pp. 8053–60, 2007.
- [16] M. D. Losego, J. T. Guske, A. Efremenko, J.-P. Maria, and S. Franzen, "Characterizing the molecular order of phosphonic acid self-assembled monolayers on indium tin oxide surfaces.," *Langmuir*, vol. 27, no. 19, pp. 11883–8, 2011.
- [17] K. Fukuda, T. Hamamoto, T. Yokota, T. Sekitani, U. Zschieschang, H. Klauk, and T. Someya, "Effects of the alkyl chain length in phosphonic acid self-assembled monolayer gate dielectrics on the performance and stability of low-voltage organic thin-film transistors," *Appl. Phys. Lett.*, vol. 95, no. 20, pp. 203301–3, 2009.
- [18] A. Khassanov, H. G. Steinrück, T. Schmaltz, A. Magerl, and M. Halik, "Structural investigations of self-assembled monolayers for organic electronics: Results from X-ray reflectivity," *Acc. Chem. Res.*, vol. 48, no. 7, pp. 1901–1908, 2015.
- [19] A. G. Koutsioubas, N. Spiliopoulos, D. L. Anastassopoulos, A. A. Vradis, and G. D. Priftis, "Formation of alkane-phosphonic acid self-assembled monolayers on alumina: an in situ SPR study," *Surf. Interface Anal.*, vol. 41, no. 11, pp. 897–903, 2009.
- [20] R. Hofer, M. Textor, and N. D. Spencer, "Alkyl phosphate monolayers, self-assembled from aqueous solution onto metal oxide surfaces," *Langmuir*, vol. 17, no. 13, pp. 4014–4020, 2001.
- [21] W. Vogel, B. Rosner, and B. Tesche, "Structural investigations of

- octadecylphosphonic acid multilayers," *J. Phys. Chem.*, vol. 97, no. 1, pp. 11611–11616, 1993.
- [22] I. Gouzman, M. Dubey, M. D. Carolus, J. Schwartz, and S. L. Bernasek, "Monolayer vs. multilayer self-assembled alkylphosphonate films: X-ray photoelectron spectroscopy studies," *Surf. Sci.*, vol. 600, no. 4, pp. 773–781, 2006.
- [23] G. Guerrero, J. G. Alauzun, M. Granier, D. Laurencin, and P. H. Mutin, "Phosphonate coupling molecules for the control of surface/interface properties and the synthesis of nanomaterials," *Dalton Trans.*, vol. 42, no. 35, pp. 12569–85, 2013.
- [24] R. Garcia and R. Proksch, "Nanomechanical mapping of soft matter by bimodal force microscopy," *Eur. Polym. J.*, vol. 49, no. 8, pp. 1897–1906, 2013.
- [25] R. Garcia and E. T. Herruzo, "The emergence of multifrequency force microscopy," *Nat. Nanotechnol.*, vol. 7, no. 4, pp. 217–226, 2012.
- [26] A. Labuda, M. Kocun, T. Walsh, J. Meinhold, T. Proksch, W. Meinhold, and R. Proksch, "Calibration of higher eigenmodes of cantilevers," *Rev. Sci. Instrum.*, vol. 87, no. 73705, pp. 1–11, 2016.
- [27] B. Branch, M. Dubey, A. S. Anderson, K. Artyushkova, J. K. Baldwin, D. Petsev, and A. M. Dattelbaum, "Investigating phosphonate monolayer stability on ALD oxide surfaces," *Appl. Surf. Sci.*, vol. 288, pp. 98–108, Jan. 2014.
- [28] C. E. Taylor and D. K. Schwartz, "Octadecanoic acid self-assembled monolayer growth at sapphire surfaces," *Langmuir*, vol. 19, no. 12, pp. 2665–2672, 2003.
- [29] R. Helmy and A. Y. Fadeev, "Self-assembled monolayers supported on TiO₂: Comparison of C₁₈H₃₇SiX₃ (X = H, Cl, OCH₃), C₁₈H₃₇Si(CH₃)₂Cl, and C₁₈H₃₇PO(OH)₂," *Langmuir*, vol. 18, no. 23, pp. 8924–8928, 2002.
- [30] A. P. Henderson, L. N. Seetohul, A. K. Dean, P. Russell, S. Pruneanu, and Z. Ali, "A novel isotherm, modeling self-assembled monolayer adsorption and structural changes," *Langmuir*, vol. 25, no. 2, pp. 931–938, 2009.
- [31] E. Hoque, J. a DeRose, G. Kulik, P. Hoffmann, H. J. Mathieu, and B. Bhushan, "Alkylphosphonate modified aluminum oxide surfaces," *J. Phys. Chem. B*, vol. 110, no. 22, pp. 10855–61, 2006.
- [32] E. Hoque, J. a Derosé, P. Hoffmann, H. J. Mathieu, B. Bhushan, and M. Cichomski, "Phosphonate self-assembled monolayers on aluminum surfaces," *J. Chem. Phys.*, vol. 124, no. 17, p. 174710, 2006.
- [33] M. Giza, P. Thissen, and G. Grundmeier, "Adsorption kinetics of organophosphonic acids on plasma-modified oxide-covered aluminum surfaces," *Langmuir*, vol. 24,

no. 16, pp. 8688–8694, 2008.

Chapter 6

Summary, conclusions and outlook

6.1. Summary and conclusions

The mechanical properties of a material can offer an indication on its molecular or atomic structure. Highly organized crystalline materials exhibit very high Young's moduli, E ; for example, E_{diamond} is approximately equal to 1 TPa. On the other hand, disordered organic materials have much lower elasticity values; E of natural rubber does not in general exceed 4 MPa. Furthermore, elementally identical materials show different elasticity depending on the degree of ordering of their constituents. E of low density polyethylene (LDPE) is only 0.10 GPa, but increases to 0.88 GPa for high density polyethylene (HDPE). In the same way that the elasticity of bulk materials can be used to determine their structure, it can provide valuable insight into the level of ordering of molecularly thin organic films.

The research question addressed in this thesis has been how small changes in the nanoscale can affect macroscopic properties of SAMs, in particular elasticity. Currently employed methods of SAM characterization, such as XRR and NEXAFS, are typically difficult to access, can be applied only for the characterization of SAMs deposited on ideal (*i.e.* atomically flat) surfaces and provide information on the average behavior of the surface. Can a different approach to this problem be found? By detecting changes in the elasticity, would it be possible to interpret them as indications of the interactions at play at the nanoscale? The use of commercially available AFMs excited in the bimodal configuration for the nanomechanical characterization of soft organic molecularly thin films on significantly stiffer substrates was investigated. The motivation of this study has been a desire to bridge an apparent lack of cohesion between academic and industrial practices, stemming from the difficulty of applying the current characterization methods of the former to the latter.

Bimodal AFM has been used for the accurate nanomechanical characterization of bulk materials and polymer thin films, but its applicability on the characterization of complex multilayered materials, such as the monolayer-substrate complex, has not been demonstrated yet.

Ligand structure and monolayer formation time, parameters known to affect the structure and ordering of SAMs, were varied and the surface elasticity of SAMs, E^* , was measured and correlated to them.

Alkanethiol homoligand SAMs were deposited from solution of ligands of varying length. E^* of the different SAMs was successfully measured using the commercially available bimodal AMFM mode in the Cypher and MFP3D AFMs using commercially available silicon nitride cantilevers. It was possible to differentiate between the mechanical behavior of SAMs by chemically similar ligands of varying length. The elasticity of SAMs of shorter ligands showed a larger contribution of the substrate, with E^* of C4 SAMs found equal to $2.79 \text{ GPa} \pm 0.13 \text{ GPa}$. Increase of ligand length resulted in a monotonic decrease of E^* , from $1.87 \text{ GPa} \pm 0.09 \text{ GPa}$ for C7 SAMs to $1.75 \text{ GPa} \pm 0.19 \text{ GPa}$ for C11 SAMs. A local maximum for C12 SAMs was observed, with $E^* = 1.93 \text{ GPa} \pm 0.06 \text{ GPa}$. Further increase of ligand length resulted in minimization of E^* , found equal to $0.96 \text{ GPa} \pm 0.07 \text{ GPa}$ for C18 SAMs. These results, apart from clearly showing that differentiating between chemically similar SAMs based on elasticity was possible, offered the first indication of molecular ordering in the nanoscale: the local maximum of E^* for C12 can be an indication of better ordering of the ligands than in C7, OT, C9 and C11 SAMs. The effect of the substrate was deconvoluted from E^* , using a formula reported in the literature and modified to account for the AFM tip geometry. The deconvoluted elasticity, E_{SAM} , was then used to interpret the level of ligand ordering. Short ligands appeared to form softer, more disordered SAMs, while addition of $-\text{CH}_2$ groups in the spacer chain enhanced van der Waals neighbor-neighbor interactions, promoting better ordering in the system. C12 SAMs were found to be the best-ordered system of all SAMs studied. C18 SAMs appeared to form much softer SAMs, indicating introduction of defects by the additional $-\text{CH}_2$ groups. Having established that bimodal AFM can differentiate between molecularly thin materials on hard substrates, it was later used to characterize binary OT:TMA SAMs. The high lateral resolution of the technique has allowed the identification of chemically different domains, visualizing for the first time the position of organic molecules in an amorphous thin material at domains smaller than 10 nm.

The kinetic evolution of ODPA SAM formation on Al_2O_3 was studied. Guided by XPS and CA data, different regimes of SAM formation were identified and mechanical properties were attributed to each regime. To the best of our knowledge this is the first time a direct correlation between stages of monolayer formation, SAM structure, wettability,

and elasticity has been achieved. Three stages of monolayer formation were identified. During the first step, for $t_M \leq 2$ min, rapid ligand absorption and adsorption to a lying down configuration took place. The second step, identified for $5 \text{ min} \leq t_M \leq 2 \text{ h}$, entailed slower ligand adsorption to the free binding sites, maximum tridentate bond formation and ligand orientation to form well-ordered, densely packed SAMs. At $t_M \geq 6 \text{ h}$ the third step was reached, during which multilayers were formed. The XPS surface concentration data were fitted to a suitable absorption model, allowing the calculation of the absorption rate for the monolayer and the multilayer formation. We further demonstrated that bimodal AFM can be used to measure the elasticity of SAMs prepared on industrial aluminium surfaces. Alkylphosphonic acid compounds have been used for surface modification in industry since 1961, but this is the first time that a technique has been proposed to investigate the quality and structure of the monolayers, allowing for optimization of process and product design.

At this point, it is interesting to draw a brief comparison between the thiol and alkylphosphonic acid SAMs. The maximum value of E^* recorded for ODPA SAMs was much larger than E^* of C18 SAMs. This behavior can indicate that alkylphosphonic acid SAMs can reach states of higher order than long chain alkanethiol SAMs. This difference can be a result of the generally more rigid bi- or tridentate binding of the $-\text{PO}(\text{OH})_2$ headgroup to the hydroxyl-terminated Al_2O_3 , which could favor the formation of a standing up phase. On the other hand, the mobile S-Au bond can allow greater conformational freedom, allowing the formation of SAMs richer in defects. Ultimately, the ligand density of phosphonic acid SAMs can be slightly higher or comparable to thiol SAMs of ligands of similar length, but differences in the binding modes between the headgroups and the substrates will lead to layers of varying ordering.

6.2. Outlook

The work presented here has demonstrated that bimodal AFM can provide accurate, reproducible and quantitative characterization of the surface elasticity of molecularly thin films, without being limited by the type and roughness of the substrate. This capability of the technique, combined with the typical high lateral resolution of the AFM, can offer an invaluable tool for the detailed characterization of thin soft films and surfaces. In conjunction to other techniques, such as ellipsometry or nanoscratching, further information on the thickness and molecular ordering of the characterized SAMs can be obtained. The combined results of these techniques can offer an accurate three-dimensional description of SAMs. Extending the concept further, if time can be viewed as

a fourth dimension, *in situ* observation of SAM deposition via bimodal AFM can offer a four-dimension description of monolayer formation and ordering.

A next step would be to further investigate structural changes in SAMs induced by branched, bulky, or rigid ligands, as well as phase separation in their binary SAMs. Preliminary results on the characterization of a binary tert-nonyl mercaptan (TNM):mercaptopropionic acid (MPA) SAMs show indications of phase separation. Three phases of different E^* appear to contribute to the average elasticity of the monolayer (see Figure 6.1). The behavior of each one of the two ligands can present considerable interest as well. TNM is characterized by the substitution of the H atoms in the $-\text{CH}_2$ group closest to the $-\text{SH}$ head by two methyl groups. This branching could induce disorganizing of the monolayer, which should then appear softer. MPA on the other hand, is a short molecule with a charged endgroup that could promote ordering.

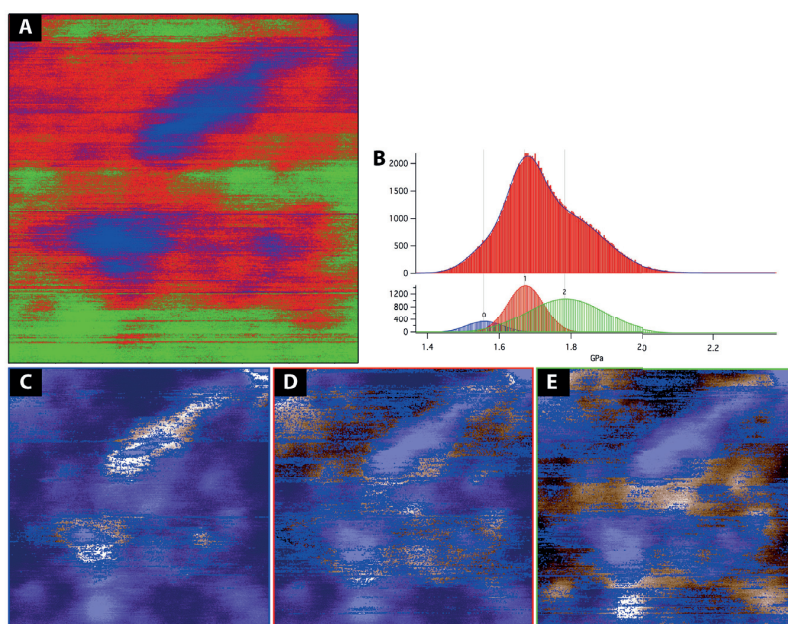


Figure 6.1 (A-E): E^* map of binary TNM:MPA SAM (A), distribution of E^* and deconvolution to three constituent peaks (B). The average elasticity of each peak $\pm \sigma$ was used to identify the topographical features corresponding to each elasticity value (C-E). Further studies on the E^* of homoligand TNM and MPA SAMs is needed in order to identify the chemical identity of each area. Scan size 145x145 nm.

Ligand exchange reactions can be monitored *ex situ* by the evolution of surface elasticity. This can be particularly interesting for substrates other than the simple flat surfaces, for example Ag nanocubes. Surface-enhanced Raman spectroscopy (SERS) characterization of polyvinylpyrrolidone (PVP) protected nanocubes at different exchange reaction times has revealed that the exchange reaction rates and mechanisms are very different for the hydrophobic OT and the hydrophilic 11-mercapto-1-undecanesulfonate (MUS). AFM

imaging of the nanocubes after 10 min of PVP exchange by OT revealed the presence of domains, supporting the hypothesis that OT initially nucleates forming small islands, and the reaction progresses by slowly replacing the PVP (see Figure 6.2A-C). MUS, on the other hand, appeared to uniformly and indiscriminately replace PVP from the entire surface of the cubes (see Figure 6.2D-F). Bimodal AFM can be used to track chemical and conformational changes in the structure of the SAMs coating the nanocubes.

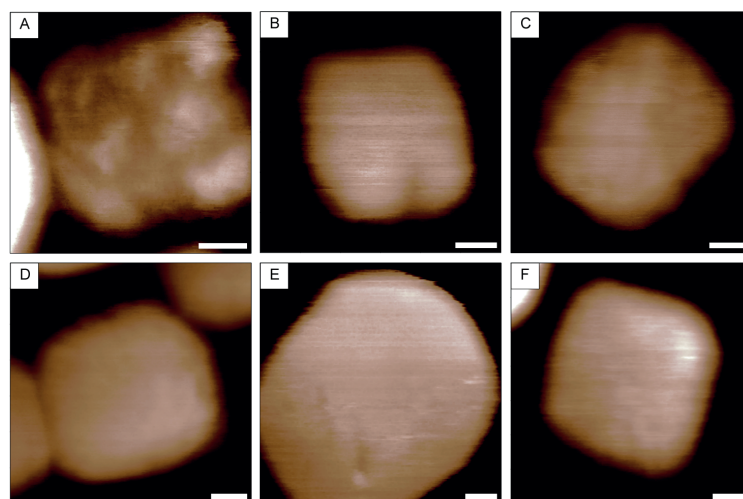


Figure 6.2 (A-F): Evolution of surface topography of AgNCs upon PVP exchange by OT (A-C) or MUS (D-F). Exchange of PVP by OT at $t = 10$ min (A) leads to significant roughening of the surface, as various taller islands and shorter domains can be observed. The height difference between the two indicates that the taller islands correspond to not-yet displaced PVP, surrounded by the shorter OT monolayer. At higher reaction times (30 h (B) and 96 h (C)) the surface of the AgNCs is smoothed significantly, suggesting full displacement of PVP by OT and subsequent full monolayer formation. The PVP-MUS exchange reaction leads to a largely uniform surface as early as $t = 10$ min (D). Surface roughness remains low even at higher reaction times (30 h (E) and 96 h (F)). Color scale range: 6.5 nm, scale bar: 10nm.

Utilizing further the direct and rapid mechanical and topographical correlation offered by the technique, biological material can be studied. Preliminary AFM imaging of live cyanobacteria has shown that the structure of the newly formed bacterial wall in dividing cells differs significantly from the old wall (see Figure 6.3). The process is completed in less than 30 min, making techniques such as force mapping unsuitable to follow the process *in situ*. Bimodal AFM however can rapidly provide information on the mechanical properties of the new wall. New walls showing different properties than the old bacterial walls offer a promising target for the development of novel antibiotics [1].

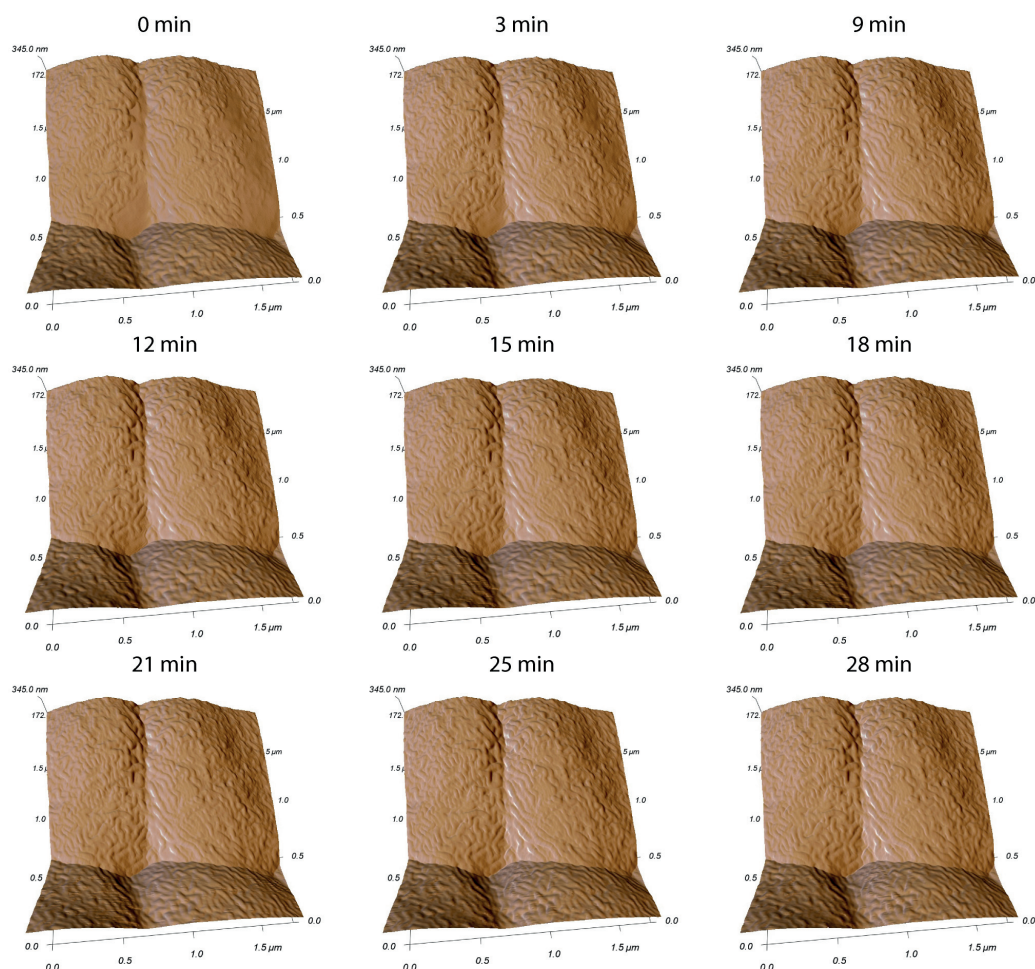


Figure 6.3: Overlay of the amplitude on the height channel showing the temporal evolution of the characteristics of the bacterial wall during the division of a unicellular cyanobacterium cell. The adoption of a wrinkled structure by the newly formed bacterial wall is a time resolved process. Bimodal AFM can be used to probe the mechanical properties of the proliferating cells, following cell division *in situ*. Every image presented in the figure was recorded in 3 min.

The use of bimodal AFM to detect mechanical properties of soft matter, and the use of surface elasticity as an indicator of molecular ordering, can offer unique possibilities for the advancement of the field. The comparative characterization of ordering at the nanoscale can be accessible for any soft material, without need for synchrotron radiation sources or limited by the features of the material itself or the substrate.

In this thesis a novel approach to determine the synthesis-structure-properties relation of organic SAMs was proposed. The method aims at the detection of structural changes in organic soft materials, by measuring their mechanical properties. The technique employed, bimodal AFM, has not been used previously for the quantitative characterization of the elasticity of multilayer materials, particularly not when the upper layer is a molecularly thin film.

The work presented here is not an exhaustive description of the field. It is my hope that the methodology proposed will be further developed and refined in the future, and used to address questions regarding the structure of complex multilayer materials, in the frame of both basic and applied research, without necessitating the use of complex and difficult to access techniques.

6.3. References

- [1] R. G. Bailey, R. D. Turner, N. Mullin, N. Clarke, S. J. Foster, and J. K. Hobbs, "The interplay between cell wall mechanical properties and the cell cycle in *Staphylococcus aureus*," *Biophys. J.*, vol. 107, no. 11, pp. 2538–2545, 2015.

Appendix A

In this section additional AFM images of the homoligand SAM triplicates discussed in Chapter 4 are presented. The presented information was omitted from the main body of the thesis for clarity. AFM images were acquired and treated as described in paragraph 4.2.

A particular characteristic of thiol SAMs is their susceptibility to environmental contamination. Contaminants appear in the AFM topography as large, rounded, tall features and appear during scanning. To avoid skewing of the data due to their effect, when the contaminants were many smaller scan sizes were recorded. Their appearance can be minimized by drying the samples under vacuum for at least 24h.

The replication of the OT:TMA binary SAM is also presented, in Figure A.8, and Figure A.9.

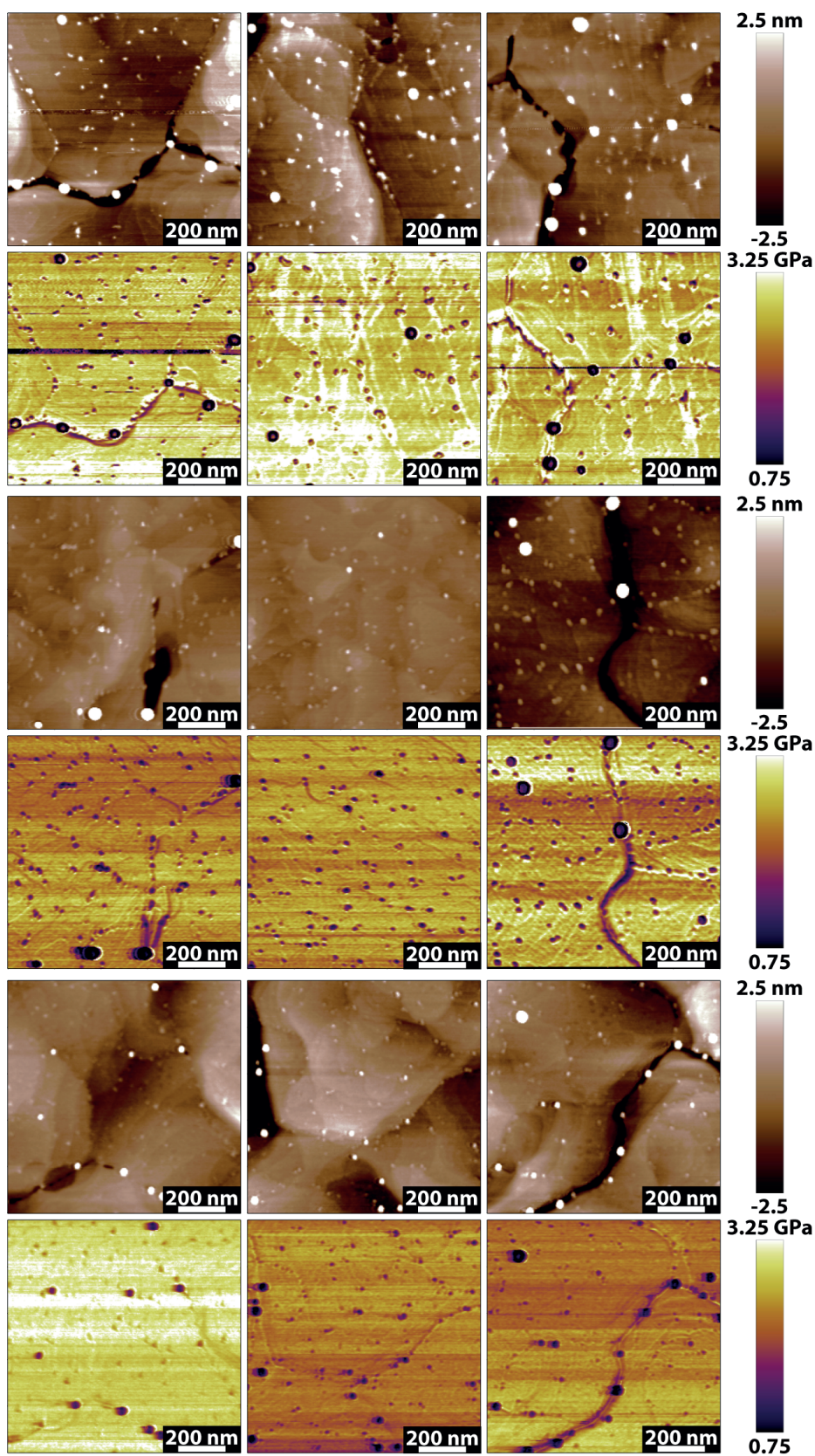


Figure A.1: Representative topography and corresponding E^* for three samples of C4 SAMs. Each row corresponds to one sample.

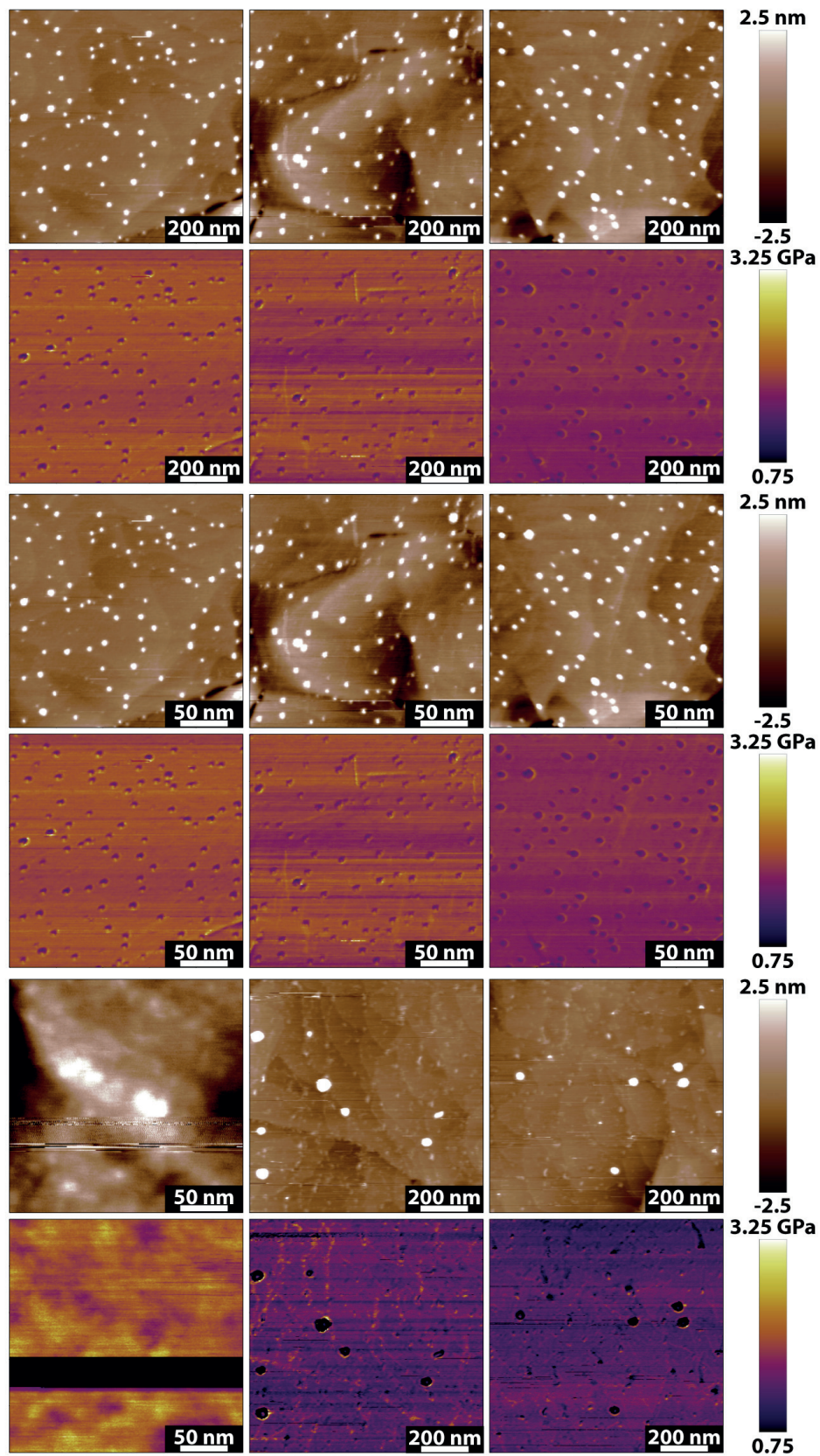


Figure A.2: Representative topography and corresponding E^* for three samples of C7 SAMs. Each row corresponds to one sample.

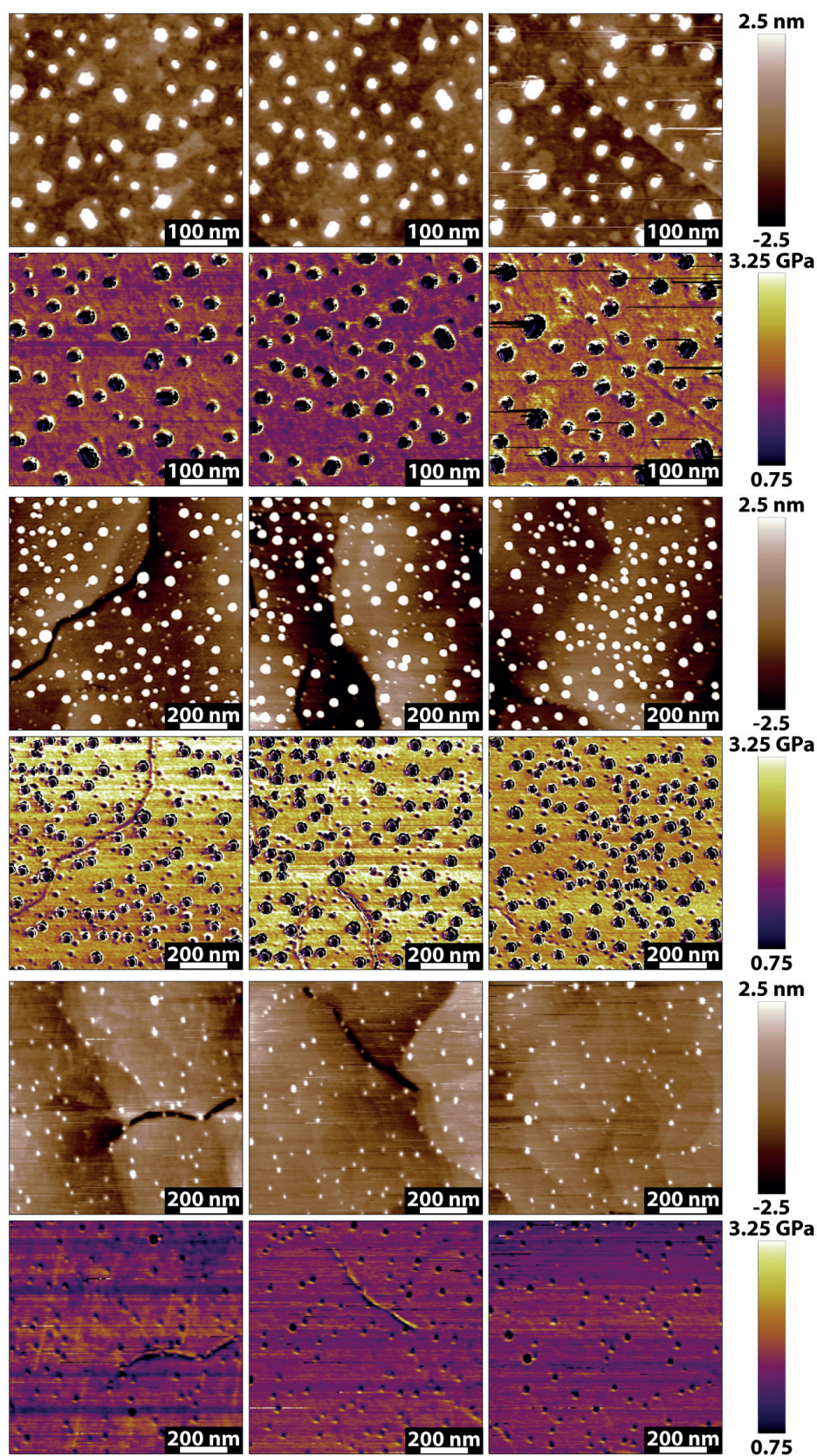


Figure A.3: Representative topography and corresponding E^* for three samples of OT SAMs. Each row corresponds to one sample. The large white dots, present especially in the first sample, correspond to ambient contamination and appear during scanning.

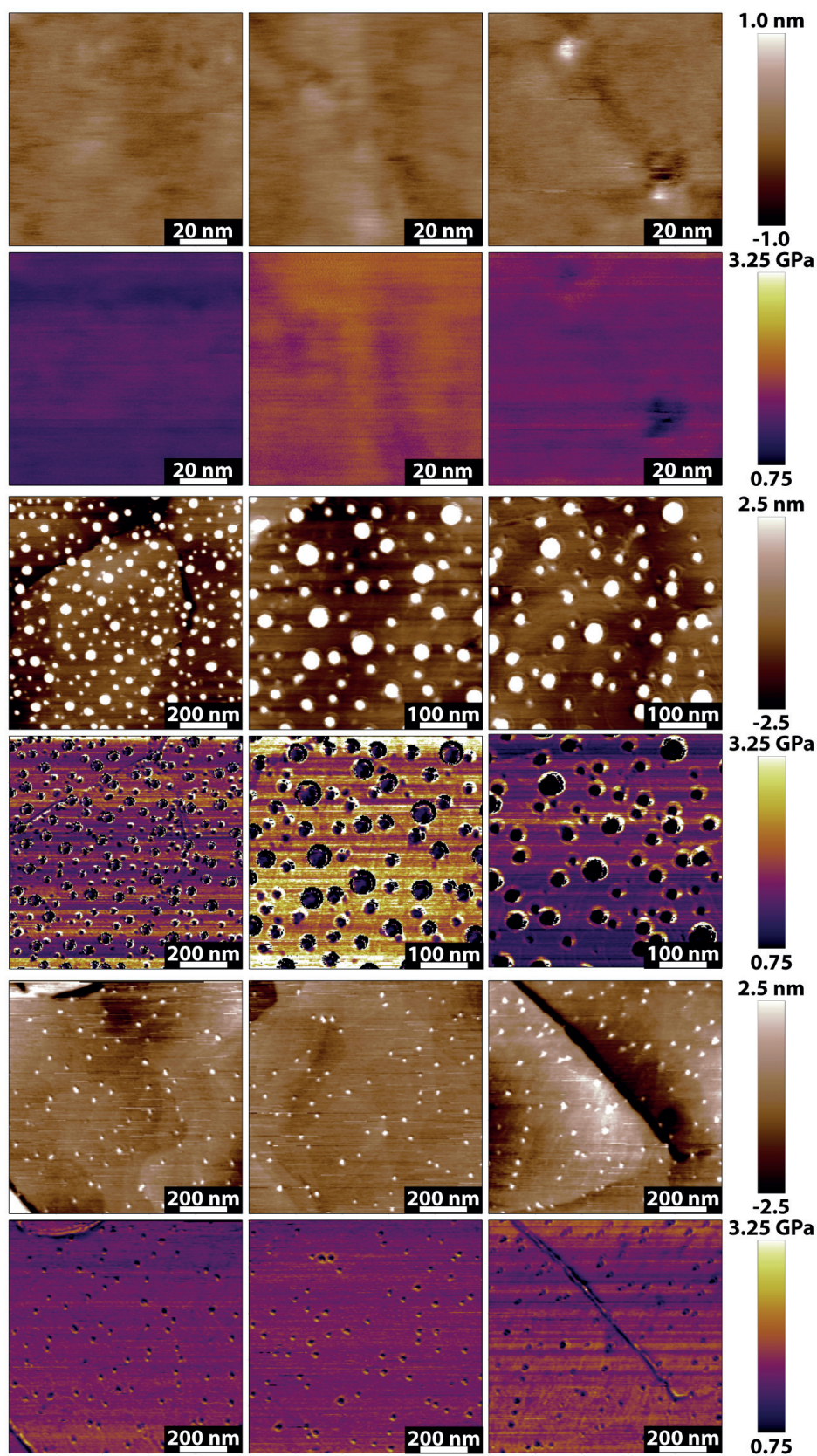


Figure A.4: C9: Representative topography and corresponding E^* for three samples of C9 SAMs. Each row corresponds to one sample.

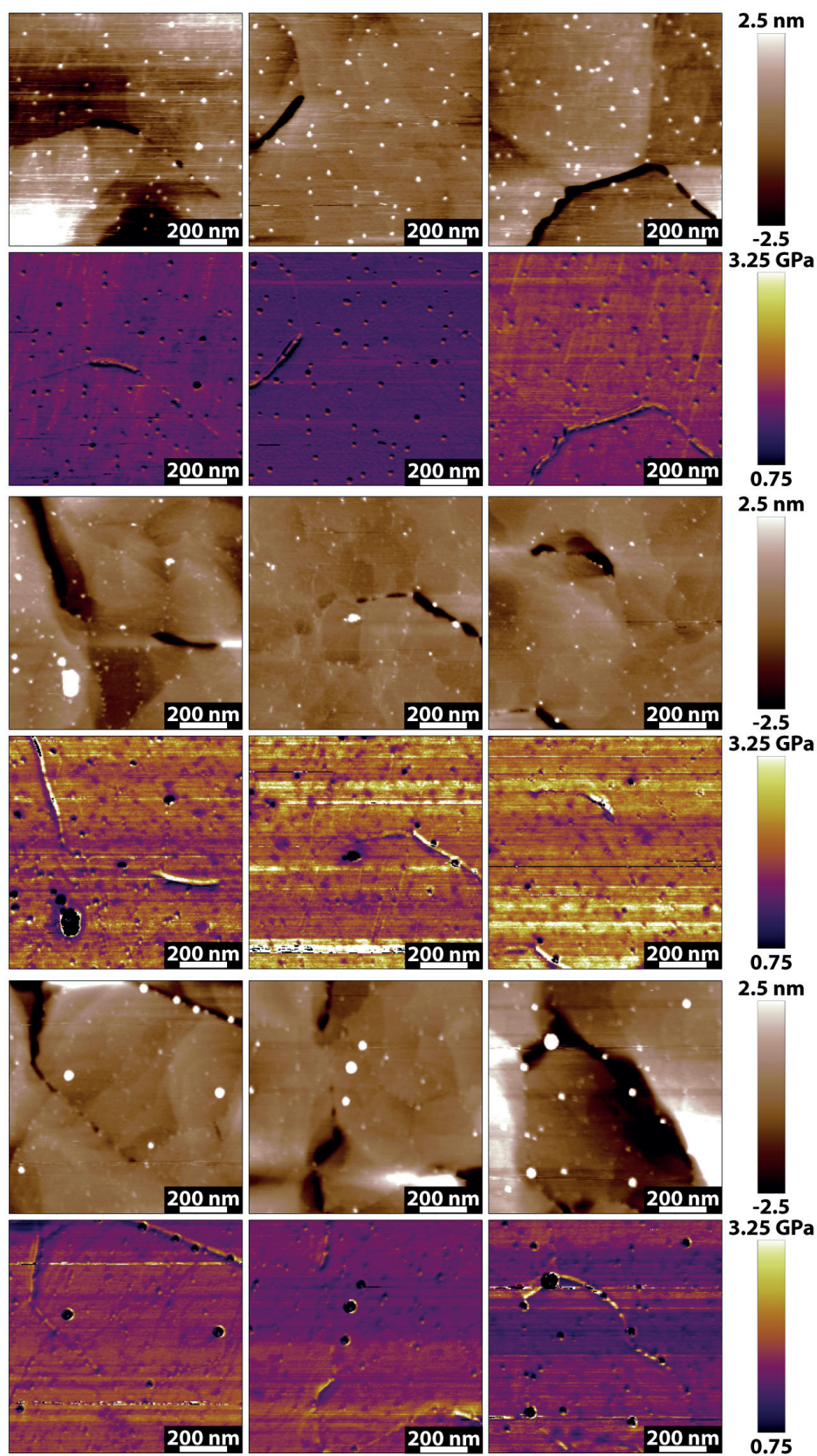


Figure A.5: Representative topography and corresponding E^* for three samples of C11 SAMs. Each row corresponds to one sample.

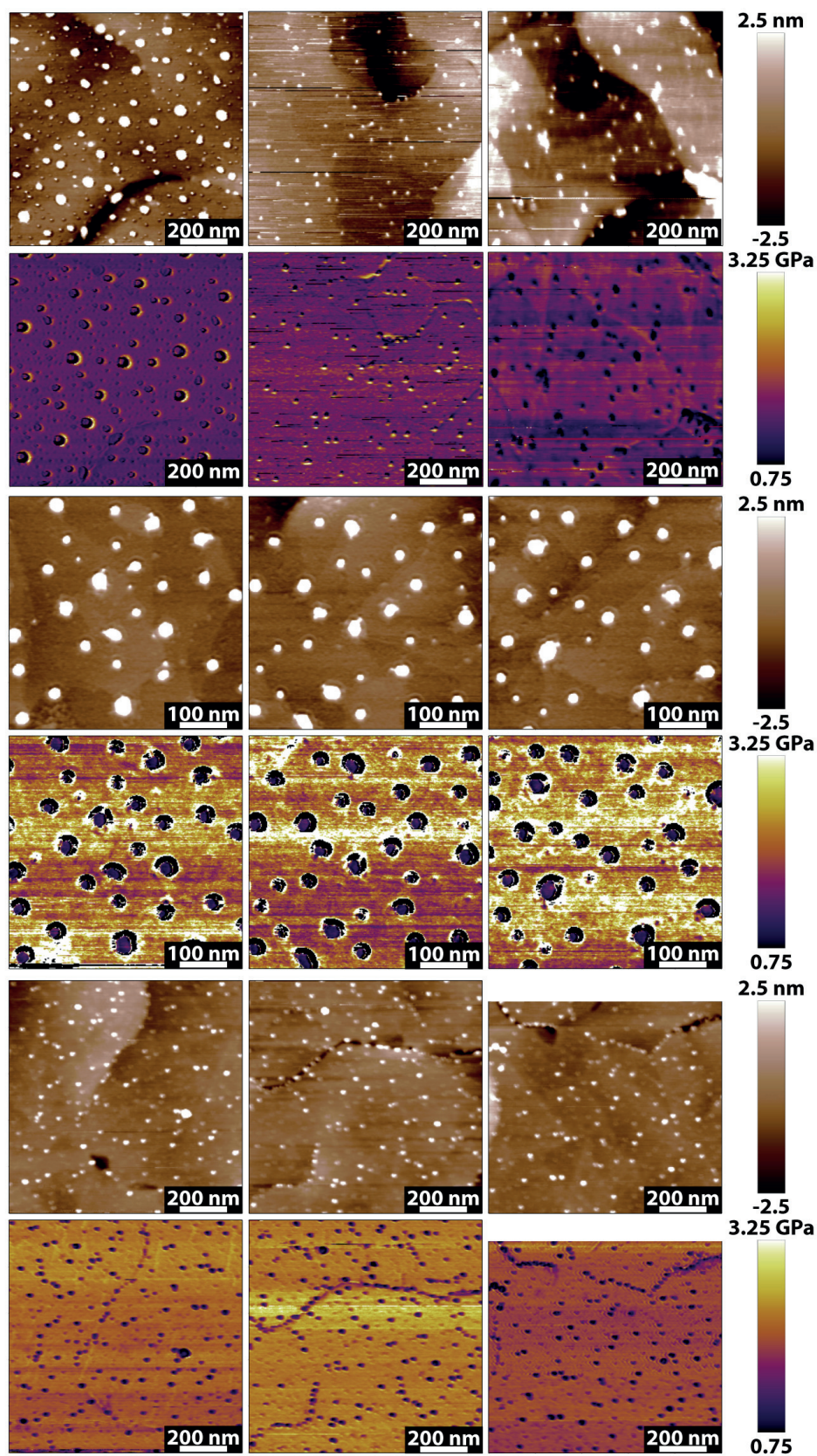


Figure A.6: Representative topography and corresponding E^* for three samples of C12 SAMs. Each row corresponds to one sample.

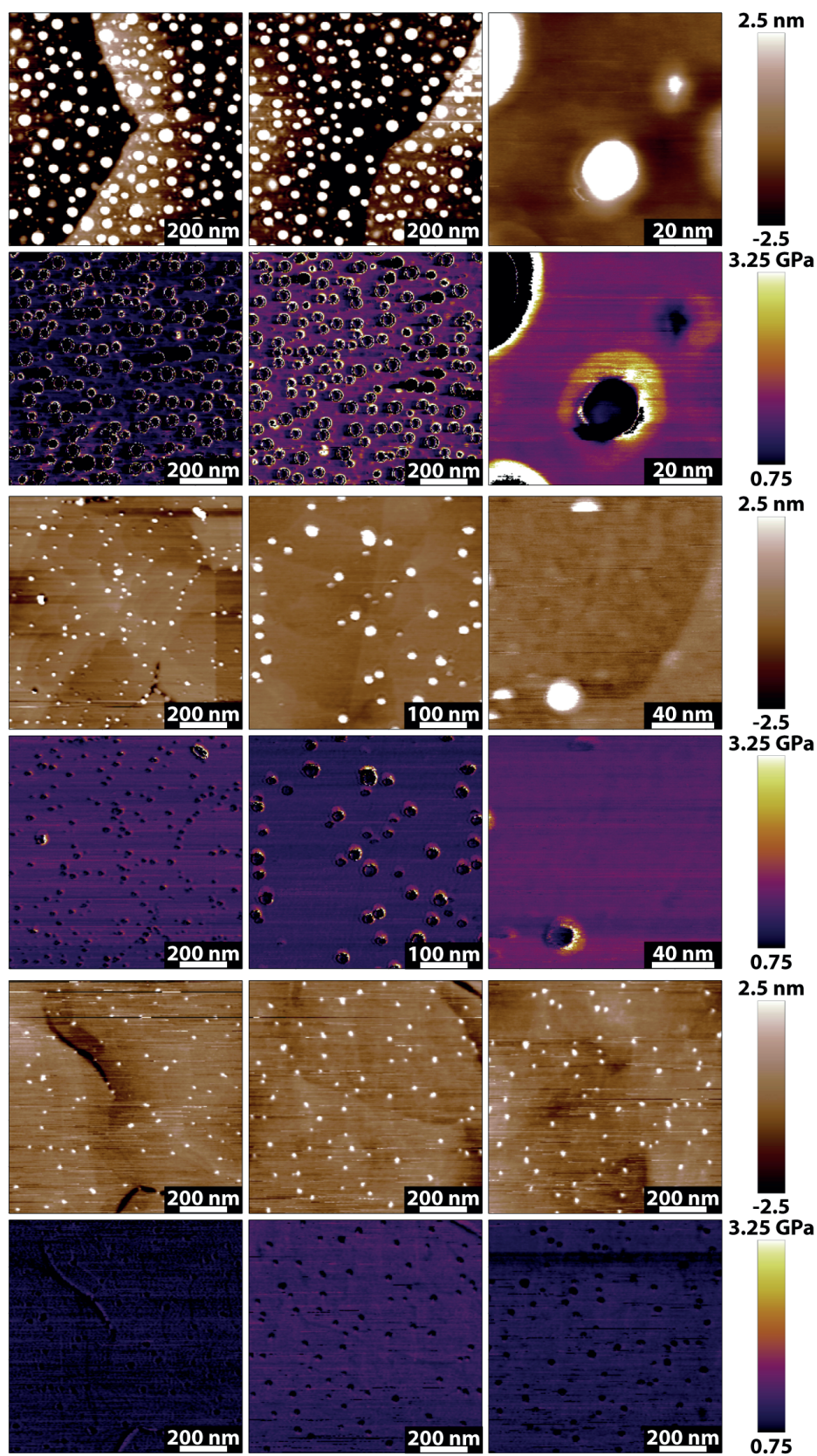


Figure A.7: Representative topography and corresponding E^* for three samples of C18 SAMs. Each row corresponds to one sample.

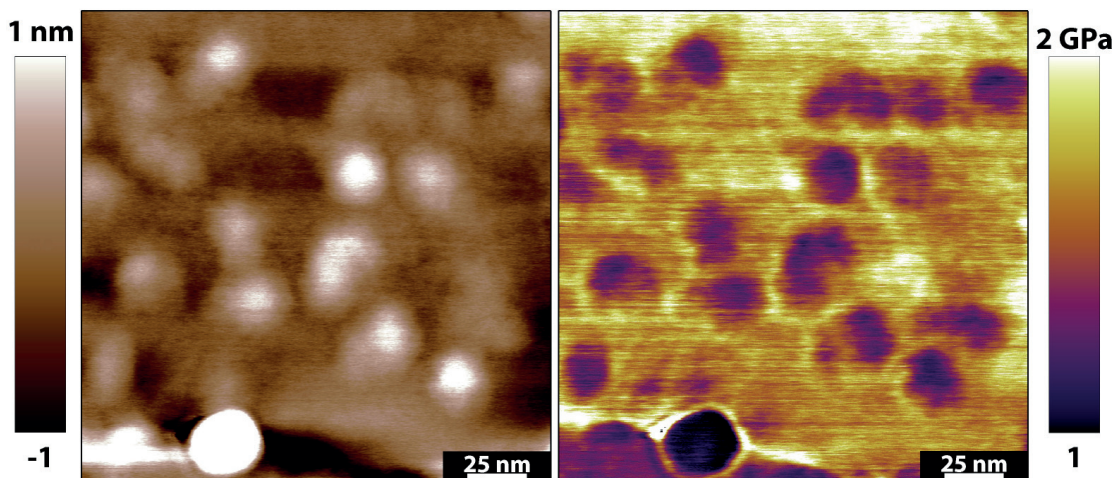


Figure A.8: Reproduction of OT:TMA binary SAM showing phase separation. The different domains show differences in E^* , consistent with the variations discussed in Chapter 4.

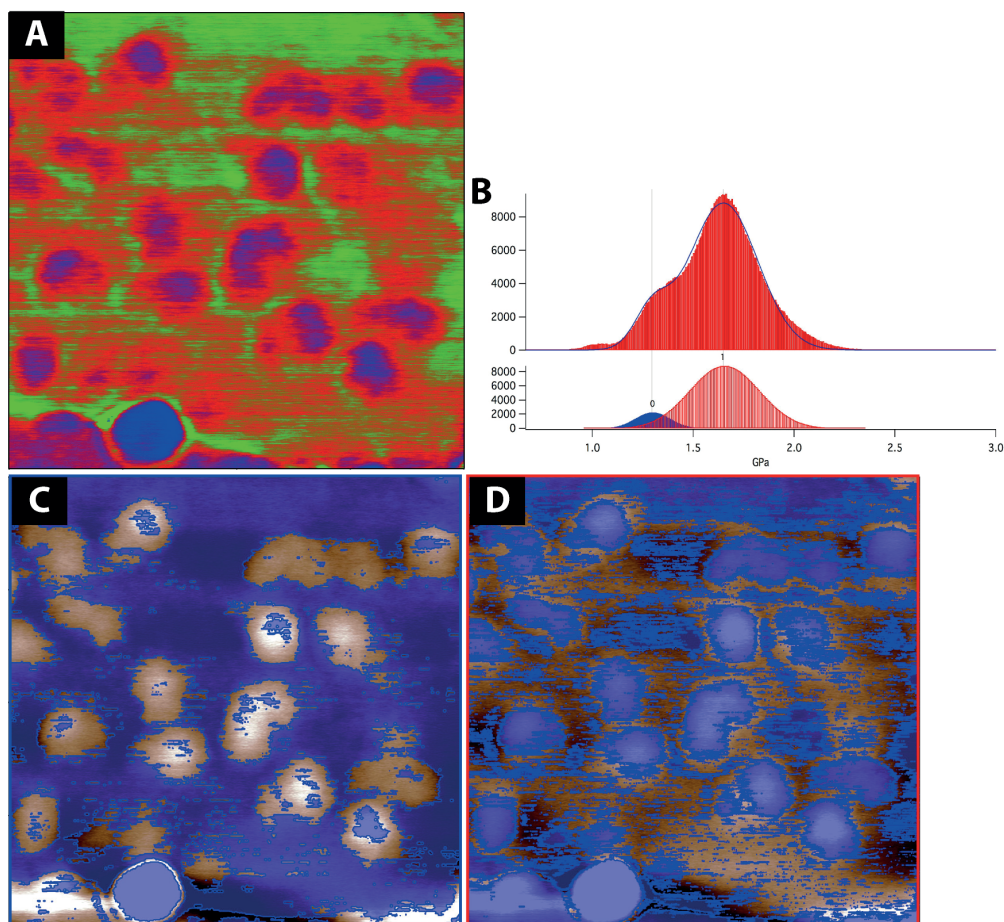


Figure A.9: Map of surface elasticity, E^* , for the OT:TMA mixed ligand SAM (A) shown in Figure A.8. Distribution of E^* can be fitted with two peaks, each centred at a different value ($1.30 \text{ GPa} \pm 0.09 \text{ GPa}$, and $1.65 \text{ GPa} \pm 0.17 \text{ GPa}$) (B). By thresholding at $E^* \pm \sigma$ for the two average E^* values, topographical features can be ascribed to each area (C, D).

Appendix B

In this section additional AFM images and calculations pertaining to the data discussed in Chapter 5 are presented. The presented information was omitted from the main body of the thesis for clarity. AFM images were acquired and treated as described in paragraph 5.2.

Table B.1: Analytical expression of absorption models proposed in the literature [1], [2].

Model	Equation
Langmuir (L)	$\theta(t) = \theta_o(1 - e^{-k_a t})$
Diffusion limited Langmuir (DLL)	$\theta(t) = \theta_o(1 - e^{-k_a \sqrt{t}})$
Non-diffusion limited second order Langmuir (SOL)	$\theta(t) = \theta_o[1 - (1 + k_a t)^{-1}]$
Diffusion (D)	$\theta(t) = k_a \sqrt{t}$
Two-step Langmuir (TSL)	$\theta(t) = \theta_o(1 - a e^{-k_{a,1} C t} - (1 - a) e^{-k_{a,2} C t})$
Modified Kisliuk (K)	$\theta(t) = \theta_o \frac{e^{k_a(1+k_E)t} - 1}{e^{k_a(1+k_E)t} + k_E}$

Table B.2: Fitting results of the experimental data to each model proposed in the literature [1], [2]. NaN denotes a non-converging model.

Model	Fitting Parameters			RSS
	θ_o	k_a	Other	
L	0.92	1.63 min ⁻¹	N/A	0.011
DLL	1.00	0.06 min ^{-1/2}	N/A	0.526
SOL	1.14	1.53 min ⁻¹	N/A	0.324
D	-	0.04 min ^{-1/2}	N/A	3.689
TSL	1.48	$k_{a,1} = 2.65 \times 10^3 (\text{M} \times \text{min})^{-1}$ $k_{a,2} = 1.41 (\text{M} \times \text{min})^{-1}$	$a=0.59$	0.001
K	NaN	NaN	$k_E (\text{NaN})$	NaN

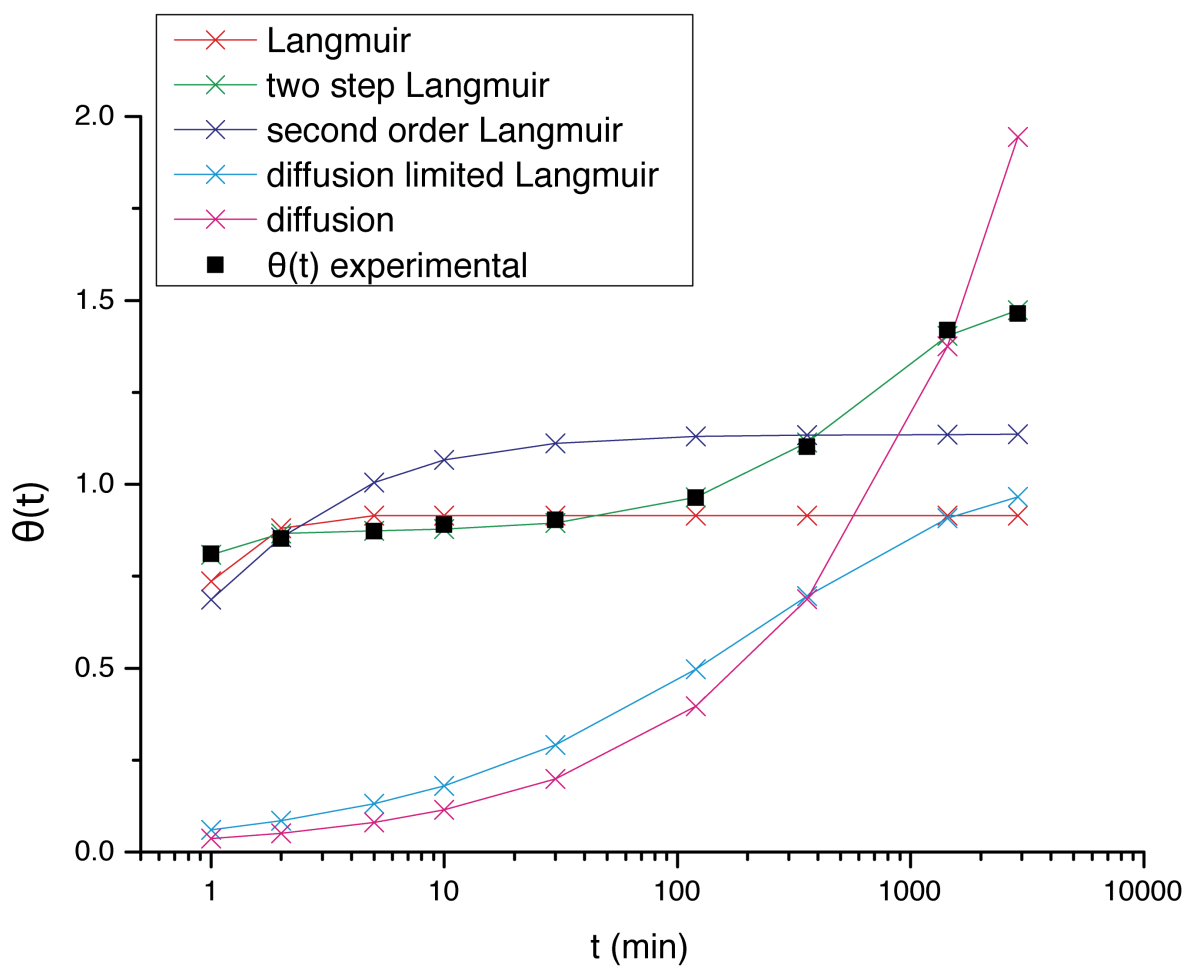


Figure B.1: Theoretically predicted evolution of ODPA absorption on Al_2O_3 and experimentally calculated surface coverage, $\theta(t)$. The best fit obtained was produced from a two step Langmuir absorption model.

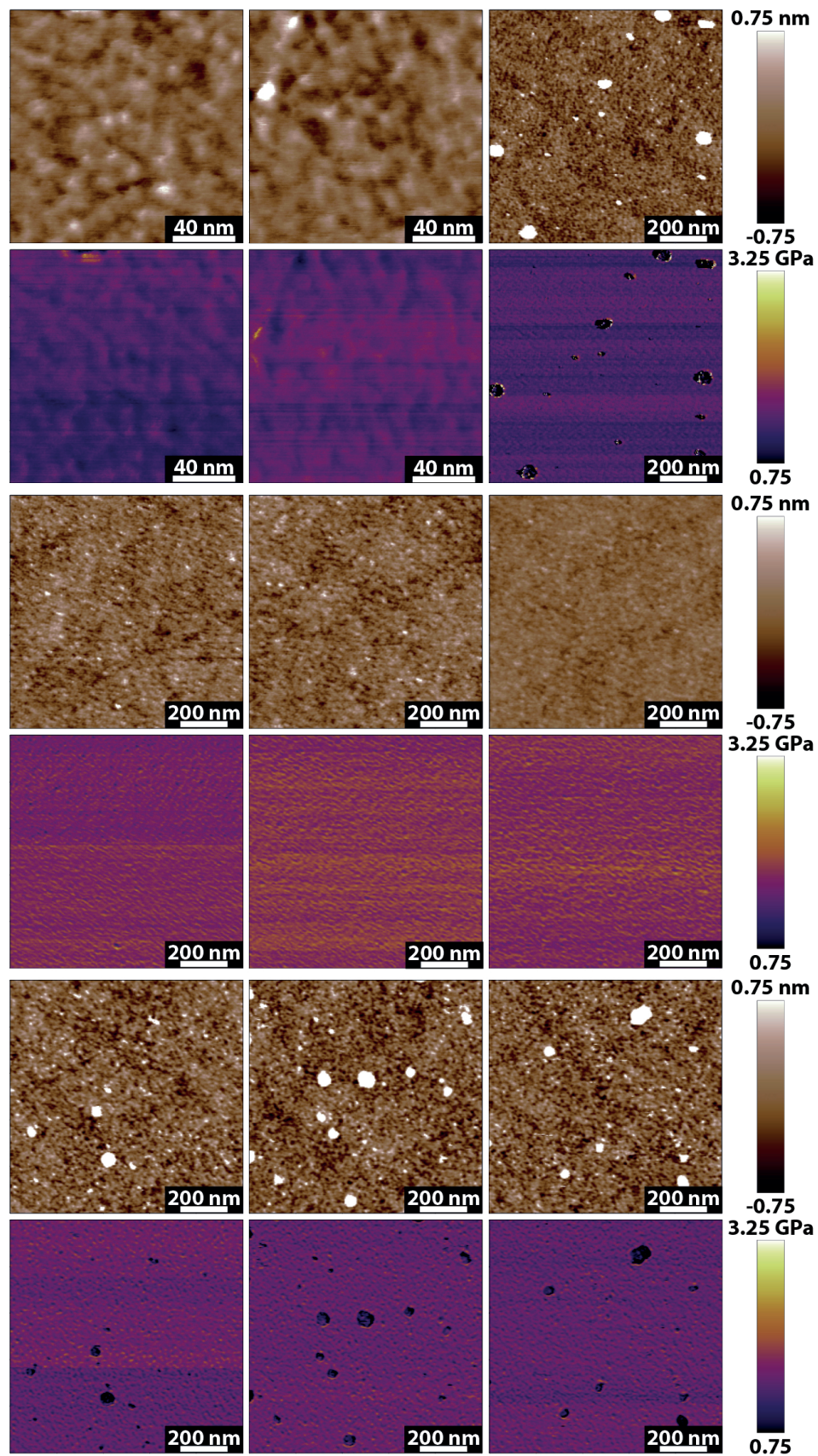


Figure B.2: Representative topography and corresponding E^* for three samples of ODPA SAMs at $t_M=1\text{min}$. Each row corresponds to one sample.

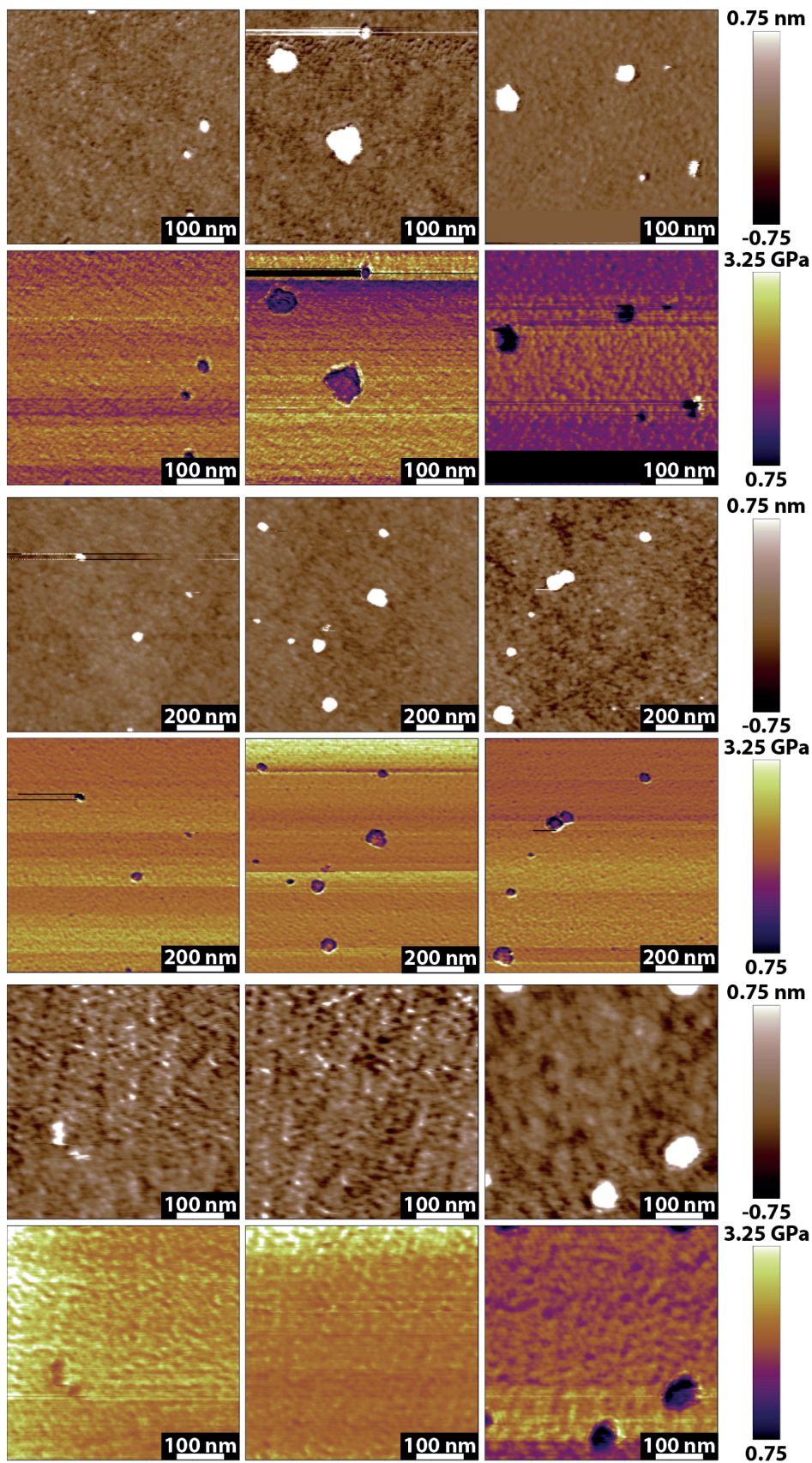


Figure B.3: Representative topography and corresponding E^* for three samples of ODPA SAMs at $t_m=2\text{min}$. Each row corresponds to one sample.

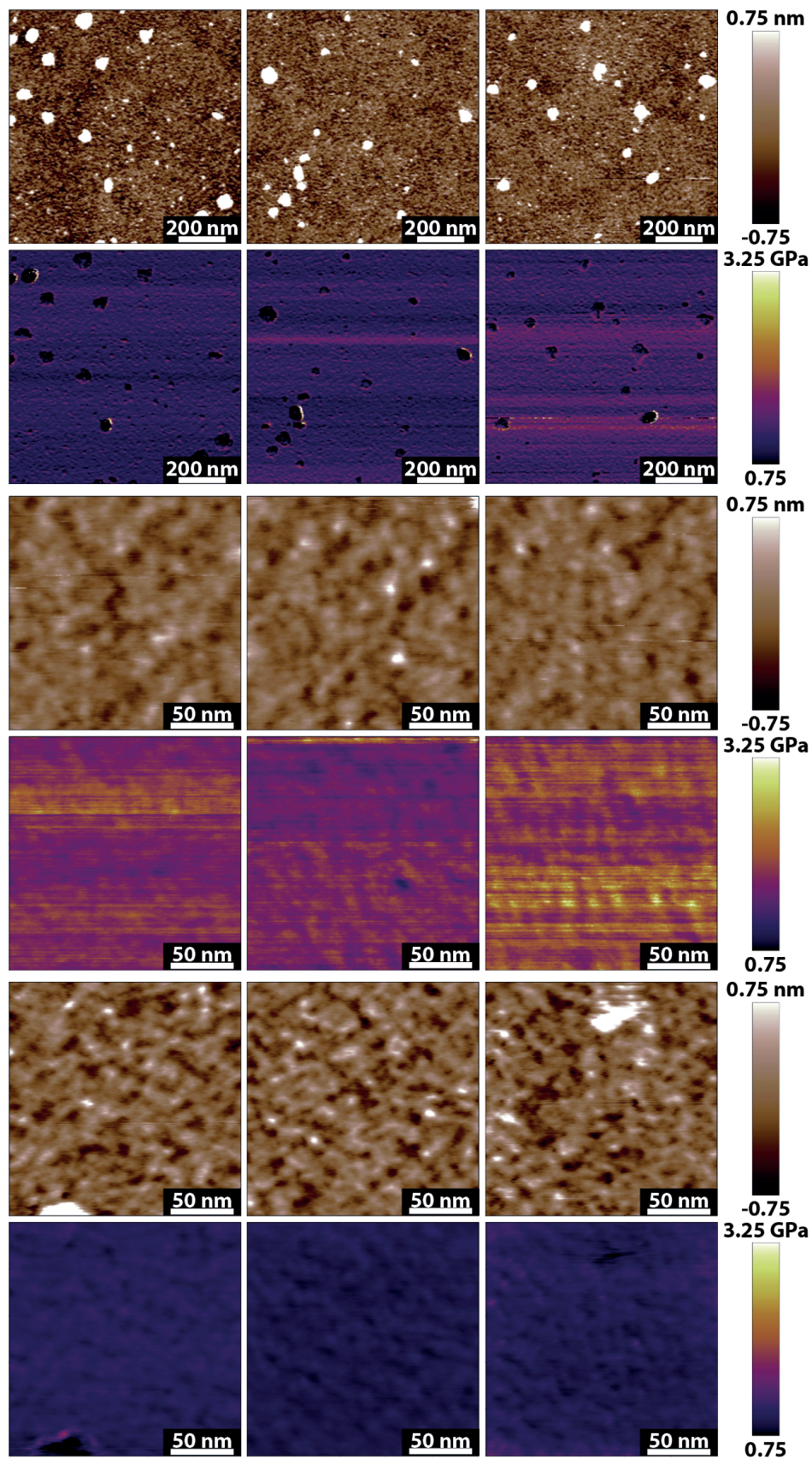


Figure B.4: Representative topography and corresponding E^* for three samples of ODPA SAMs at $t_M=5\text{min}$. Each row corresponds to one sample.

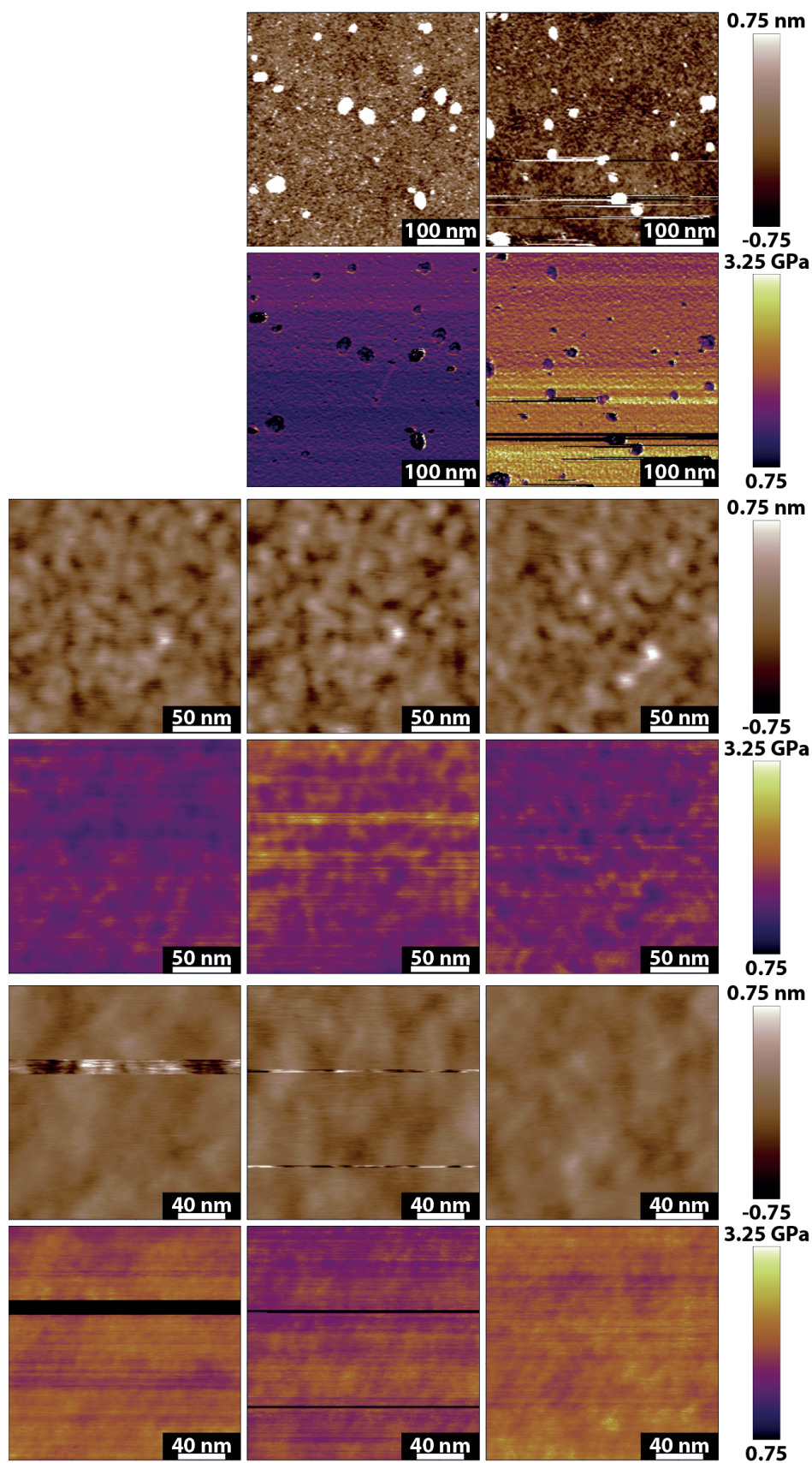


Figure B.5: Representative topography and corresponding E^* for three samples of ODPA SAMs at $t_m=10\text{min}$. Each row corresponds to one sample.

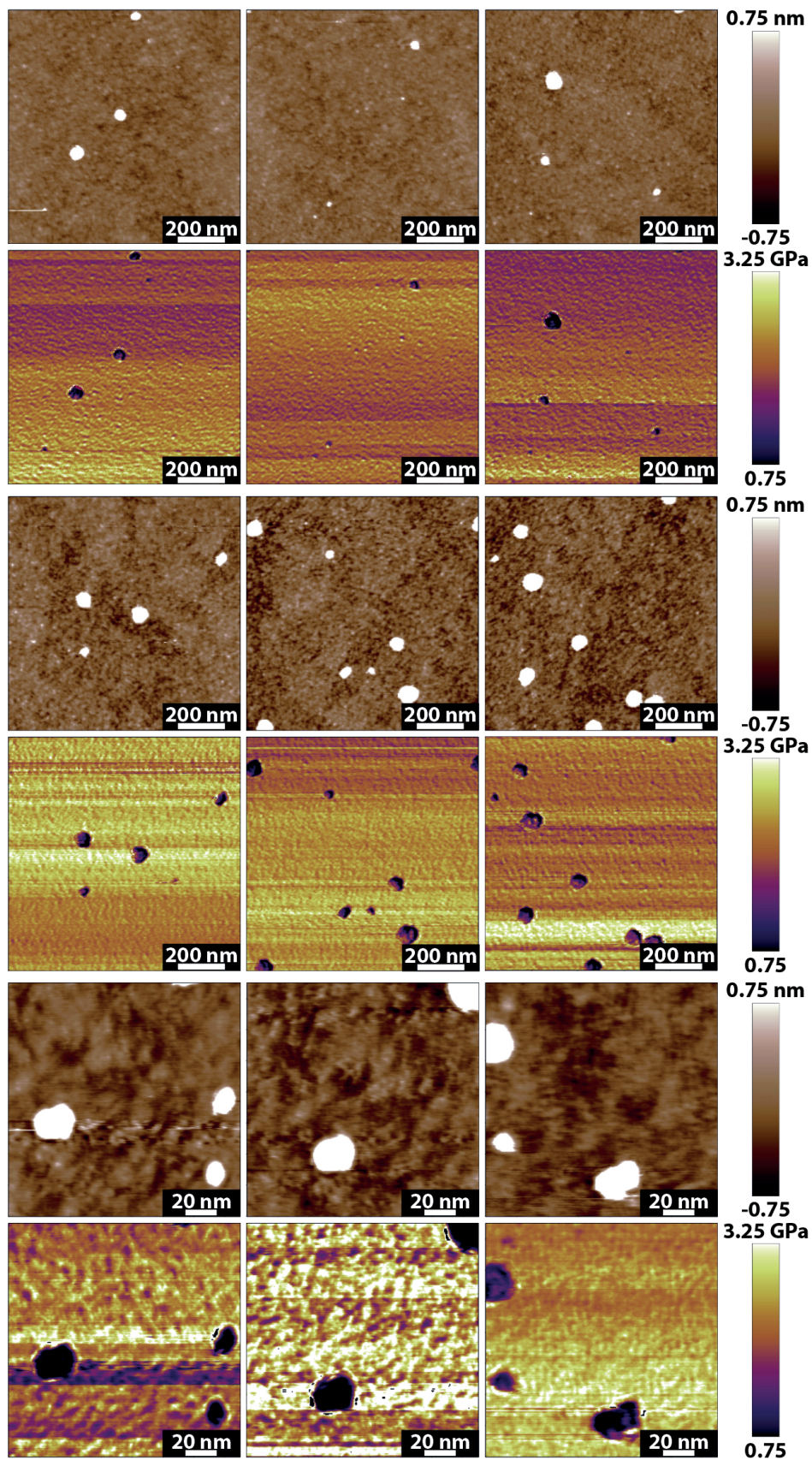


Figure B.6: Representative topography and corresponding E^* for three samples of ODPA SAMs at $t_M=30$ min. Each row corresponds to one sample.

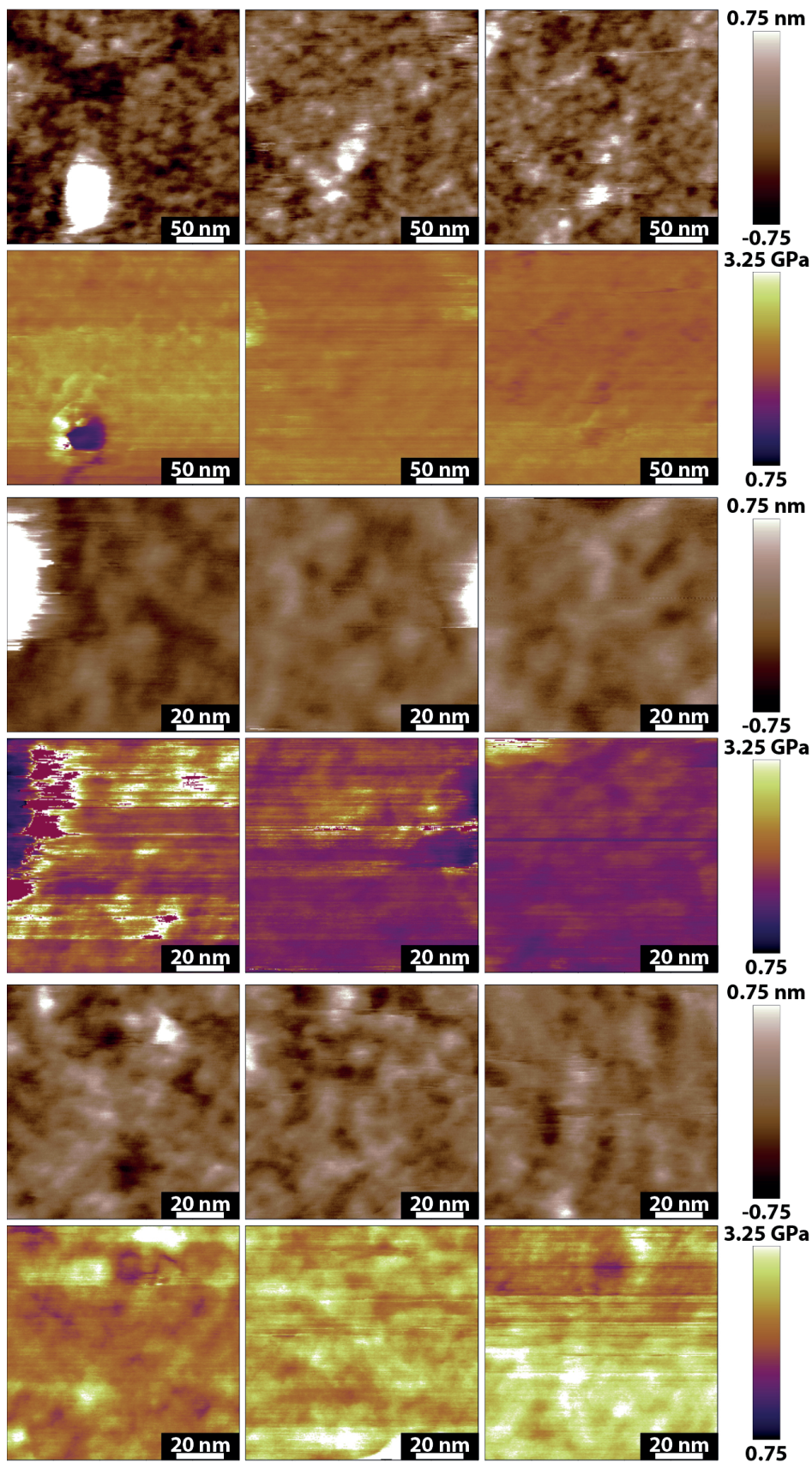


Figure B.7: Representative topography and corresponding E^* for three samples of ODPA SAMs at $t_m=2h$. Each row corresponds to one sample.

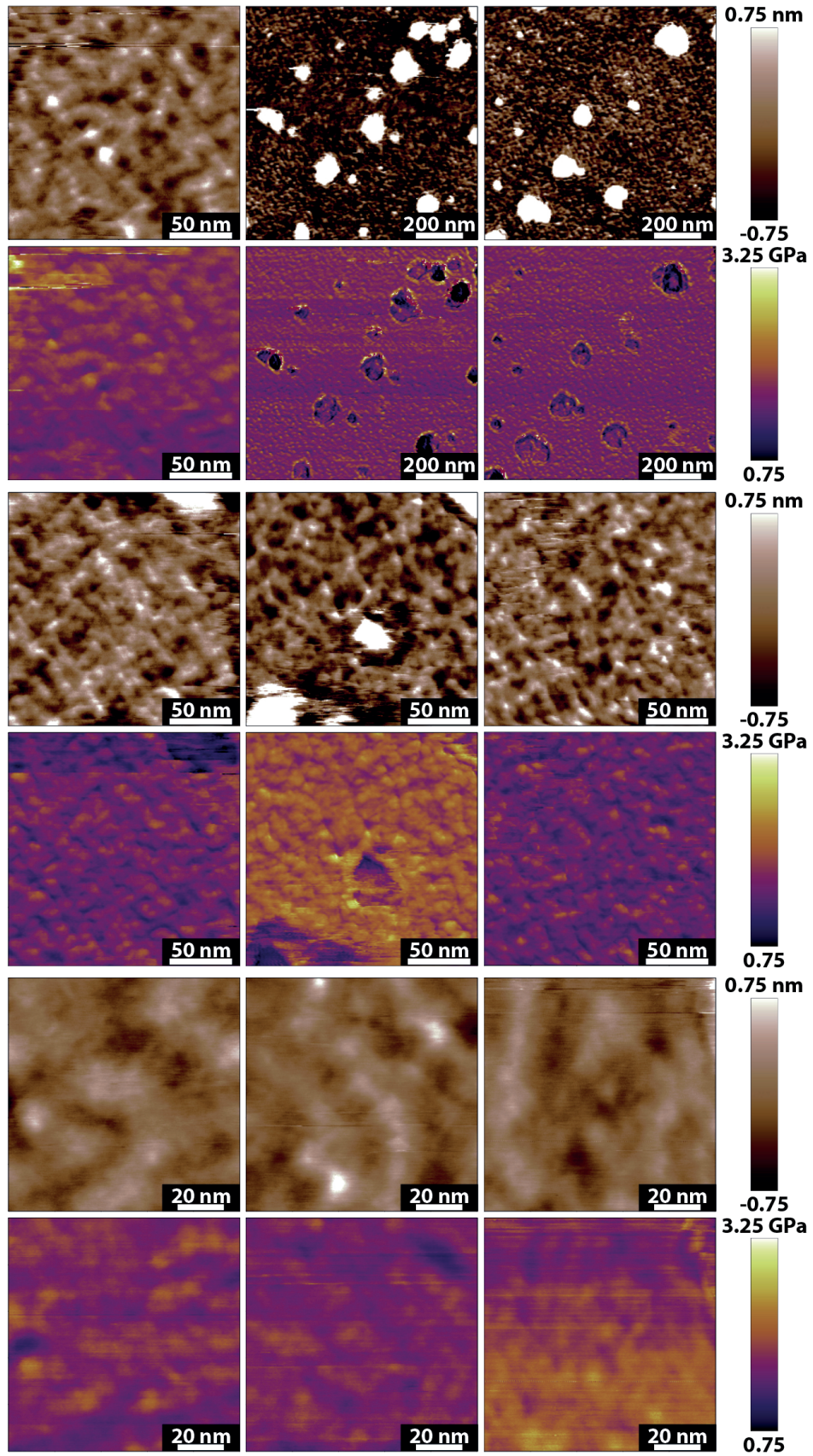


Figure B.8: Representative topography and corresponding E^* for three samples of ODPA SAMs at $t_M=6h$. Each row corresponds to one sample.

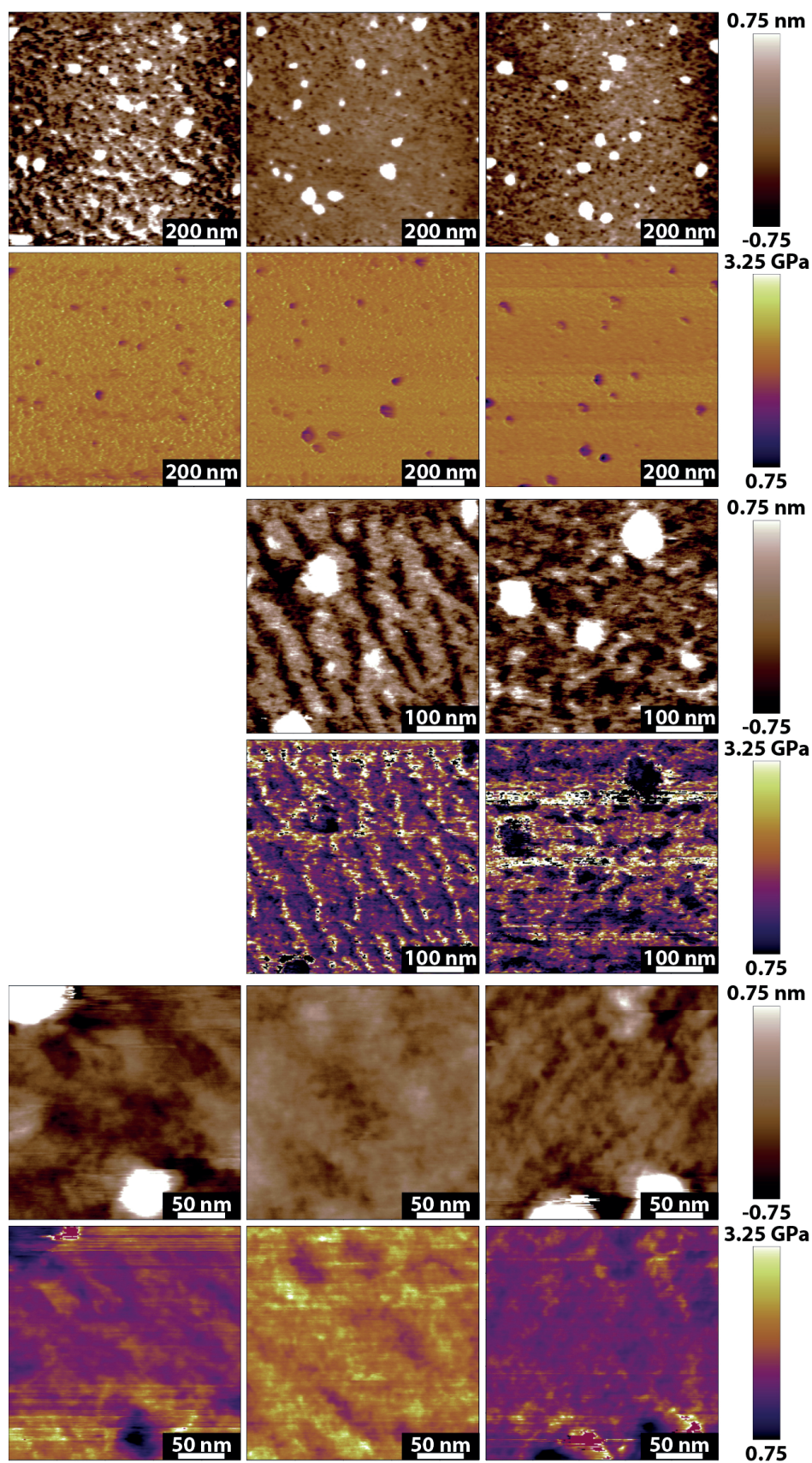


Figure B.9: Representative topography and corresponding E^* for three samples of ODPA SAMs at $t_m=24\text{h}$. Each row corresponds to one sample.

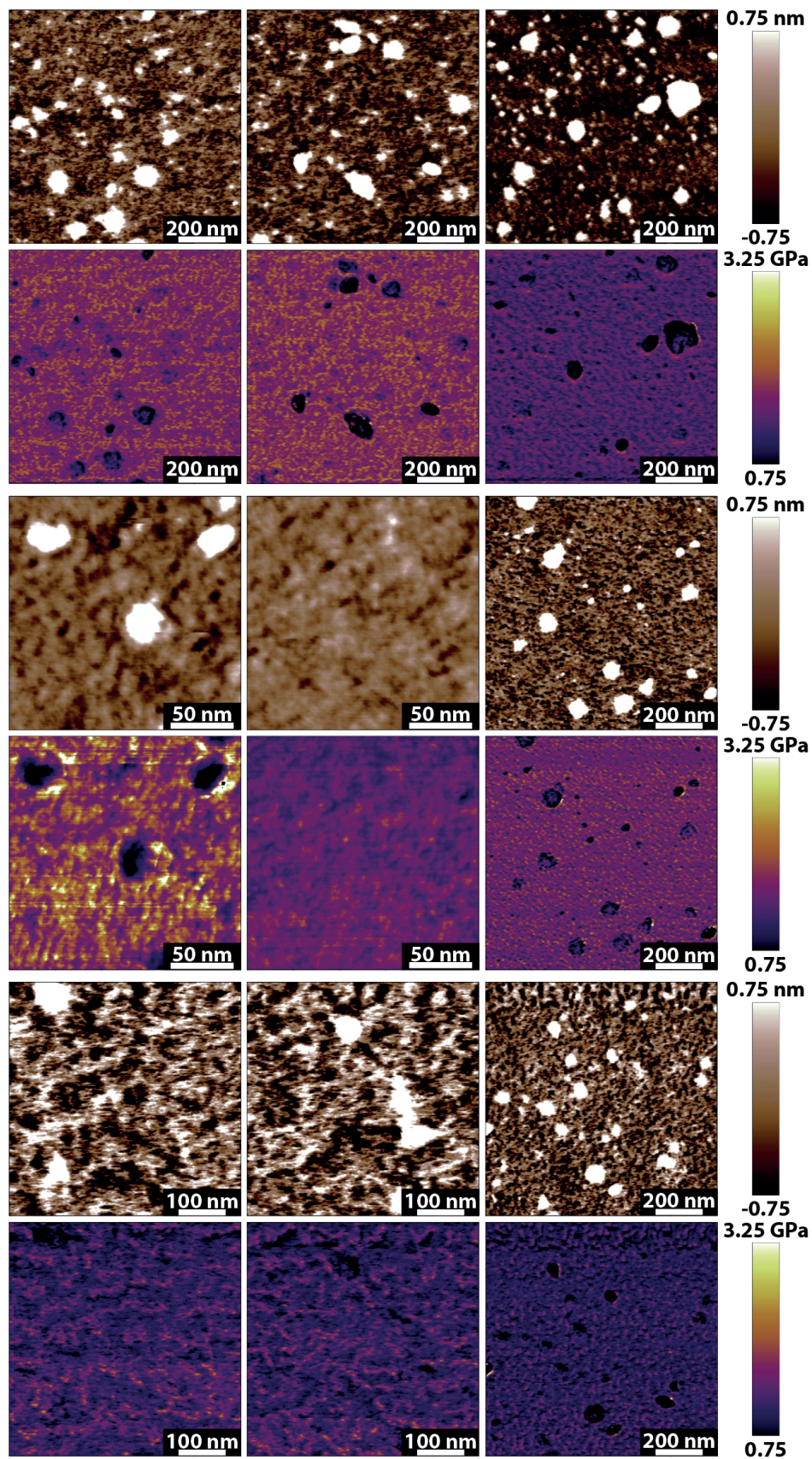


Figure B.10: Representative topography and corresponding E^* for three samples of ODPA SAMs at $t_M=48h$. Each row corresponds to one sample.

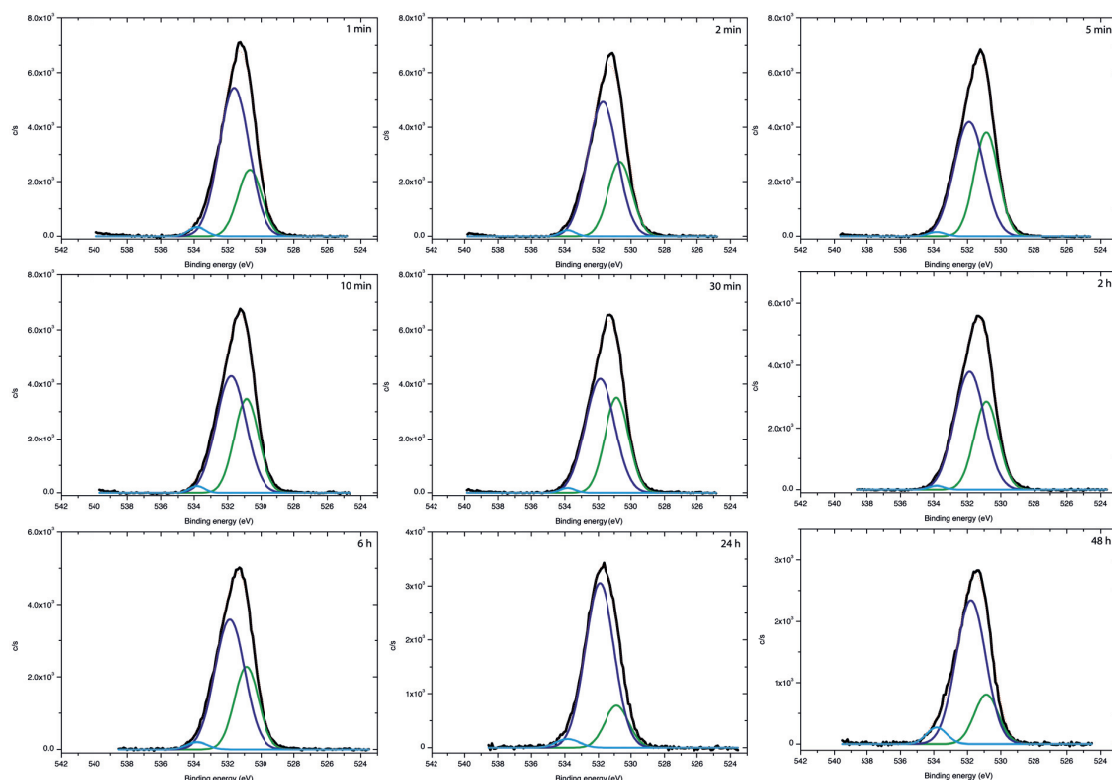


Figure B.11: Fitted O1s peaks (solid black line) of ODPA SAMs formed at all tested t_m . Three peaks are identified for every SAM, corresponding to different chemical species: Al-O-P at 531 eV (green line), P-OH and Al-O at 532 eV (purple line) and P=O at 534 eV (blue line).

References

- [1] A. G. Koutsoubas, N. Spiliopoulos, D. L. Anastassopoulos, A. A. Vradis, and G. D. Priftis, "Formation of alkane-phosphonic acid self-assembled monolayers on alumina: an in situ SPR study," *Surf. Interface Anal.*, vol. 41, no. 11, pp. 897–903, 2009.
- [2] R. Helmy and A. Y. Fadeev, "Self-assembled monolayers supported on TiO₂: Comparison of C₁₈H₃₇SiX₃ (X = H, Cl, OCH₃), C₁₈H₃₇Si(CH₃)₂Cl, and C₁₈H₃₇PO(OH)₂," *Langmuir*, vol. 18, no. 23, pp. 8924–8928, 2002.

Evangelia-Nefeli Athanasopoulou

Chemical Engineer, PhD candidate

eviathanasopoulou@hotmail.com

Avenue de Valmont 20
CH-1010 Lausanne, Vaud
(+41) 79 46 67446

09.07.1990
Greek, Australian

Education

- **2013 – present (exp. graduation 26/1/2018): EPFL, SuNMIL**
PhD candidate, “Scanning Probe Microscopy Characterization of Organic Self-Assembled Monolayers”
- **2008 – 2013: National Technical University of Athens (NTUA)**
School Of Chemical Engineering
Diploma of Chemical Engineering, Grade 8.72 / 10

Research experience

- **09/2013 - present:** SuNMIL, EPFL, Lausanne, Switzerland
PhD candidate; Supervisor: Prof. Francesco Stellacci
Synthesis and characterization of organic self-assembled monolayers on gold and Al₂O₃
Nanomechanical characterization of soft matter (self-assembled monolayers, collagen and amyloid fibers) using bimodal atomic force microscopy (AFM)
Nanomechanical characterization of hydrated gels (collagen derivatives), bacteria and eukaryotic cells using atomic force spectroscopy
Conductive AFM characterization of perovskite solar cells
AFM topographical and phase imaging in air and liquid environments
Al₂O₃ nanoparticles modification and characterization via FTIR, TGA and Raman spectroscopy
- **03/2013 - 07/2013:** Instituto Superior Técnico (IST), Lisbon, Portugal
External Master student; Supervisor: Ass. Prof. Fátima Montemor
Characterization of self-healing epoxy coatings for corrosion protection of AA2024-T3 via Electrochemical Impedance Spectroscopy (EIS), Local Electrochemical Impedance Spectroscopy (LEIS), Scanning Vibrating Electrode Technique (SVET) and Scanning Electron Microscopy (SEM)
- **10/2012 - 02/2013:** NTUA in conjunction with the National Center for Scientific Research "Demokritos", Athens, Greece
Trainee and Master student; Supervisor: Prof. Costas Charitidis (NTUA) and Ioannis Kartsonakis (Demokritos)
Synthesis and characterization of CeMo inhibitor loaded nanocontainers, chloride and water nanotraps and epoxy coatings for corrosion protection of AA2024-T3
- **07/2012-09/2012:** Sustainable Production and Consumption (SOSPROCAN) group, Universidad de Cantabria, Santander, Spain
Trainee; Supervisor: Prof. Angel Irabien
ASPEN modelling of the industrial process for obtaining synthetic rubber from styrene and butadiene

Teaching experience

- **02/2016 – 01/2017:** Department of Materials Science and Engineering, EPFL
Master student supervisor for semester projects “Preparation and Characterization of Al₂O₃ Core-Shell Nanoparticles” I & II
- **09/2014 - 12/2014:** Department of Materials Science and Engineering, EPFL
Teaching assistant for the course “Surfaces and Interfaces”

Teaching experience

- **09/2013 – 12/2013:** Department of Materials Science and Engineering, EPFL
Teaching assistant for the course “Thermodynamics for Materials Science”

Peer-reviewed publications

- S. Majumdar, X. Wang, S. D. Sommerfeld, J. J. Chae, E. Athanasopoulou, L. Shores, X. Duan, L. M. Amzel, F. Stellacci, O. Schein, Q. Guo, A. Singh, J. Elisseeff. Artificial chaperone driven collagen self-assembly to engineer a

biomimetic cornea implant. Nat. Biomed. Eng., *submitted*

- S. Paek, P. Gao, E. Athanasopoulou, K. Taek Cho, G. Grancini, Y. Lee, P. Schouwink, Yi Zhang, F. Stellacci and M. K. Nazeeuddin. From Nano to Micrometer Scale: Role of Anti-Solvent Treatment on the Performance of Composite Perovskite Solar Cells. Chem. Mater. 29 (2017) 3490-3498
- I.A. Kartsonakis, E. Athanasopoulou, D. Snihirova, B. Martins, M.A. Koklioti, M.F. Montemor, G. Kordas, C.A. Charitidis. Multifunctional Epoxy Coatings Combining a Mixture of Traps and Inhibitor Loaded Nanocontainers for Corrosion Protection of AA2024-T3. Corros. Sci. 85 (2014) 147-159
- **11/2017, 2017 MRS Fall Meeting & Exhibit**, Boston, USA: E. Athanasopoulou and F. Stellacci. Nanomechanical Characterization of Organic Self Assembled Monolayers Using Bimodal Atomic Force Microscopy, oral presentation
- **06/2017, EDMX Research Day 2017**, EPFL, Lausanne, Switzerland: E. Athanasopoulou and F. Stellacci. Nanomechanical Characterization of Soft Matter Using Bimodal Atomic Force Microscopy, poster presentation
- **10/2016, CCMX-MaP “Soft Interfaces in Industry: Current Challenges and New Directions”**, ETH, Zurich, Switzerland. E. Athanasopoulou and F. Stellacci. Nanomechanical Characterization of Soft Surfaces Using Bimodal Atomic Force Microscopy, poster presentation
- **11/2015, EDMX Research Day 2015**, EPFL, Lausanne, Switzerland: E. Athanasopoulou and F. Stellacci. Mixed ligand SAMs for the surface modification of Al₂O₃, poster presentation
- **02/2015, 9th Workshop Ellipsometry**, University of Twente, the Netherlands: P. Basa, E. Athanasopoulou and F. Stellacci. Organic Monomolecular Coatings on Alumina Studied by Mueller Matrix Ellipsometry, poster presentation
- **09/2013, EUROCRR 2013**, Estoril, Portugal: I. Kartsonakis, **E. Athanasopoulou**, D. Snihirova, F. Montemor, C. Charitidis, G. Kordas. Multilayer Epoxy Coatings Including Nanotraps and Nanocontainers for Corrosion Protection of AA2024-T3, oral presentation

Conference presentations and posters

Language skills

- Greek (native language)
- English (Cambridge Certificate of Proficiency in English, 2006, grade B)
- German (Goethe – Zertifikat B1: Zertifikat Deutsch, 2011, grade Sehr Gut-Very good (score 282.00 / 300))
- French (Centre de Langues EPFL, A2/B1)

Computer skills

- Excellent command of Microsoft Office™ tools (Word™, Excel™, Power Point™)
- Basic knowledge of data processing tools and programs (Origin™, Mathematica™)

Interests

Swimming, reading, traveling

